Voltage Control of Electrical, Optical and Magnetic Properties of Materials by Solid State Ionic Transport and Electrochemical Reactions

by

Mantao Huang

Submitted to the Department of Materials Science and Engineering
in partial fulfilment of the requirements for the degree of

Doctor of Philosophy in Materials Science and Engineering

at the

MASSACHUSETTS INSTITUTE OF TECHNOLOGY

May 2020

© Massachusetts Institute of Technology 2020. All rights reserved

Author……………………………...…………………………………………………………........
Department of Materials Science and Engineering
April 30, 2020

Certified by………………………………………………………………………………………........
Geoffrey S. D. Beach
Professor, Co-director, Materials Research Laboratory (MRL)
Thesis Supervisor

Accepted by…...……………………………………………………………………………………........
Frances M. Ross
Chair, Departmental Committee on Graduate Studies

Voltage Control of Electrical, Optical and Magnetic Properties of Materials by Solid State Ionic Transport and Electrochemical Reactions

by

Mantao Huang

Submitted to the Department of Materials Science and Engineering
in partial fulfilment of the requirements for the degree of

Doctor of Philosophy in Materials Science and Engineering

Abstract

Reversible post-fabrication control of material properties enables devices that can adapt to different needs or environmental conditions, and brings additional levels of functionality, paving the way towards applications such as reconfigurable electronics, reconfigurable antennas, active optical devices and energy efficient data storage. One promising way of achieving the controllability is through solid-state ionic transport and electrochemical reactions in thin film structures, where the properties of materials can be electrically controlled by a gate voltage in an addressable way. Here we explore using such ionic gating method to control the electrical, optical and magnetic properties of solid-state thin film layers, and show that large modification can be achieved for a wide range of properties. We demonstrate a new type of three terminal resistive switching device where the resistivity of a thin film conductive channel can be controlled by a gate voltage. We demonstrate solid-state ionic gating of the optical properties of metals and oxides and show the versatility of the approach by implementing voltage-controlled transmission, thin film interference, and switchable plasmonic colors. We also show that the approach allows for voltage control of ferrimagnetic order, demonstrating voltage induced 180-degree switching of the Néel vector, as a new way of magnetic bit writing. These findings extend the scope of voltage programmable materials and provide insights into the mechanisms of voltage controlled material properties by solid-state ionic transport and electrochemical reactions.

Thesis Supervisor: Geoffrey S. D. Beach

Title: Professor, Co-director, Materials Research Laboratory (MRL) at MIT

Acknowledgements

Foremost, I would like to express my gratitude to my thesis advisor Prof. Geoffrey Beach for his guidance, help and support. He always shows great enthusiasm and interest in my research. His positive attitude and encouragement helped me to recognize challenges as opportunities. He has students' interest at his heart and has introduced me to many valuable opportunities. I am very grateful for his advice and insightful suggestions. I could not have imagined having a better advisor and mentor.

I would also like to thank my thesis committee members Prof. Harry Tuller and Prof. Silvija Gradečak. During every meeting with Prof. Tuller, I find so much to learn about ionics. I also thank Prof. Gradečak for her valuable comments and feedbacks on my research.

I have been very lucky to work with talented and fun people in Beach Group. To Aik Jun Tan, Alexander Kossak, Angela Wittmann, Byunghun Lee, Can Onur Avci, Chi-Feng Pai, Daniel Suzuki, Elizaveta Tremsina, Felix Buettner, Ivan Lemesh, Jason Bartell, Kai Litzius, Kohei Ueda, Lucas Caretta, Maxwell Mann, Minae Ouk, Parnika Agrawal, Pooja Reddy, Sara Sheffels, Sarah Schlotter, Sasha Churikova, Seonghoon Woo, Siying Huang and Usama Hasan, thank you for your help and support. Special thanks to Aik Jun Tan for helping me get started with experiments in the lab and sharing his passion for research, Maxwell Mann for his help setting up instruments and sharing the fun projects he worked on, Lucas Caretta for his encouragement and valuable discussions, and Felix for his help on beamtime experiments.

I would like to acknowledge collaborators from other laboratories for their help. Special thanks to Prof. Bilge Yildiz and Konstantin Klyukin for magnetic simulations, and Prof. Joel Yang, Hailong Liu, and Qifeng Ruan from Singapore University of Technology and Design for helping me

understand more on plasmonics. I also thank Seonghoon Woo, Ki-Young Lee (Korea Institute of Science and Technology), Dr. Karin, Jonas Zehner (IFW Dresden and Institute of Material Science, TU Dresden), Ira Waluyo, Adrian Hunt, Wen Hu, Claudio Mazzoli (Brookhaven National Laboratory), Manuel Valvidares, Pierluigi Gargiani (ALBA Beamline), Prof. Veis, Lukáš Beran, and Michal Vančík (Charles University in Prague).

I have been very lucky to have the help from David Bono, Colin Marcus, and Brian Neltner for setting up and troubleshooting many instruments that are essential for the thesis. I thank David Bono for patiently answering all my questions and helping me learn electronics. The thesis research work relied heavily on shared facilities at MIT; I would like to thank Kurt Broderick (Microsystems Technology Laboratories), Mark Mondol and Jim Daley (NanoStructures Laboratory), and Mike Tarkanian (Department of Materials Science and Engineering, DMSE). My thanks also extend to the DMSE administrative office stuff, especially Angelita Mireles, Dominique Altarejos, and Elissa Haverty.

Finally, I would like to thank my close friends and family for their support. My graduate school experience would not be complete without my friends. I thank my family for their encouragement, care and support. I'm especially grateful to my parents for their unconditional love. Lastly, I would like to thank my lovely and beautiful girlfriend Shengnan Huang. She always believes in me even when things went seemingly wrong. I thank her for care and love that makes every day of my life enjoyable.

I acknowledge the financial support from MIT Lincoln Lab, NSF MRSEC program under award number award number DMR-1419807, MIT-SUTD Graduate Fellows Program, MIT Deshpande Center for Technological Innovation, and Kavanaugh Translational Innovation Fellowship.

Table of Contents

Chapter 1 Introduction 17

1.1 Motivation 17

1.2 Thesis Outline 18

Chapter 2 Background 21

2.1 Previous Work on Voltage-Controlled Material Properties 21

2.2 Optical Properties 25

2.2.1 Thin Film Interference 25

2.2.2 Plasmonics 28

2.2.3 Dynamic Control of Optical Properties 31

2.3 Magnetic Anisotropy and Magnetic Hysteresis Loops 35

2.4 Ferrimagnets 37

Chapter 3 Experimental Methods 41

3.1 Sample Fabrication 41

3.1.1 Magnetron Sputtering 41

3.1.2 Lithography 44

3.2 Magneto-Optical Kerr Effect 48

3.3 Anomalous Hall Effect 49

3.4 X-ray Absorption Spectroscopy (XAS) and X-ray Magnetic Circular Dichroism (XMCD) 51

Chapter 4 Voltage Control of Resistivity Based on Metal/Metal Oxide Redox Reactions..... 55

4.1 Experimental Methods 57

4.2 Voltage Induced Resistive Switching 57

4.3 Modeling Oxidation Progress 61

4.4 Large Voltage Induced Resistance Switching 64

4.5 Material Selections and Device Designs for Better Switching Performance 67

4.6 Summary 70

Chapter 5 Voltage-Gated Optics and Plasmonics Enabled by Solid-State Proton Pumping... 71

5.1 Experiment Methods 73

5.2 Optical Property Switching Using a Solid-state Proton Pump 75

5.3 Switchable Plasmonic Color Devices 79

5.4 Giant Reversible Switching of Effective Refractive Index 82

5.5 Switching Performance 86

5.6 Additional Implementations of Color Switching Devices 93

5.7 Discussion 99

Chapter 6 Voltage Control of Ferrimagnetic Order and Voltage-Assisted Writing of Ferrimagnetic Spin Textures by Solid-State Hydrogen Gating 101

6.1 Experiment Methods 103

6.2 Dominant Sublattice Switching and Compensation Temperature Gating 106

6.3 *Ab initio* Modeling of Hydrogen-Enabled Switching of Ferrimagnetic Order 115

6.4 Reversibility of Sublattice Gating and 180° Néel Vector Switching 116

6.5 Fast Hydrogenation with Voltage Pulses 122

6.6 Reversed Domain and Skyrmion Generation in Racetrack Devices 125

6.7 Voltage Control of Magnetic Anisotropy of Bulk PMA Films.................................. 128

6.8 Conclusions 130

Chapter 7 Summary and Outlook 133

7.1 Summary 133

7.2 Outlook.. 135

7.2.1 High Resolution Optical Modulator with Applications of Ultra-High Pixel Density Displays or Holographic Displays 135

7.2.2 Using SiO_2 and Spin-Coated Hydrogen Silsesquioxane (HSQ) as the Solid Electrolyte for Proton Conduction 136

7.2.3 Controlled Properties as Quantitative Probes for Nanoionics 137

7.2.4 Voltage Control of Spin–Orbit Torque (SOT) Switching Threshold for Alternative Implementation of Reversed Domain Generators.. 137

7.2.5 Voltage Control of More Material Properties 138

References 139

List of Figures

Figure 2.1. Scope of material properties to be controlled by solid-state ionic motion and electrochemistry 21

Figure 2.2. Voltage control of interfacial magnetism 23

Figure 2.3. Voltage control of magnetic anisotropy using a solid-state proton pump based on hydrogen accumulation at the Co/GdO_x interface. 24

Figure 2.4. Interference of light reflected from a thin film layer on a substrate 26

Figure 2.5. Simulated reflected color of a SiO_2 layer on Si substrate as a function of SiO_2 thickness 28

Figure 2.6. Surface plasmon and localized surface plasmon resonance 29

Figure 2.7. Working principle of high-resolution plasmonic color printing 30

Figure 2.8. Interference color control by electrically addressable phase change of phase change materials 32

Figure 2.9. Enhanced contrast and switching speed of electrochromic devices by incorporating plasmonic nanoslits 32

Figure 2.10. Photographs of a 500 nm thick Y film capped with 20 nm Pd protection layer before and after hydrogen gas exposure at 10^5 Pa 33

Figure 2.11. Programmable plasmonic resonance and metasurfaces based on hydrogen absorption of Mg 34

Figure 2.12. Total energy (E) as a function of θ, with different external field H_z 36

Figure 2.13. Hysteresis loops measured along the easy axis when external field is applied along directions at different angles to the easy axis 37

Figure 2.14. Sublattice moment configuration of ferrimagnetic sublattices of GdFe below and above compensation temperature T_M 38

Figure 2.15. H_c and M_s of GdCo as a function of temperature (top) and polar MOKE hysteresis loops measured below and above compensation temperature (bottom) 39

Figure 2.16. Fast spin dynamics, small spin textures and ultrafast magnetic reversal using ferrimagnets 40

Figure 3.1. Schematic of sputtering system 42

Figure 3.2. Steps of photolithography using photomask or laser writer 45

Figure 3.3. Steps of pattern transfer using lift-off (top) and etching (bottom). 47

Figure 3.4. Magneto-optical Kerr effect (MOKE) 48

Figure 3.5. Magneto-optic Kerr effect measurement system with integrated focused laser and wide field capabilities 49

Figure 3.6. Ordinary (left) and anomalous (right) Hall effects 50

Figure 3.7. Device layout of voltage gated Hall cross for AHE measurement while a gate voltage is applied 51

Figure 3.8. Schematic of experimental setups for different XAS detection modes........ 53

Figure 3.9. X-ray absorption spectra of Mg-Ni at Mg K-edge before and after hydrogen absorption and after exposure to air 54

Figure 4.1. Voltage induced resistive switching 59

Figure 4.2. R_L and V_G as a function of time at room temperature 63

Figure 4.3. Possible morphology evolution during V_G application 65

Figure 4.4. Large Voltage Induced Resistance Switching 67

Figure 4.5. Dynamic resistivity modulation of $MgNi_x$ and VO_2 69

Figure 5.1. Shadow mask design for fabricating array of gating devices allowing measurement of multiple devices on thickness wedge samples. 73

Figure 5.2. Hydrogen absorption by bottom electrode 78

Figure 5.3. Electrochemical switchable solid state thin film plasmonic device 81

Figure 5.4. Electrochemical switchable color from solid state thin films 83

Figure 5.5. Measured and simulated reflectance of interference color devices with three different t_{SiO2}, before and after hydrogen loading 84

Figure 5.6. Experiment micrographs and simulated colors of yttrium gating reflection devices with different GdO_x refractive index when loaded with hydrogen. 85

Figure 5.7. Simulated colors of plasmonic switching device with different GdO_x refractive indices and different Mg hydrogen loading states 86

Figure 5.8. Switching ratio, reversibility and response time 88

Figure 5.9. Switching time dynamics of GdO_x interference device. 91

Figure 5.10. Switching transient for Mg optical switching device during hydrogenation with $V_G = 5$ V (a) and dehydrogenation with $V_G = -2$ V(b) 92

Figure 5.11. Reflected colors from Al nanodisk arrays with varying periodicities and diameters showing bright colors. 95

Figure 5.12. Reflected images of voltage controlled plasmonic color devices with Au nanodisk arrays (top) and Al(20 nm)/Au(4 nm) nanodisk arrays (bottom) as fabricated, after $V_G = 5$ V was applied and after -5 V was applied subsequently 96

Figure 5.13. Reflected images of voltage controlled plasmonic color device with a 1nm thick Co layer as fabricated, after $V_G = 5$ V was applied and after -5 V was applied subsequently 96

Figure 5.14. Color pixel that shows color changes through yellow, red and blue 97

Figure 5.15. High resolution demonstration 98

Figure 6.1. Device layout of reversed domain (left) and skyrmion bubble generators (right) ... 104

Figure 6.2. Gating of dominant sublattice and compensation temperature (T_M) of GdCo 107

Figure 6.3. a, H_c and MOKE loop polarity versus Gd atomic percent of GdCo. b, MOKE hysteresis loops at x = 43.8 and x = 45.7 108

Figure 6.4. Schematic illustration of water splitting and hydrogen pumping by applying positive V_G 110

Figure 6.5. MOKE hysteresis loops before and after applying V_G = +3 V for 180 s under different gas environments 112

Figure 6.6. Differential wide-field MOKE images and experimental procedures to verify the origin of MOKE polarity flipping. 114

Figure 6.7. Ab initio calculations of the impact of hydrogen intercalation 116

Figure 6.8. Electrical measurement of reversible toggling of the dominant sublattice with gate voltage 118

Figure 6.9. Cycle time as a function of cycle number when the device was cycled using V_G = +2.3 V and -0.5 V 119

Figure 6.10. 180° switching of the Néel vector and the exchange bias field by gate voltage 121

Figure 6.11. H_c and V_G as a function of time showing that a single 5 ms +7 V V_G pulse can switch the dominant sublattice at room temperature. 123

Figure 6.12. H_z, V_G and AHE signal as a function of time in the vicinity of the V_G pulse showing a delay of Co moment switching after the V_G pulse. 124

Figure 6.13. Reversed domain generator based on GdCo voltage gating 126

Figure 6.14. Sequence of wide field MOKE contrast images showing the movement of the generated skyrmion bubbles with lateral current pulses injected from right to left.................... 127

Figure 6.15. AHE hysteresis loops measured with out-of-plane field and in-plane field as fabricated, when the gate voltage was held at different levels, and when a negative gate voltage was applied to reverse the hydrogen loading.. 129

Figure 7.1. Passive addressing of an array of voltage-controlled devices................................. 136

Figure 7.2. Gate voltage controlled hydrogen loading/unloading device showing reversible deformation with gate voltage application... 138

Chapter 1 Introduction

1.1 Motivation

The field of traditional materials science and engineering is often characterized by understanding and utilizing the relation between material structure, property, processing and performance[1]. When a need for certain performances arises, it is translated to the corresponding desired material properties. In order to achieve the desired material properties, certain material structure or composition need to be established, and implemented by processing techniques. This paradigm assumes that properties of materials are defined during processing and are not actively changed during usage. With the advancement of information technology, the demand is higher than ever before for devices to adapt to different working states and to have additional functionalities. Dynamic control of material properties allows the devices to adapt to different needs, to maintain optimal performance for broader range of conditions, and to achieve additional levels of functionality, enabling applications such as reconfigurable electronics[2], reconfigurable antennas[3], active optical devices[4], and energy efficient data storage.

One promising way of realizing dynamic control of materials properties was proposed in the PhD thesis by Uwe Bauer[5]. The concept was referred to as "voltage programmable materials". The approach involves using solid-state ionic movement and electrochemical reactions to change metal/metal-oxide interfaces based on a solid-state thin film stack[6]. It was shown that such an approach can generate unprecedentedly large modifications of the magnetic anisotropy of ferromagnetic thin films. The approach was extended by the work of Aik Jun Tan, showing that a solid-state proton pump can be realized by putting a solid electrolyte layer on top of the

ferromagnetic metal thin film, followed by a thin layer of top electrode[7–9]. When a small voltage is applied to the top electrode, water from the ambient is dissociated to form protons and oxygen. The protons are driven towards the bottom electrode by the electric field and receive electrons to form neutral hydrogen. The process happens rapidly at room temperature and the magnetic anisotropy can be controlled with good cyclability. The method is also compatible with microelectronic fabrication and can potentially enable highly localized control.

Since a wide range of material property can potentially be reversibly changed by redox reactions and hydrogenation, in the thesis, we extend the mechanism to realize effective modulation of the electrical and optical properties and extend the modulation of magnetic properties to include the control of ferrimagnetic order. The result reveals a promising path towards voltage programmable materials, since the modulation is effective, and the approach is highly versatile with very simple structure that has the potential to be integrated to existing devices without affecting other functionalities. This work may help develop a better understanding of the underlying mechanisms as well as point to several applications including neuromorphic computing, data storage, optical modulators and color displays.

1.2 Thesis Outline

The thesis is arranged into 7 chapters. Chapter 1 provides a preliminary introduction to the focus of the thesis – voltage control of material properties using ionic transport and electrochemical reactions and describes the motivation of the research presented in the thesis.

Chapter 2 provides the scientific background and an overview of the major concepts that are critical to understanding the results presented in the thesis. The chapter includes the concept of

voltage-controlled material properties and previous work on this topic. In addition, because the thesis presents results of voltage control of the electrical, optical and magnetic properties of materials, this chapter also introduces thin film interference, plasmonics, and magnetic properties with emphasis on ferrimagnets.

Chapter 3 provides a detailed description of the major experimental methods used in the thesis. The chapter starts off with the sample fabrication methods used in the thesis – sputtering and patterning. It then describes the measurements to characterize the electrical and magnetic properties such as reflection spectroscopy and polar magneto-optical Kerr effect (MOKE) measurements. In the end of the chapter, we also present the basic working principle of X-ray absorption spectroscopy (XAS) and X-ray magnetic circular dichroism (XMCD) for getting element-specific chemical and magnetic information from thin film gating devices.

Chapter 4, 5 and 6 present the main results of the thesis: voltage control of the electrical, optical, and magnetic properties respectively. In Chapter 4, we show that we can control the resistance of a lateral conductive thin film channel through reversible redox reaction gated by a voltage. The chapter demonstrates a proof of concept three terminal resistive switching device and reveals that the mechanism may enable a new technique to quantitively characterize ion diffusion and electrochemical reaction in thin film stacks as they are otherwise difficult to probe. In Chapter 5, we demonstrate voltage gated optics enabled by solid-state proton pumps. We show that the optical properties of both the electrolyte and the electrodes can be reversibly controlled by a voltage, and show demonstrations of several different implementations of the approach including voltage-controlled transmission, reflective color and switchable plasmonic colors. In Chapter 6, we shift our focus to voltage control of ferrimagnetic order. We show that a solid-state proton pump can

largely change the relatively amplitude of sublattice magnetic moments of GdCo, enabling voltage induced 180-degree magnetic switching.

Chapter 7 summarizes the findings of the thesis and discuss their potential impact and applications followed by a brief list of some possible future work to fill the knowledge gap and to explore uncharted territory in voltage-controlled material properties.

Chapter 2 Background

2.1 Previous Work on Voltage-Controlled Material Properties

The thesis is based on the enabling works of Uwe Bauer[5] and Aik Jun Tan[9], which demonstrated that voltage induced ionic motion and electrochemical reactions provide an effective route towards voltage control of magnetism of interfaces[6,10,11]. The method works by voltage controlled ionic motion and electrochemical reactions that change the composition of the interfaces and the materials. Comparing traditional methods of voltage-controlled magnetism that uses purely electronic effects, the ionic counterpart enables much larger magnetic property modulation. Besides magnetic properties, there are other material and interfacial properties that depends on the composition of materials such as electrical, optical and chemical catalytic properties as shown in Figure 2.1. The thesis expands the scope of the voltage-controlled materials properties using solid-state ionic motion and electrochemical reactions to also include controlling electrical, optical properties. The thesis also expands the scope of the control of magnetic properties to include the control of ferrimagnetic order.

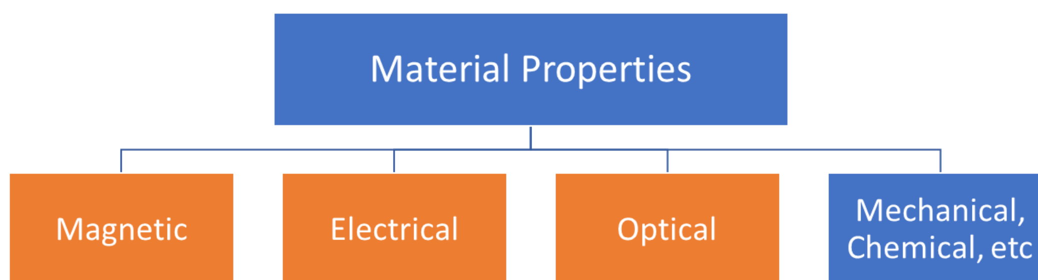

Figure 2.1. Scope of material properties to be controlled by solid-state ionic motion and electrochemistry.

Using voltage to modify magnetic properties using solid-state ionic motion was first demonstrated by Bauer et al[6]. In a Ta/Pt/Co/GdO_x/Au heterostructure as shown in Figure 2.2a. By grounding the bottom Ta/Pt/Co layer and applying a negative gate voltage to the Au top electrode, the Co layer could be oxidized, changing the anisotropy landscape of the magnetic layer. Figure 2.2b shows the MOKE hysteresis loops of the device during a sequence of gate voltage applications. The loops indicate that the magnetic anisotropy changed from favoring perpendicularly magnetized state to favoring in-plane magnetized state after applying a negative gate voltage. The reaction is non-volatile as the Co redox state remains unchanged when the device is set to open circuit and no external voltage is applied. In addition, with a reversed voltage applied to the device, the oxidation process can be reversed, and the Co layer regains the perpendicularly magnetized state. The redox reactions of Co were confirmed by electron energy loss spectroscopy (EELS) as shown in Figure 2.2c and X-ray magnetic circular dichroism (XMCD) analyses[6,12]. The work demonstrated that reversible, non-volatile redox reactions can be induced by a gate voltage applied to such solid-state thin film structures, and demonstrated that the magneto-electric efficiency of the change of magnetic anisotropy is on the order of 5000 fJ $V^{-1}m^{-1}$, which is orders of magnitude larger than about 10 fJ $V^{-1}m^{-1}$ previously reported through a purely electric field effect[13]. In addition, the structure can be made to be CMOS process compatible, paving ways towards applications in magnetic memory and logic devices.

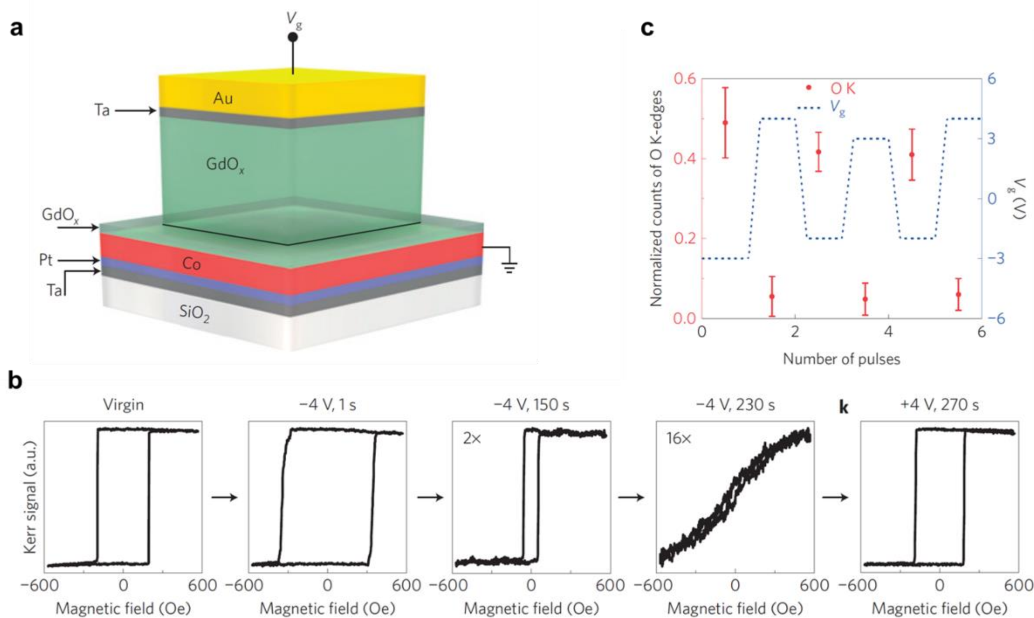

Figure 2.2. Voltage control of interfacial magnetism. a, Schematic illustration of the device layer structure and geometry. **b,** Polar MOKE hysteresis loops at gate region following gate voltage sequence showing reversible magnetic property control. **c,** in situ EELS oxygen K-edge count rate of Co layer normalized to that of GdO_x layer following gate voltage pulses applied to the device. Reprinted with permission from Ref [6].

The work by Uwe et al. focused on redox reactions in the solid-state structure to achieve reversible control of magnetic properties. Because the control of magnetic properties are induced by redox reactions, these systems usually have the problem of poor reversibility due to chemical and structural changes of the magnetic layers during cycling. Tan et al. recently showed that protons are the major mobile ions that are responsible for the gate voltage induced redox reactions[7,8]. The redox reactions of Gd seen in Uwe's work can be explained as follows: when a negative gate voltage is applied, water molecules that are stored in the GdO_x layer get split to oxygen and hydrogen; the oxygen oxidizes cobalt layer and the hydrogen migrates towards the top electrode in the form of protons. The work also showed that the structure serves as a solid-state proton pump that enables fast and reversible magnetic property control using a modest gate voltage. The protons

are sourced from hydrolysis of water from the gas ambient. The operation schematics of the mechanism is shown in Figure 2.3.

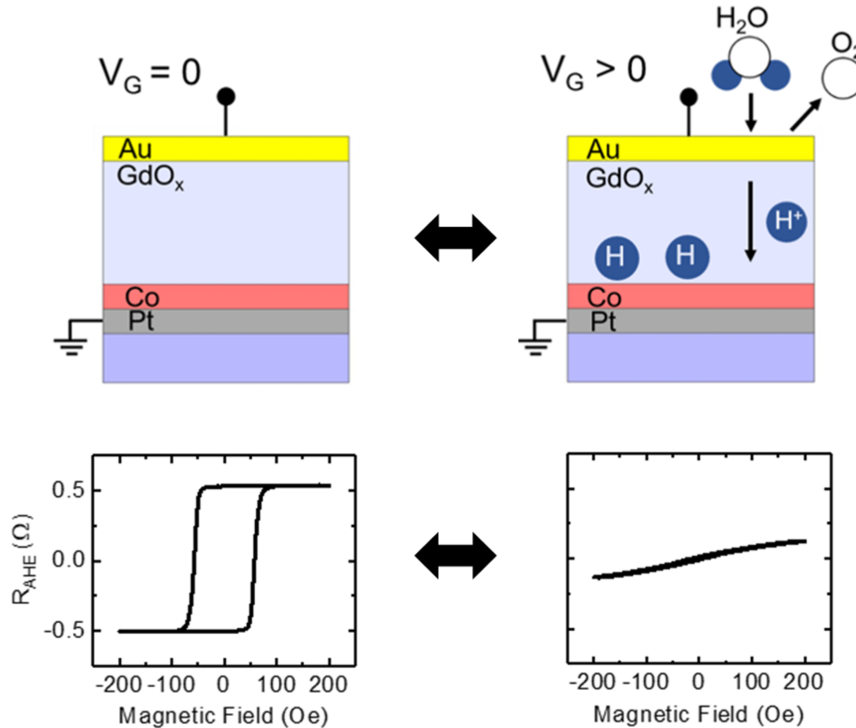

Figure 2.3. Voltage control of magnetic anisotropy using a solid-state proton pump based on hydrogen accumulation at the Co/GdO$_x$ interface. (a) Schematic illustration of the device structure and operation principle. (b) AHE hysteresis loops when V_G was cycled between 0 V (left) and +3V (right). Adapted from Ref[7].

The example device has a layer structure of Ta/Pt/Co/GdO$_x$/Au. When a positive voltage of amplitude $\gtrsim$ 1.2V is applied to the top electrode, the water content from the ambient is hydrolyzed at the top electrode, producing protons and oxygen through an oxygen evolution reaction. The protons are driven to the bottom electrode by the electric field in the oxide via a Grotthuss-type mechanism enabled by the water content of the oxide matrix. The electrochemical reactions of the system are:

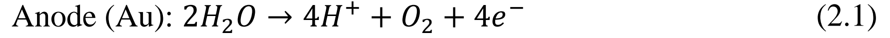

$$\text{Anode (Au): } 2H_2O \rightarrow 4H^+ + O_2 + 4e^- \tag{2.1}$$

$$\text{Cathode (Pt): } 4H^+ + 4e^- \rightarrow 4H \tag{2.2}$$

The hydrogen accumulated at the GdO_x/Co interface turns off the perpendicular magnetic anisotropy as shown in Figure 2.3 (bottom). The process can also be reversed by applying a reversed gate voltage or just by short circuiting the device.

In the thesis, we expanded the scope of the voltage-controlled materials properties using solid-state ionic motion and electrochemical reactions to also include controlling electrical, optical properties and magnetic properties of ferrimagnets. The sections below will discuss the background of optical and magnetic properties. The focus will be brief introduction of the optical effect and works in the literature to dynamically change optical properties. For magnetic property control, the basics of magnetic anisotropy, hysteresis loop and ferrimagnets will be introduced.

2.2 Optical Properties

The thesis includes voltage control of optical properties and its applications in realizing the control of several optical phenomena including interference and plasmonics, which will be introduced in this section. In addition, this section will present related works on the dynamical control of optical properties.

2.2.1 Thin Film Interference

Thin film interreference refers to the phenomenon where light reflected by the upper and lower interfaces of a thin film layer interfere with one another, changing the reflection and/or transmission of the light[14]. Thin-film interference is the underlying reason for the colors seen from thin oil layers on water and from soap bubbles. The colors of several natural species are from thin film interference such as the Aglais io butterfly and buttercup flowers[15–18]. With proper design of the configurations of the layers, thin film interreference can be applied to make anti-reflection coatings and optical filters[14].

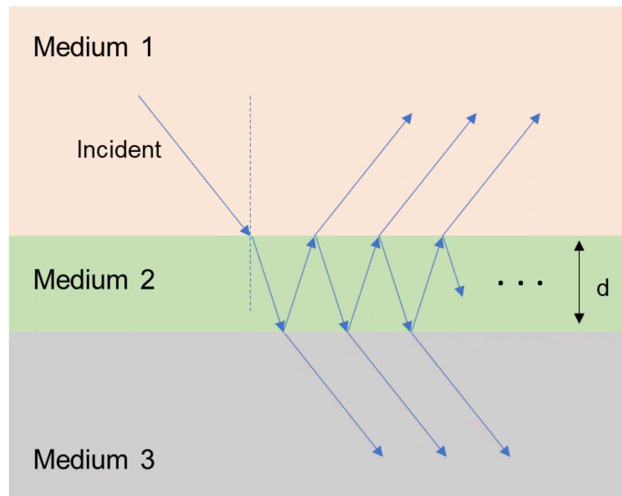

Figure 2.4. Interference of light reflected from a thin film layer on a substrate.

Figure 2.4 illustrates the optical path of interference when light from a medium incident on a thin film stack with a thin layer on a thick substrate. The structure consists of one finite layer of thickness d (the thin film, Medium 2) between two semi-infinite layers (Medium 1: the medium light incidents from, Medium 3: the substrate). When the incident wave reaches the interface between Medium 1 and Medium 2, part of it is reflected and part of it transmits through with the angle defined by Snell's law. If the refractive index of Medium 2 is higher than that of Medium 1, the phase of the reflected light is changed by π. When this transmitted light reaches the interface

of Medium 2 and Medium 3, again, the light is partially reflected and partially transmitted. The reflected light travels towards the top interface and gets partially transmitted and partially reflected at the top interface. The process keeps going while the intensity of the light drops as it progresses. The transmitted light and the reflected light are effectively the interference of all the light coming out with different phases and amplitudes from the layers towards the corresponding directions.

The calculation of the reflectance and transmittance from a thin film stack can become complicated when the number of layers increases because the interaction of light bouncing from all the interfaces needs to be taken into consideration to get an accurate result. The transfer matrix method[19] provides a simple way of calculating the reflectance and transmittance of multilayer stacks. In the thesis, the interference color calculation is carried out using tmm[20], a python package for simulating light propagation in multilayer films.

The understanding of thin film interference comes handy for estimating the thickness of a thin film layer on substrates. Figure 2.5 shows the simulated reflection color of a SiO_2 thin layer on Si substrate when looked at from air, as a function of the layer thickness. The refractive indices of Si and SiO_2 are taken from ref.[21,22]. The reflected color can be therefore used to estimate the layer thickness. Interpretations need to be carried out carefully since the perceived color depends on the illuminant and the color perception, and similar color can be seen from stacks with very different structures.

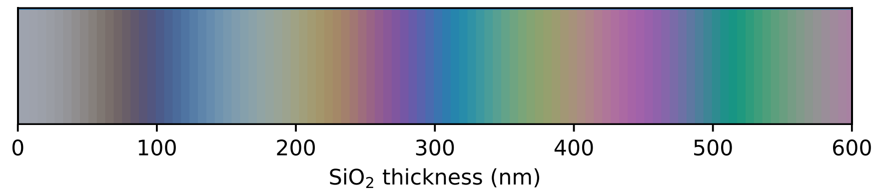

Figure 2.5. Simulated reflected color of a SiO_2 layer on Si substrate as a function of SiO_2 thickness.

Because the reflected spectrum depends on the thickness and optical properties of the layers, voltage-controlled interference color is demonstrated later in the thesis where the change of effective refractive indices and thicknesses induce changes in the color of the devices.

2.2.2 Plasmonics

When light interacts with a metal, the free electrons in the metal can be excited to form coherent charge density fluctuations on the surface. These excitations are called surface plasmons (SPs)[23]. Surface plasmons couple light to the metal surface strongly and are capable of confining the light in an area that is smaller than the diffraction size[24]. Figure 2.6a illustrates surface plasmons at the interface between a metal and a dielectric material. The dispersion curve for a surface plasmon mode as shown in Figure 2.6b indicates that SPs have greater momentum (smaller wavelength) than a free space photon of the same frequency.

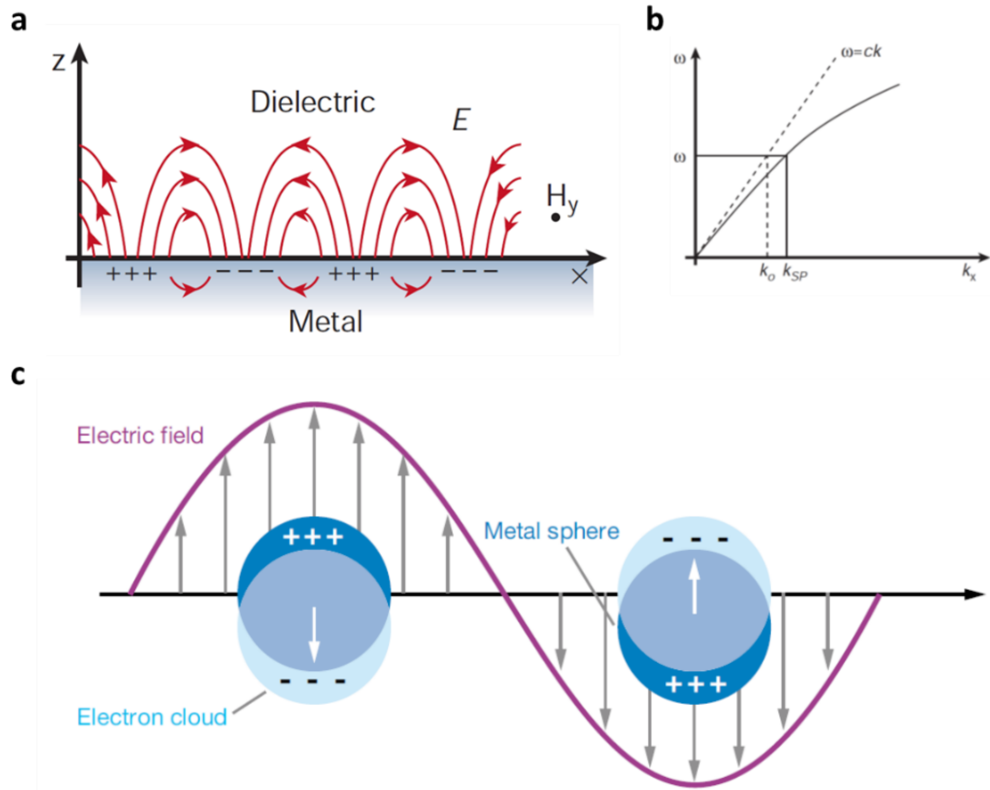

Figure 2.6. Surface plasmon and localized surface plasmon resonance. a, Schematic diagram illustrating SPs at the interface between a metal and a dielectric. **b,** Dispersion curve for a SP mode showing that it has greater momentum than a free space photon of the same frequency. **c,** Schematic diagram illustrating a localized surface plasmon. Reprinted with permission from Refs[25,26]

Figure 2.6c illustrates that when light interacts with particles that are smaller than the incident wavelength, it leads to a plasmon that is confined and oscillates locally near the particle. The frequency at which the plasmons are oscillating is called localized surface plasmon resonance (LSPR). At such frequency, the intensity of localized electromagnetic field can be greatly enhanced. The resonance is highly sensitive to the refractive index of the surrounding dielectric. As a result, the phenomena enables applications such as chemical sensing[27] and information processing[28] as well as optical components such as lenses, mirrors and polarizers[29]. Besides the optical properties of the particle and the surrounding medium, LSPR is also sensitive to the size of

the particles but is less sensitive to the distance between adjacent particles or the periodicity of the particles are arranged as a periodic array. A general trend is that as the particle size increases and as the refractive index of the surrounding dielectric increases, the LSPR peak shifts to longer wavelengths. One interesting application of plasmonics is to produce structural colors, as shown in the work by Kumar et al., showing color printing beyond the diffraction limit[30,31].

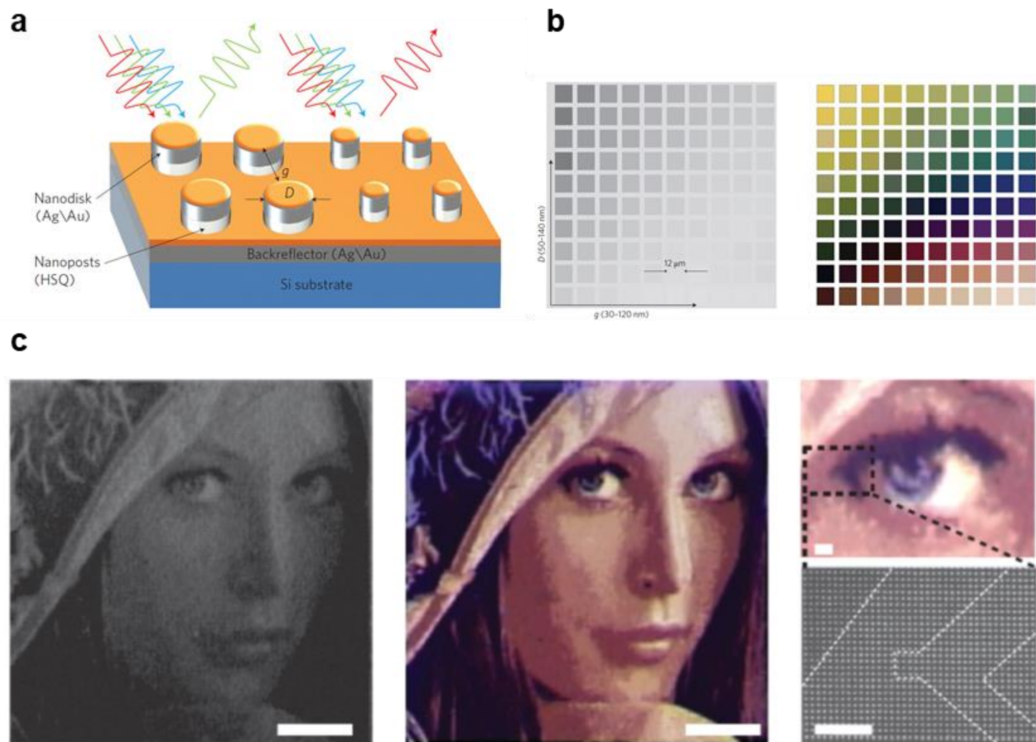

Figure 2.7. Working principle of high-resolution plasmonic color printing. a, Device structure and schematic illustration of interactions of light with the nanostructures. **b,** Optical micrographs of arrays of nanostructures with different diameters D and gaps g before (left) and after metal deposition (right). **c,** Optical micrographs of the Lena image before (left) and after (right) metal deposition. Scale bar, 1 µm. The optical micrograph and SEM image of a zoomed-in region are shown on the right. Scale bar, 500 nm. Reprinted with permission from Ref.[30]

2.2.3 Dynamic Control of Optical Properties

Tuning of the optical properties of materials by electrical means has been an active field of research. Efforts have been focused on liquid crystal and electrochromic materials to achieve such tunability[32–37]. These means of controlling optical properties have enabled numerous important applications such as tunable optical filters and displays. Emerging fields of photonics such as reconfigurable metamaterials demand increasingly localized control of optical properties, an attribute which conventional technologies such as liquid crystals have difficulty to achieve due to the thickness requirement. The use of electrochemistry and ion migration to modulate optical properties has been realized in electrochromic devices and switchable mirrors[34,38], though conventional electrochromic devices require an ion storage layer[39], which complicates the layer design.

Recently, phase change materials have been studied for highly confined electrical tuning of optical properties[40,41]. As shown in Figure 2.8, the phase change of $Ge_2Sb_2Te_5$ (GST) in a thin film stack can be induced by electrical pulses, and the interference color of the film can be controlled locally. The nucleation-dominated crystallization is a drawback that may prevent uniform reversible switching by electrical stimuli[42].

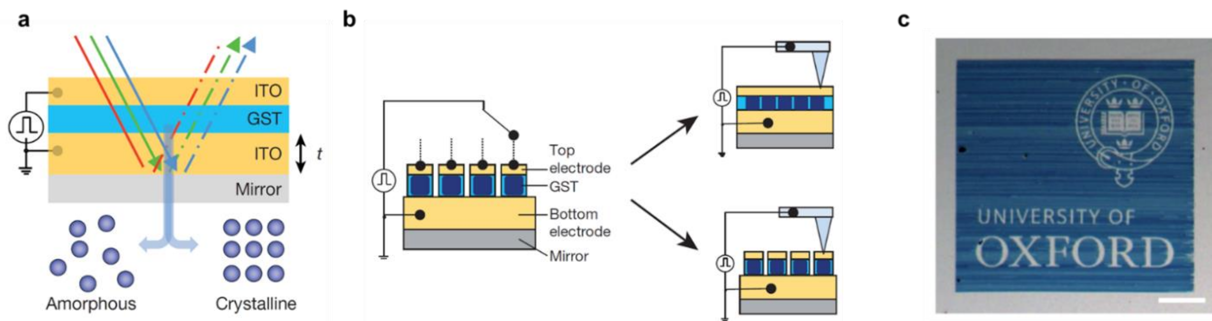

Figure 2.8. Interference color control by electrically addressable phase change of phase change materials. a, Schematic representation of the thin-film material stack. The crystallization/amorphization the thin GST layer induces a color change of the stack. **b,** Schematic illustration of the electrically induced color changes. **c,** Electrically constructed image. The blue regions are regions where the phase is transformed. Reprinted with permission from Ref.[41]

Combining plasmonics with actively controlled optical properties enables active plasmonics. On one hand, the approach gives flexibility to plasmonic devices whose optical response is usually fixed after fabrication. On the other hand, because plasmonic response is highly sensitive to the optical properties of the metallic structure and the surrounding dielectric medium, and therefore the inclusion of plasmonics structures can enhance the speed and amplitude of actively controlled optical devices. Figure 2.9 shows an example of combining electrochromic switching with plasmonic nanoslits to achieve fast optical switching with high contrast.

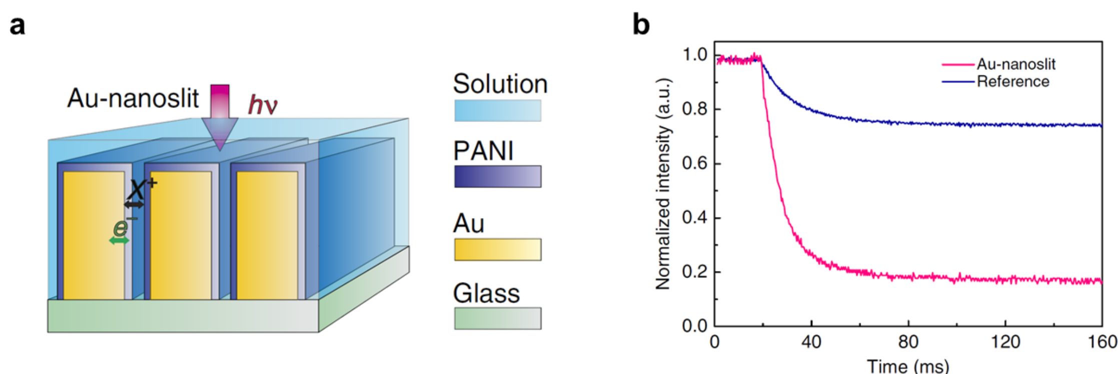

Figure 2.9. Enhanced contrast and switching speed of electrochromic devices by incorporating plasmonic nanoslits. a, Schematic diagram of an electrochromic electrode incorporating Au-nanoslit array. **b,** Transmitted light intensity as a function of time for Au-nanoslit and reference planar electrodes showing faster switching of devices with plasmonic nanoslits. Adapted from Ref.[37]

Controlling optical properties with hydrogen loading/unloading has been an active field of research recently. Thin metal films such as Mg and Y can be reversibly transformed into an optically transparent state by hydrogenation[43]. Figure 2.10 shows an example of a switchable mirror with

yttrium thin film. The reflective layer became transparent after hydrogen exposure. Following the initial work on yttrium, hydrogen-switched optics, such as mirrors[43,44] or other reflection-based optical devices[45,46], were realized with a wide range of materials such as Pd and Mg[47,48].

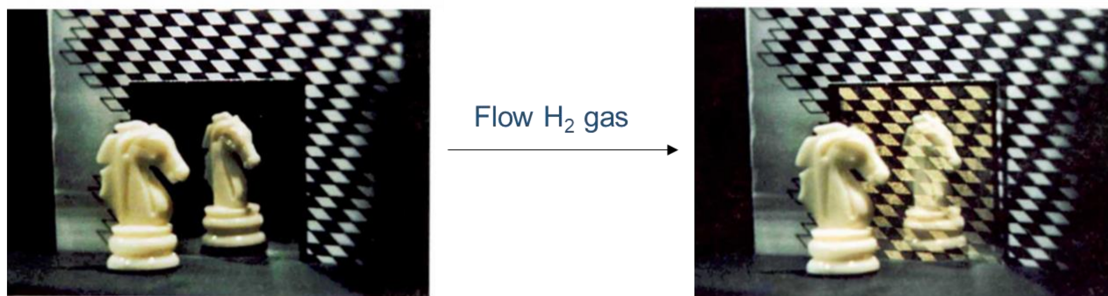

Figure 2.10. Photographs of a 500 nm thick Y film capped with 20 nm Pd protection layer before and after hydrogen gas exposure at 10^5 Pa. Reprinted with permission from Ref.[43]

Metals such as Mg are of particular interest as they can support plasmon resonances in the visible spectrum in nanostructures with suitable geometry[48]. These resonances can enable subwavelength light manipulation, and color generation with print resolutions at the optical diffraction limit[30,31,49]. As shown in Figure 2.11, hydrogen loading and unloading can serve as an effective means to change the optical response on demand to achieve active plasmonics and metasurfaces, with great potential in dynamic plasmonic color displays, dynamic holography, anti-counterfeiting technologies, and information encryption[46,50–53].

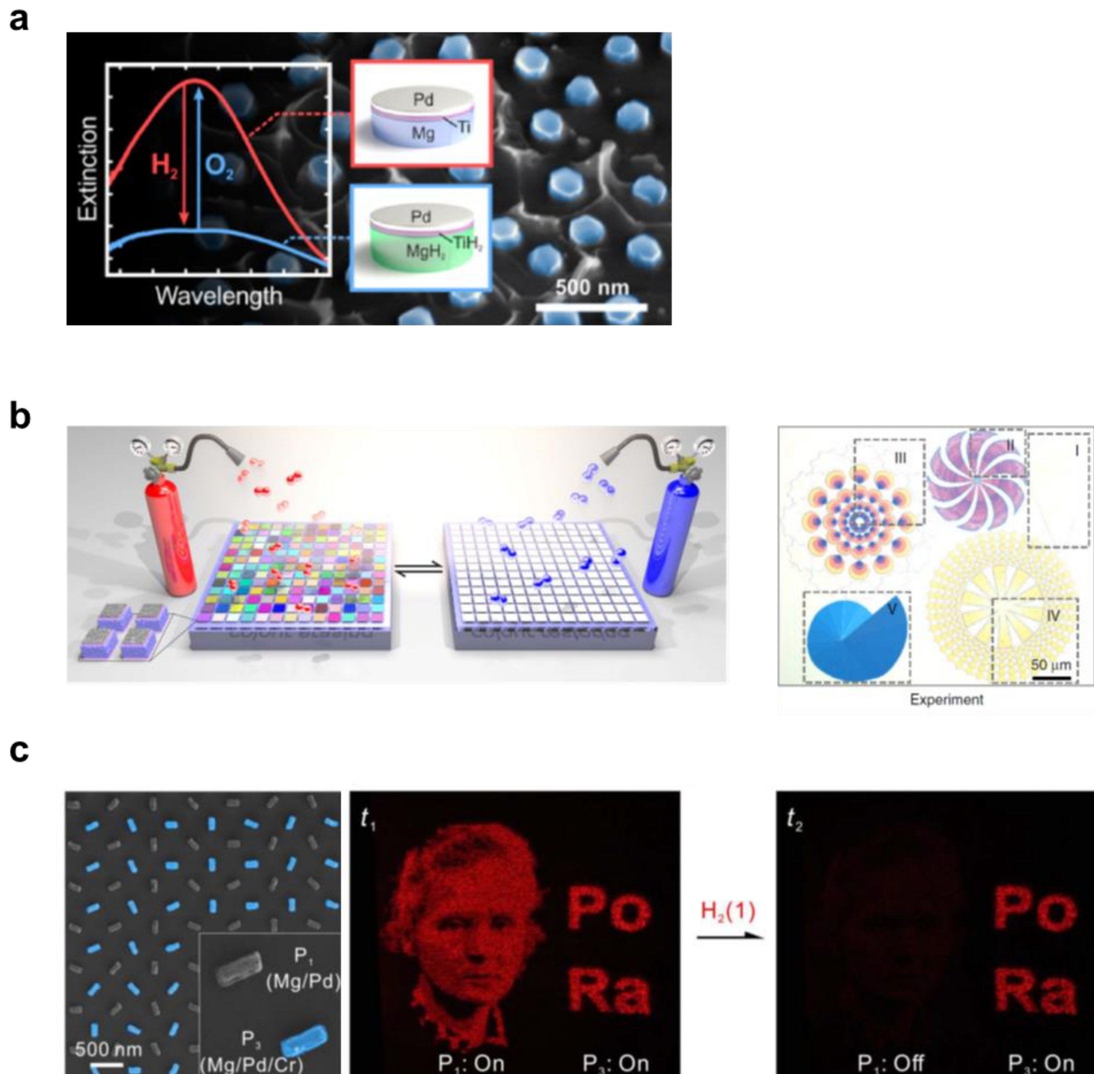

Figure 2.11. Programmable plasmonic resonance and metasurfaces based on hydrogen absorption of Mg. a, Switching of magnesium particles to magnesium hydride and vice versa showing that exposure to H_2 and O_2 turns on and off the plasmonic resonance of Mg nanodisks. **b,** Working principle and optical characterization of the dynamic plasmonic color display. **c,** SEM image of the hybrid plasmonic metasurface with Mg/Pd (P1) and Mg/Pd/Cr (P3) nanorods as dynamic pixels (left). Snapshots of the holographic images before and after hydrogenation (right). Reprinted with permission from Refs.[48,50,51].

In most work so far, such optical response switching is achieved through exposure to hydrogen gas in an enclosed chamber, which is impractical for many applications. The approach turns on/off all elements at the same time which precludes addressability, i.e. local and selective switching[54].

Chapter 5 shows a way to utilize voltage gated ionic motion and electrochemical reactions to enable control of hydrogen load/unloading without the need of gas exposure and potentially achieve addressability.

2.3 Magnetic Anisotropy and Magnetic Hysteresis Loops

The magnetic anisotropy refers to the property of an anisotropic system where the magnetization tends to point in certain preferred directions[55]. The behavior can be understood from an energy minimization point of view, as in many magnetic materials, the energy required to align the magnetization vector depends on the direction. In a system with magnetic anisotropy, the magnetization vector often has a preference to align with the minimum energy axis, which is called the easy magnetization axis. Magnetic anisotropy plays critical roles in coercivity, magnetic remanence and magnetic recording. The Stoner Wohlfarth model is a widely used model for determining the energy of a single domain ferromagnet with a uniaxial magnetic anisotropy[56].The model assumes that the anisotropic energy (E_A) characterized by K of the system is

$$E_A = K \sin^2 \theta \tag{2.3}$$

where θ is the angle M makes with the anisotropy axis. With no external field, the magnetization tends to align to either the up ($\theta = 0°$) or down ($\theta = 180°$) direction and does not favor any other directions. With an external field applied, the total energy is the sum of the Zeeman energy (E_z) and the anisotropy energy, which can be expressed by

$$E = E_{\mathrm{A}} + E_{\mathrm{Z}} = K \sin^2 \theta - HM_{\mathrm{s}} \cos(\theta - \phi) \tag{2.4}$$

where H is the amplitude of the external field, M_{s} is the saturation magnetization, and ϕ is the angle the external field makes with the anisotropy axis. The model describes the magnetization of a ferromagnet with a single domain. Figure 2.12 shows the angular dependence of the total energy when an external field along $\theta = 0$ direction is applied. H_{K} is the anisotropy field, and

$$H_{\mathrm{K}} = 2K/M_s \tag{2.5}$$

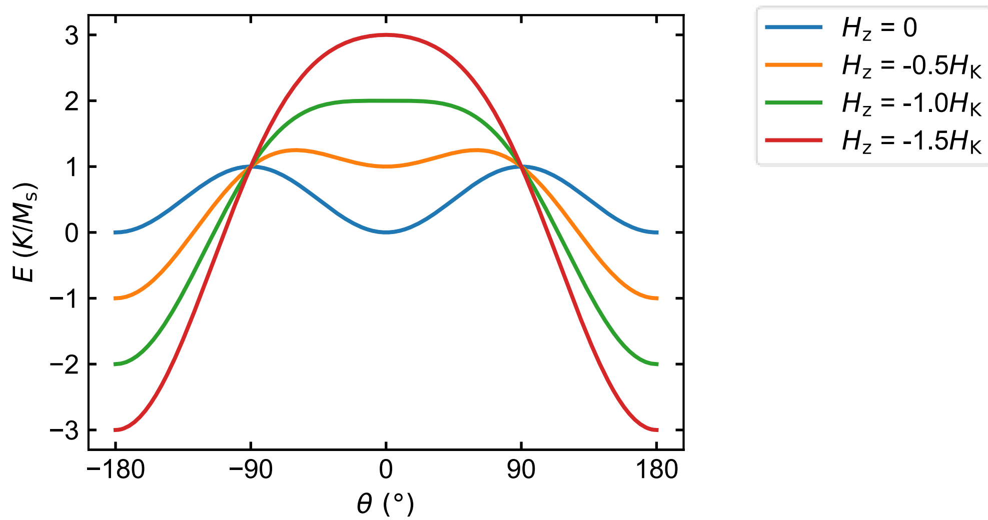

Figure 2.12. Total energy (E) as a function of θ, with different external field H_z

If the magnetization starts with $\theta = 0°$ and no external field is applied, as shown in the figure, E is at a local minimum and would stay unchanged. When a small field pointing down is applied, $\theta = 0°$ is still the local minima and the state is retained without strong energy fluctuations. With increasing field amplitude ($H_z < -H_k$), the $\theta = 0°$ state is no longer stable, and the magnetization flips to 180° to align with the external field. The non-immediate response gives rise to hysteresis behavior, and the hysteresis loops are very often used in studying the magnetic properties. In a hysteresis loop,

the magnetization is measured along one direction while an external field is swept parallel or antiparallel to the same direction. The common parameters that can be extracted from a hysteresis loop includes coercive field (H_c), remanence (M_r) and saturation magnetization (M_s). Figure 2.13 shows an example of hysteresis loops calculated from the Stoner Wohlfarth model of a ferromagnet with uniaxial magnetic anisotropy and the external field is applied in direction with 0, 60 and 90 degrees to the anisotropy axis.

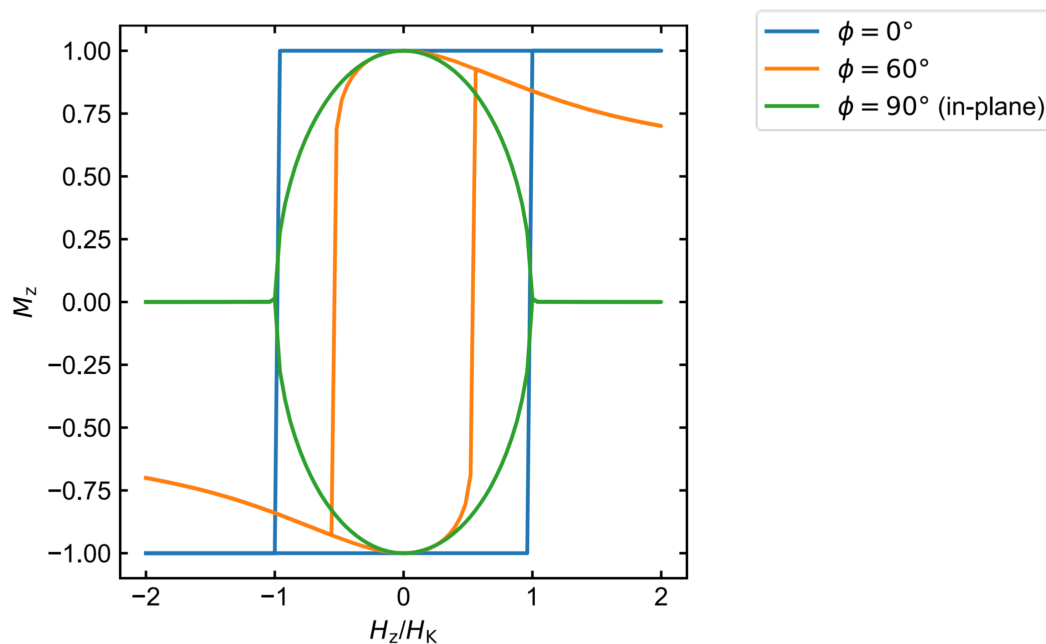

Figure 2.13. Hysteresis loops measured along the easy axis when external field is applied along directions at different angles to the easy axis.

2.4 Ferrimagnets

Ferrimagnets are composed of magnetic material with populations of atoms with opposing magnetic moments and the opposing moments are not equal[57]. As a result of the unequal

magnetization, a spontaneous magnetization exists in ferrimagnets, which distinguishes them from antiferromagnets. Figure 2.14 illustrates the magnetic moment configuration of GdFe, a rare-earth transition-metal (RE-TM) ferrimagnet.

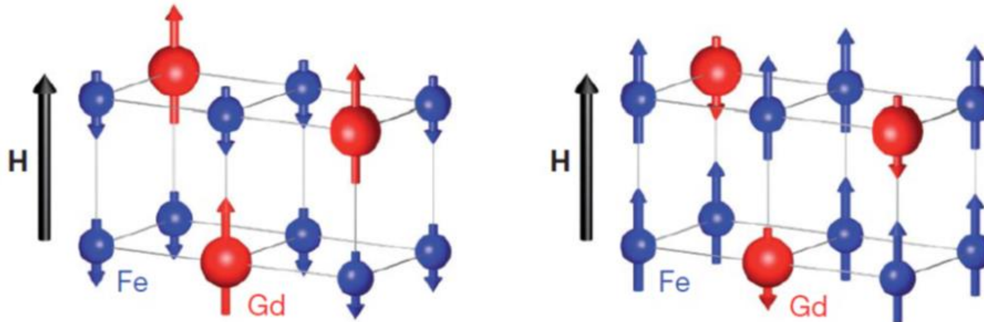

Figure 2.14. Sublattice moment configuration of ferrimagnetic sublattices of GdFe below and above compensation temperature T_M. Reprinted with permission from Ref.[58]

In RE-TM ferrimagnets, the rare earth moments generally decrease faster with temperature, which may lead to a temperature at which the two sublattice moment cancels each other, which is called the compensation temperature (T_M)[59]. For example, Figure 2.15 shows the total magnetic moment as a function of temperature for a GdCo ferrimagnetic thin film.

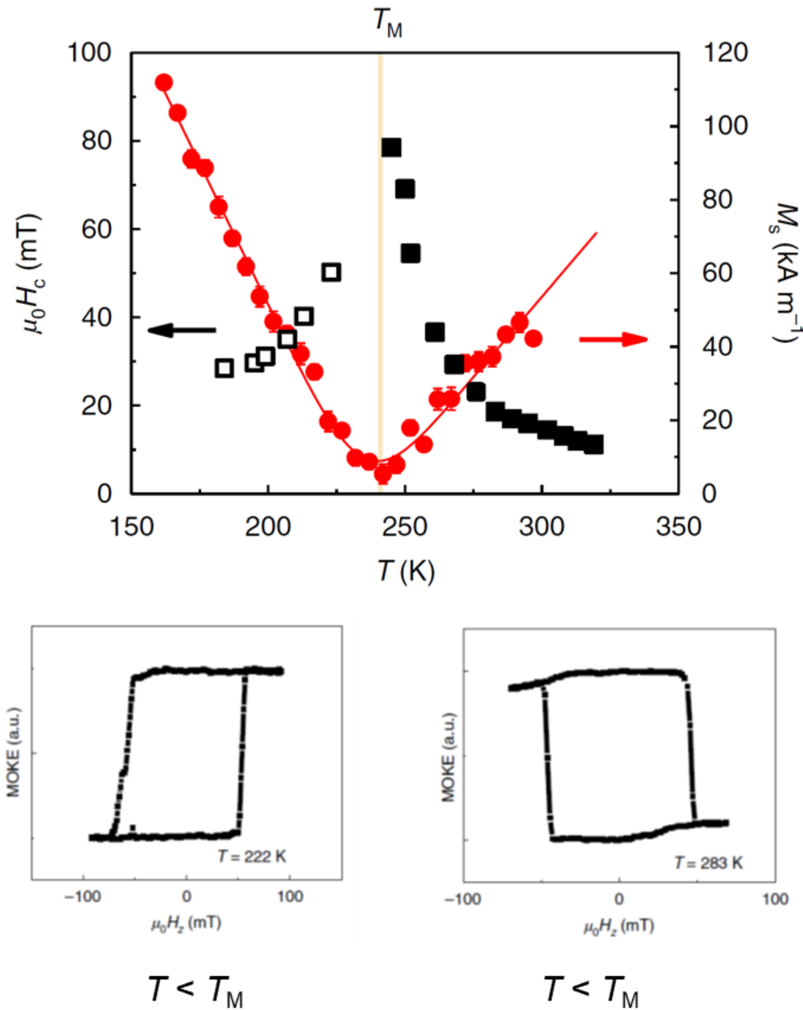

Figure 2.15. H_c and M_s of GdCo as a function of temperature (top) and polar MOKE hysteresis loops measured below and above compensation temperature (bottom). Reprinted with permission from Ref.[60]

At low temperature, the Gd sublattice dominants, and as temperature increases, the total magnetization decreases as Gd moment drops faster than that of the Co sublattice[61]. At around 240K, the magnetization goes to zero (T_M), and when the temperature increases, Co becomes dominant and the total magnetization increases with increasing temperature. Figure 2.15 also shows the coercivity of the film as a function of temperature (black boxes). H_c diverges near T_M due to vanishing total magnetization. Shown in the bottom are the MOKE hysteresis loops acquired

below and above the compensation temperature. The experimental method to acquire MOKE hysteresis loops will be discussed later in Chapter 3. The MOKE contrast of the material comes primarily from the Co[62], and therefore the sign of the MOKE signal indicates the direction of the Co sublattice moment. Because the dominant sublattice change from Gd to Co when the temperature goes above T_M, the Co lattice either tends to align antiparallel and parallel to the external field respectively, so the polarity of the MOKE hysteresis loop flips. Figure 2.16 shows that ferrimagnets allow for ultrafast optical switching[58], fast spin dynamics[60,63] and small spin textures[60].

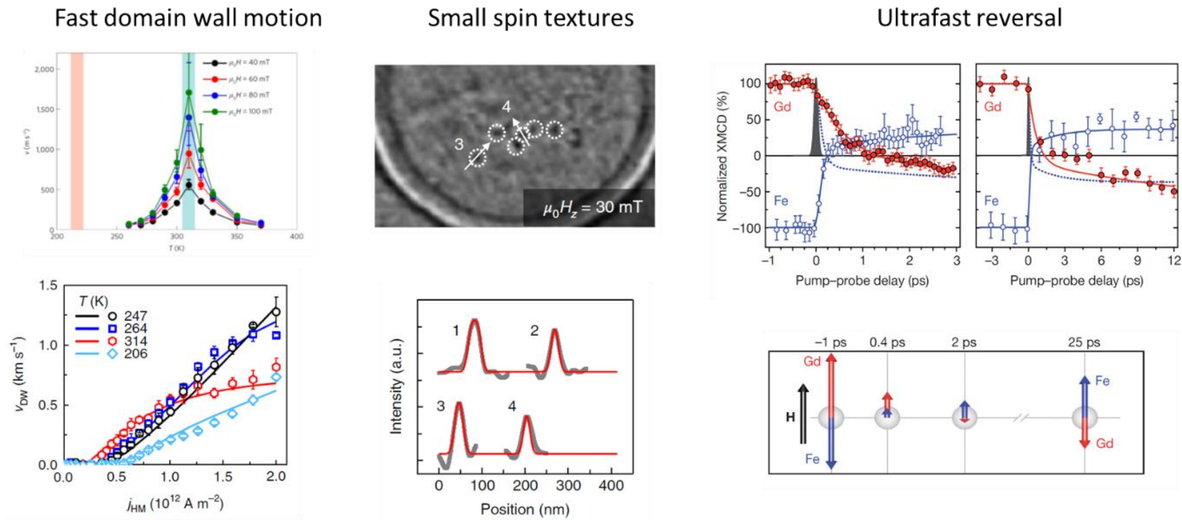

Figure 2.16. Fast spin dynamics, small spin textures and ultrafast magnetic reversal using ferrimagnets. Reprinted with permission from Refs.[58,60,63]

These exciting capabilities of ferrimagnets depend critically on their ferrimagnetic order and compensation behavior. However, the properties of ferrimagnets are fixed once they are fabricated, and a way of changing the properties of ferrimagnets is still lacking. The thesis shows that the exchange coupling and the magnetic sublattice moments can be reversibly controlled by electrical means, post-fabrication. Such capability could bring additional functionalities of existing ferrimagnetic devices, such as enabling voltage gated skyrmion steering/routing devices and devices that adapt to different environment temperatures and maintain optimal performance through precise dynamic control of compensation.

Chapter 3
Experimental Methods

3.1 Sample Fabrication

In this section, the main deposition and patterning techniques used to fabricate the samples in the thesis are discussed. The main deposition technique used in the thesis was magnetron sputtering. The patterning was mostly carried out by shadow masking and photolithography. Fine structures with feature size smaller than 2 μm were patterned using electron beam lithography, electron beam evaporation and lift-off.

3.1.1 Magnetron Sputtering

Most thin film growths in the thesis were carried out by sputter deposition. Sputtering is a physical phenomenon where energetic particles of a plasma bombard a solid material and the atoms are ejected from its surface. The ejected atoms eventually deposit on a substrate. The process can be utilized as a physical vapor deposition technique to grow thin films of fine layers[64], and has applications for both laboratory research and industrial scale production because the deposited layers can scale to a large area with good uniformity and smoothness. In addition, a wide variety of materials can be deposited using this method including metals, oxides and other insulators.

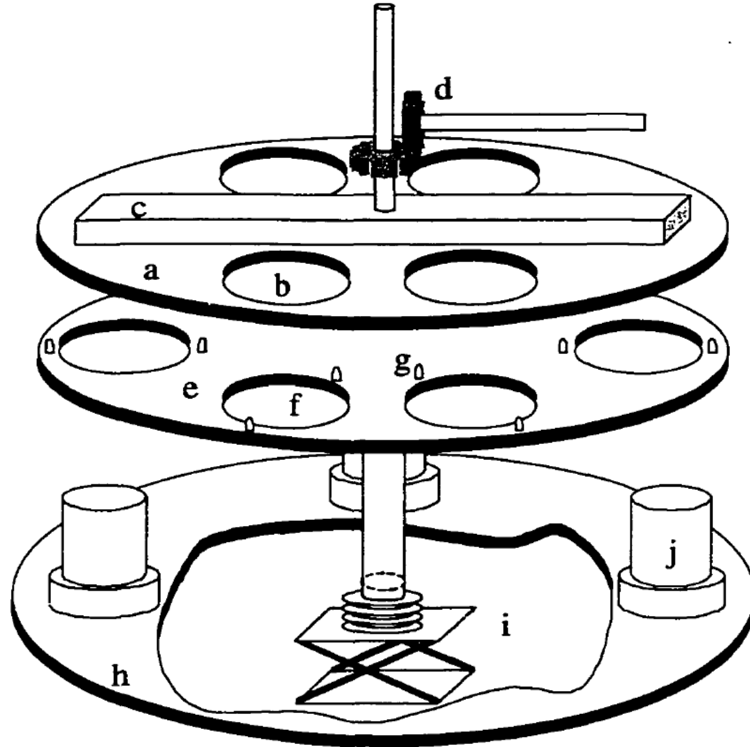

Figure 3.1. Schematic of sputtering system. (a) Substrate table. (b) Substrate holder slot. (c) Liquid nitrogen reservoir. (d) Gears for rotating the substrate table. (e) Mask table. (f) Mask slot. (g) Pins to align substrate and mask tables. (h) Chamber floor. (i) Jack and bellows below the chamber floor. (j) Chimney for sputter source. Adapted from Ref.[65]

The sputtering depositions for most of the samples presented in the thesis were carried out using a sputter system as shown in Figure 3.1. The system is equipped with 4 sputtering guns that can hold their own target materials. With a combination of a mechanical backing pump and a turbomolecular pump, the chamber can reach a low background pressure ($\sim 7 \times 10^{-8}$ Torr). Thanks to the mask holder and sample holder planetary as shown in the figure, one can change the sample and mask alignment without breaking the vacuum, which allows for growing different materials with different shapes within just one pump down session. During sputtering, Ar gas was introduced, and the flow rate and the opening of orifice were controlled to maintain a sputtering pressure of 2-3.5 mTorr. To grow metallic films, metallic targets were sputtered by using a DC

power supply in constant current mode. The system also has the capability to introduce O_2 gas while sputtering enabling reactive sputtering of oxides. To grow oxide films, either metallic targets were reactively sputtered by flowing oxygen gas during sputtering, or radio frequency (RF) sputtering was used to directly sputter off oxide targets with constant power. The rate of sputtering was calibrated for each material and deposition condition by carrying out X-ray reflectometry to measure the thickness of a film with known deposition time.

The properties of thin films of the same materials sputter under different conditions can be rather different, and the control of deposition conditions is critical in these cases. The difference in thin film properties may come from different microstructures. The microstructure of the film grown by sputtering has been well studied, and the zone structure model[66] is a widely accepted qualitative model of the expected microstructure for different sputtering temperature and Ar pressures. For example, here we show that high deposition pressure potentially leads to porous film structures. As shown in Table 3.1, when grown under normal Ar pressure, SiO_2 has a relatively dense structure. When the film was grown at much higher sputtering pressure, the resulting film was less dense. The control over sputtering parameters offers a way for optimizing the proton conduction of solid electrolyte.

Table 3.1. Effect of sputtering pressure on the rate and density of SiO_2 layer deposition

Argon Pressure	Rate (nm/min)	Density (g/cc)
3 mTorr	15.5	2.3
15 mTorr	3.5	1.8 (~20% void)

Sputtering has poor directionality due to the high kinetic energy of the particles going to the substrate and high gas pressure. When depositing on patterned photoresist for lift-off, sputtering may result in side-wall coverage preventing effective lift-off and leaving residues on the edge.

Getting larger resist undercut or using a double layer resist recipe as we describe in the next section may help alleviate the problem. For very fine structures with feature size smaller than a few hundred nanometers, evaporation instead of sputtering is strongly recommended since it is more directional, resulting in little sidewall coverage and allows for a clean lift-off.

3.1.2 Lithography

Shadow mask lithography is heavily used in the thesis as a simple technique to make pattern structures conveniently and at low cost. In the thesis, the technique simply involves using a laser cut mask to selectively cover the substrate, followed by film deposition. After the film deposition, the mask is removed, and one gets substrates with thin film layers of the desired pattern. Due to the unavoidable gap between the mask and the substrate, and the non-directionality of sputtering deposition, one gets broadening and blurring of the features near the edge. The precision of laser cutting also limits the reproducibility of the technique. Due to these limitations, the technique is not suitable for fine structures. With reasonable effort, a 100 μm resolution is achievable with extra care to make sure the mask sits flat without warping on the substrate. The technique not only is low cost, but also has the advantage that no photoresist, photomask, exposure, mechanical spinning, or heating is needed so that the sample can be protected from heating, chemical or mechanical damage. In this thesis, shadow masking is used whenever possible to save time and reduce cost.

Photolithography is the process of forming a pattern in a layer of photosensitive resist by selectively exposing the areas using light. A common photolithography process involves first spin coating the photo resist, then through a mask with patterns, exposing the substrate to a UV light

that induces reactions of the resist and changes the solubility of the resist. The solubility increases by light exposure for positive photoresists and decreases for negative photoresists. Finally, the sample is immersed in a solution to dissolve selected areas of photoresist. The step is called developing. Figure 3.2 shows an example of the photolithography process. Instead of using a mask with a pattern to selectively block the light, it is also possible to use direct laser writing to selectively expose the photoresist. Compared to using a mask, which is fixed once made, direct laser writing offers faster iteration time as one has the freedom to generate arbitrary patterns and does not need to wait for the masks to be made and shipped, at the cost of lower throughput since the exposure is serial and takes more time to expose a larger area. In the thesis, we mainly used direct laser writing using a Heidelberg µPG 101 Micro Pattern Generator. For the patterning of the samples studied in the thesis, we used a double layer resist recipe that consists of PMGI from MicroChem as the bottom layer, and S1813 from MICROPOSIT as the top layer. For laser writing, 7 mW laser power with 20% pulse duration was used. MICROPOSIT MF-CD26 developer solution was used to develop the photoresist.

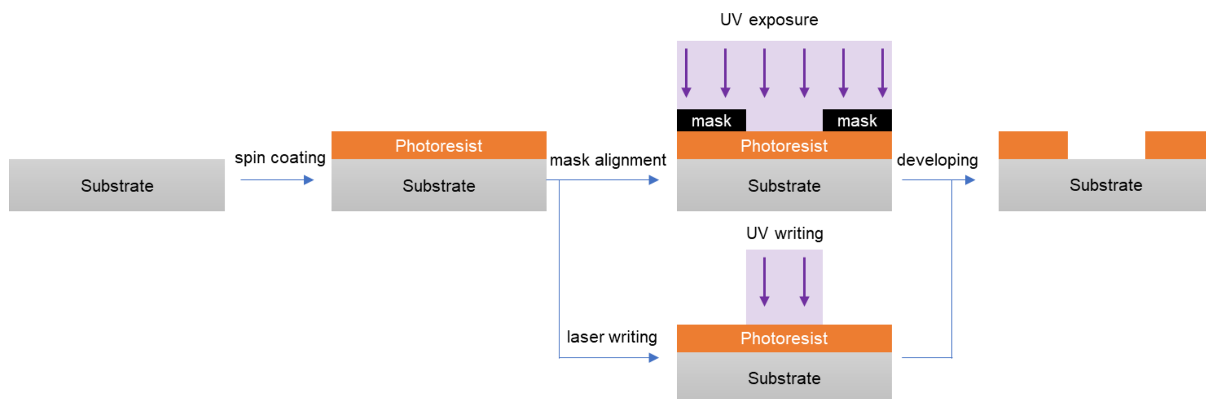

Figure 3.2. Steps of photolithography using photomask or laser writer. Positive photoresist is used here as a demonstration.

The adhesion of resist to the substrate is critical for successful patterning especially for small and high aspect ratio features. With poor adhesion, the developed resist may deform and displace, when the adhesion is bad, the spin coating of resist may even result in uncovered regions on the substrate. An adhesion promotor such as polydimethylsiloxane (PMDS) can be used to promote adhesion. The physiosorbed water content on the oxide may cause poor adhesion. The author found that heating the sample above 100°C for a few minutes before spin coating also promotes the adhesion of resist for successful patterning.

In the thesis, two different methods were used to transfer the pattern from the photoresist to thin film layers. The two methods are shown in Figure 3.3. The first method is lift-off, where we first spin coat, expose and develop a photoresist layer, and then use the patterned photoresist as a mask for thin film deposition, and then the unwanted material along with the photoresist is removed by dipping the sample in resist stripping solution. The other method is by milling, where the layer is first deposited uniformly on the substrate, and then the photoresist is put on and patterned. Next the unwanted material is milled away by ion bombardment using the patterned photoresist as a mask. The milling method has the advantage of having a clean edge but also has the disadvantage of the need to control the milling time so that it does not mill away or damage the layers underneath. A mass spectrometer can be used to determine the end point of the milling. Ion milling may also change the property of the unprotected layers in the bottom during the process.

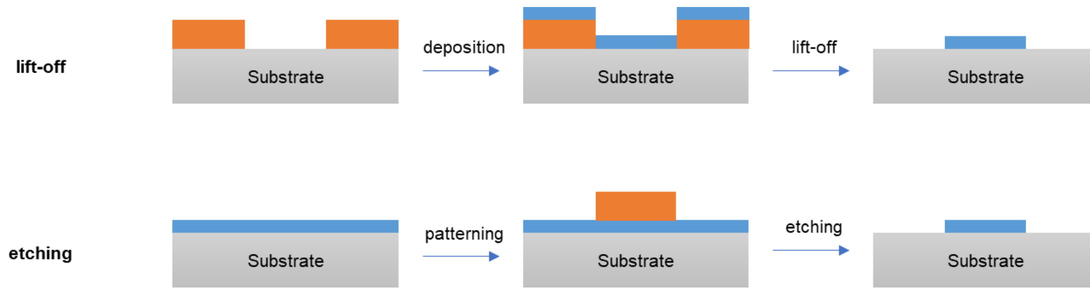

Figure 3.3. Steps of pattern transfer using lift-off (top) and etching (bottom).

When very fine resolution (smaller than 2 μm) is needed, electron beam lithography was used in the thesis. Electron beam lithography works by using a focused electron beam to selectively expose resist materials. The writing is carried out by steering the electron beam using an electric field and scanning the pattern. Similar to photolithography, the exposed area either becomes more soluble or less soluble depending on the polarity of the resist, and a developing solution will selectively dissolve the unwanted area, leaving resist with the desired pattern. Due to the small wavelength of the electron beam, electron beam lithography offers much finer resolution, down to ~10 nm, but the process is a serial process and therefore takes longer time than photolithography using a mask when the exposure area is large. Electron beam lithography may suffer from proximity effects due to the long scattering diameter of electrons. Proximity effect correction can be implemented to mitigate the issue. We used polymethyl methacrylate (PMMA) resist with thickness of 200 nm, and base electron dose of around 1000 μC cm^{-2}. In the thesis, electron beam lithography was primarily used to fabricate plasmonic structures for voltage controlled optical properties and was often combined with electron beam evaporation rather than sputtering for higher deposition directionality and easier lift-off.

3.2 Magneto-Optical Kerr Effect

Magneto-optical Kerr effect (MOKE) refers to the change of polarization when light is reflected off a magnetized surface, originating from the magneto-optical activity and the magnetization of the materials. Figure 3.4 shows the MOKE when a linearly polarized light is reflected by a magnetic sample, it becomes an elliptically polarized light characterized by a rotation angle and ellipticity[67,68].

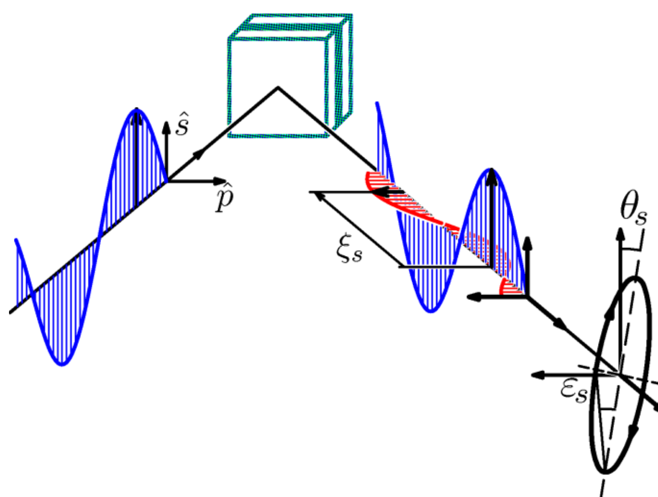

Figure 3.4. Magneto-optical Kerr effect (MOKE). Adapted from Ref.[68]

Based on this effect, MOKE polarimetry is carried out to study the magnetic properties of magnetic thin films. It allows the measurement of ultra-thin magnetic structures and gives fast measurement time scales compared to vibrating sample magnetometry, but has the disadvantage of the signal not providing quantitative information of the absolute magnetization of the samples.

Using a piezo-birefringent modulator (PEM), polarizers and a lock-in amplifier, both the ellipticity and the Kerr rotation can be measure simultaneously[69]. It is also possible to acquire polar MOKE results with only polarizers and a quarter waveplate, without the use of PEM. In the thesis, the experimental schematics are shown in Figure 3.5. A 660 nm red laser is used as the light source,

and the light is focused on the sample using an objective lens. The signal is detected by the photodiode detector. Alternatively, a white light source is used, and an CCD camera is used to image the MOKE contrast of an area. In either case, the received signal is proportional to the out-of-plane magnetization of the sample.

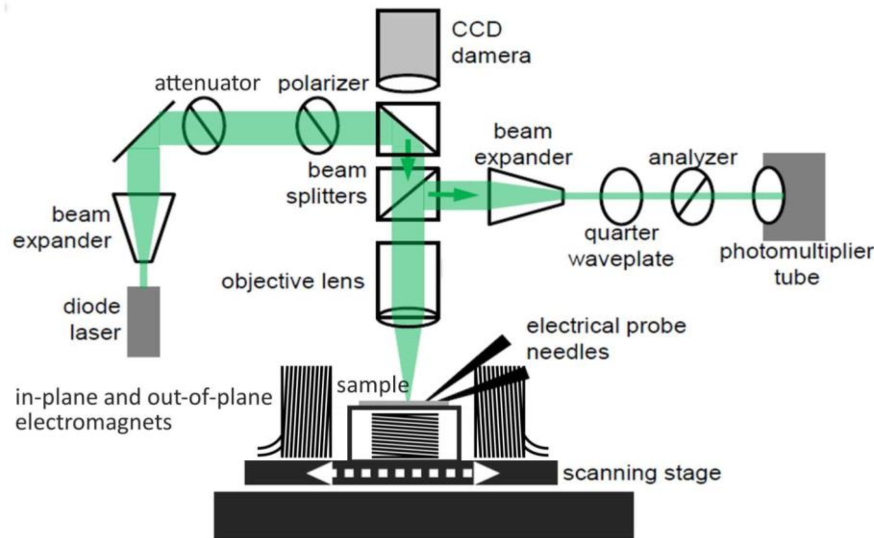

Figure 3.5. Magneto-optic Kerr effect measurement system with integrated focused laser and wide field capabilities. Adapted from Ref.[70]

Both focused laser and wide-field MOKE were used in the thesis. When a focused laser is used, the magnetic information of only one spot can be analysis at a time, but due to the fast response of the detecting diode, the method provides high bandwidth. On the other hand, when the wide-field MOKE is used, the magnetic information of an area can be acquired by the CCD so that one can get an image of the sample containing the magnetic contrast. To acquire hysteresis loops of magnetic films, the magnetic field is swept and the out-of-plane component of the magnetization of the sample is measured by the MOKE signal.

3.3 Anomalous Hall Effect

In magnetic materials, the Hall effect includes an additional contribution than the ordinary Hall effect, known as the anomalous Hall effect (AHE)[71]. It is proportional to the magnetization of the material rather than the magnetic field. In some materials, the AHE is much stronger than the ordinary Hall effect. AHE allows for the measurement of out-of-plan magnetization as shown by Figure 3.6. The anomalous Hall resistance (R_{AHE}) is the transverse voltage to the current in the longitudinal direction. R_{AHE} is proportional to the out-of-plane magnetization.

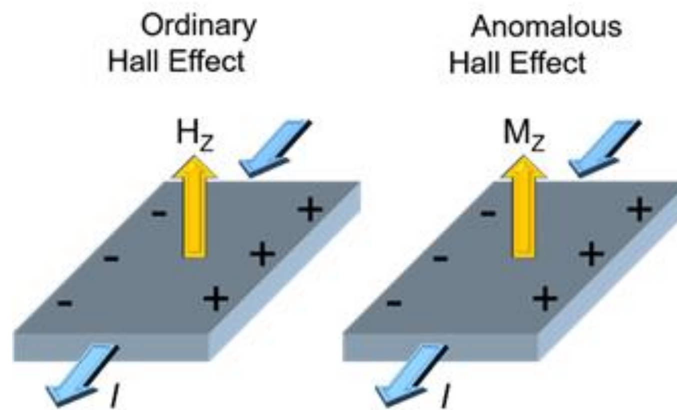

Figure 3.6. Ordinary (left) and anomalous (right) Hall effects. Blue arrows represent the direction of current, and "+" and "-" signs represent the polarity of Hall voltage. Adapted from Ref[9].

In this thesis, R_{AHE} is measured using a lock-in method, where an AC current is injected in the longitudinal direction and the AC voltage is read along the traverse direction. The AC measurement usually is more robust against noise than a DC measurement.

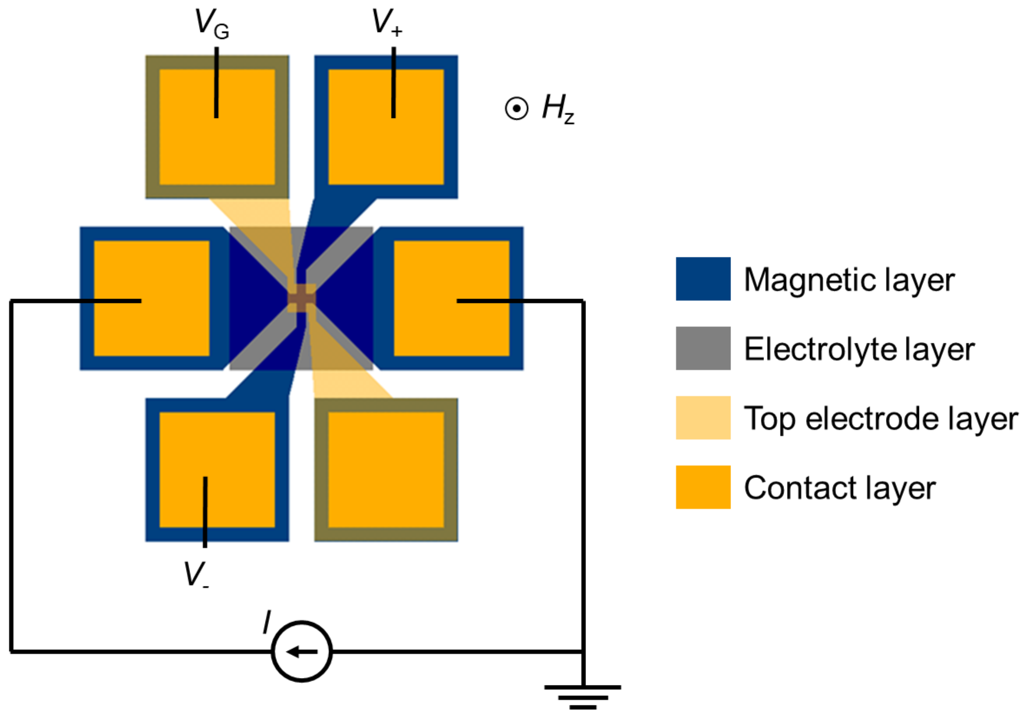

Figure 3.7. Device layout of voltage gated Hall cross for AHE measurement while a gate voltage is applied.

The anomalous Hall effect hysteresis loops are acquired by sweeping the out-of-plane field while measuring the anomalous Hall signal. In addition, since the thesis focuses on the gate voltage induced magnetic property change, gated Hall crosses were fabricated so that R_{AHE} could be measured at the same time of gate voltage application. Figure 3.7 shows the device layout of a gated Hall cross that allows for measurement of R_{AHE} while a gate voltage (V_G) is applied.

3.4 X-ray Absorption Spectroscopy (XAS) and X-ray Magnetic Circular Dichroism (XMCD)

X-ray absorption spectroscopy (XAS) and X-ray magnetic circular dichroism (XMCD) are two closely related spectroscopy techniques that are sensitive to elemental chemical and local

magnetization[72–74]. XAS was carried out to study the chemical change induced with gate voltage applied. XMCD was used to study the sublattice moment change of the GdCo ferrimagnets.

In XAS, the absorption of incident X-ray by the sample is measured as a function of X-ray energies. At certain energies, a sharp rise in absorption is observed, which corresponds to a transition of an electron ground state to an empty state. The sharp rise is called the absorption edge for the corresponding transition. XAS measurements are usually performed at synchrotron facilities because the measurement requires an intensive continuous energy-spectrum. The incoming photon energy is tuned using a monochromator. There are a few different methods to collect the absorption spectra including transmission, fluorescence, and electron yield[75]. Transmission is very straight forward, where the transmitted beam intensity is measured as a function of photon energy to get the absorption. The technique gives proportional information but requires a thin substrate (usually a membrane) for the X-ray to transmit through the sample. Fluorescence is to measure the X-ray fluorescence when a sample is illuminated with X-ray photons. The detector may also distinguish the energy of the received fluorescence photons giving more information about the sample. In electron yield mode, the absorption is measured by the photoelectrons created by the X-ray absorption. The sampling depth of electron yield is limited because photoelectron needs to be able to escape from the surface, leaving only less than a few nanometers of sampling depth[76]. Based on the energy and intensity of the measured peaks in XAS results, the valance and chemical environment of specific element can be characterized.

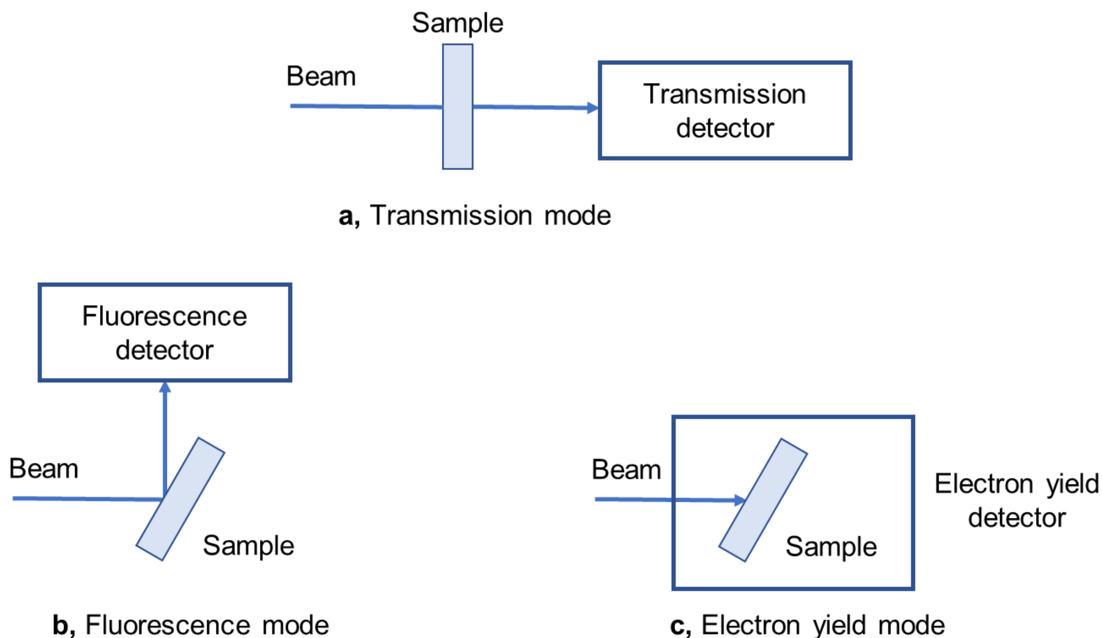

Figure 3.8. Schematic of experimental setups for different XAS detection modes. a, Transmission mode. **b,** Florescence mode. **c,** Electron yield mode.

For example, Figure 3.9 shows the XAS spectrum of Mg element at L_2 edge of Mg-Ni alloy before and after loading with hydrogen, revealing an emergence of a shoulder at around 1310 eV. The difference can be used to identify the chemical change of our thin film structure after a gate voltage is applied.

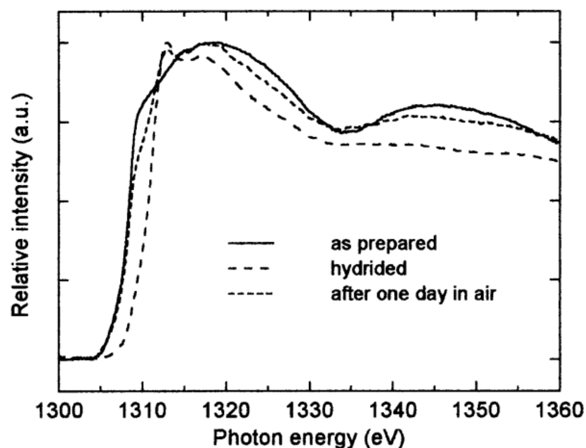

Figure 3.9. X-ray absorption spectra of Mg-Ni at Mg K-edge before and after hydrogen absorption and after exposure to air. Reprinted with permission from Ref.[77]

XMCD measures the difference between XAS spectra acquired with two opposite circular polarization vectors. The XMCD spectra can be modeled using the sum rule to retrieve the spin, and angular momentum of individual elements[78]. The XAS data in this thesis were collected using fluorescence signals at the CSX and IOS beamlines of the National Synchrotron Light Source II (NSLS-II) at Brookhaven National Laboratory. The XMCD data were collected at BL29-BOREAS beamline in transmission mode at ALBA managed by Construction, Equipping and Exploitation of the Synchrotron Light Source (CELLS).

Chapter 4
Voltage Control of Resistivity Based on Metal/Metal Oxide Redox Reactions

Neuromorphic electronics based on artificial synapses can enable non-von-Neumann computing architectures that are highly-parallelized and energy efficient[79–81]. In such systems, the signals transmitted between neurons are represented by currents, the weights of synaptic connections are represented by electric conductance, and the learning function can be achieved by tuning the conductance according to synaptic modification rules[82]. Two-terminal memristive devices can serve as synapses for brain-inspired computing systems,[79,83–85] but require temporal separation of the learning and signal transmission functions that occur concurrently in natural neural systems[86]. Three terminal resistive switching devices in which a gate controls the channel conductance can more efficiently reproduce synaptic behaviors[87].

Three terminal resistive switches can also enable multilevel data storage. Multilevel data storage can be achieved with two-terminal resistive memory devices, but the resistance state can be perturbed during the read operation[88]. Since three-terminal resistive switches have separate read and write paths they can offer improved multilevel memory stability. A variety of three terminal resistive switches have been proposed. A three-terminal chemical resistive switch was first proposed in 1960 and termed memistor,[89] but the reliance on a liquid electrolyte limited its applicability. Solid-state memistors were later developed based on WO_3 thin films,[90] and though

high resistance change ratios could be achieved, it required operating voltages in the range 10-30V. Atomic switches have been studied for three-terminal resistive switching devices, but the fabrication is relatively complicated[91]. Ferroelectric field effect transistors are promising for three terminal resistive switching as they provide fast switching speed and high resistance change ratio, but they are usually limited by the retention time[92]. New types of three-terminal switches based on alternative switching mechanisms could lead to enhanced performance and broader application possibilities.

In this chapter we study a three-terminal resistive switch based on solid-state redox reactions between metal and metal oxide. Because of the large resistivity difference between the metal and its oxide, redox reactions can be used to substantially modulate the resistivity of the material. Bauer et al. demonstrated that by applying a voltage to a Co/GdO_x/Au thin-film stack, oxygen ions in the GdO_x layer can be driven towards or away from the Co layer to oxidize or reduce it, and thereby control the magnetic properties of the Co[6]. Bauer also proposed and experimentally realized a three-terminal device[5] that exploited this same phenomenon to induce nonvolatile changes of the resistance of a metal channel, though the changes were relatively modest due to a thick metal back electrode that acted as a current shunt. Here we use the same material system and a three-terminal configuration but with a more suitable layer structure to demonstrate large lateral resistance (R_L) modulation using a small gate voltage V_g applied to the top electrode. Recently, a lateral resistance change was observed in gated metal/GdO_x/gate structure, but the effect was slow (on the order of minutes) even at elevated temperatures[93]. Here we show that fast resistance switching at room temperature can be obtained, and provide additional insight into the mechanism and design of such devices. By measuring the resistance change rate at different temperatures, the thermally activated nature of the resistance change is observed. We demonstrate reversible resistive switching at room

temperature with a ratio of ~10^3. Potential material choices and device designs are discussed for achieving better switching performance. The resistive switch demonstrated here has potential applications for neuromorphic computing and multilevel data storage and, due to the stability and low resistivity of the metal channel, it also has the potential of controlling a relatively large current.

4.1 Experimental Methods

Sample preparation: All devices were prepared using magnetron sputtering through shadow masks on thermally oxidized Si at room temperature with a background pressure of ~3×10^{-7} Torr. The Ta (2 nm) layer for contact pads was deposited under 2 mTorr Ar. The Co (5 nm) layer, Au (5 nm) layer for contact pads, and top electrode layers were deposited under 3 mTorr Ar. The GdO_x layers were deposited by reactive sputtering from a Gd target under 3 mTorr Ar at an oxygen partial pressure of ~5×10^{-5} Torr.

Electrical Measurement: The Co channel resistance R_L was measured using a Keithley 2400 sourcemeter by sourcing a 0.05 V voltage. Microprobes were used to make electrical contact, and the contact resistance was measured to be smaller than 20 Ω. V_G was applied using one of the wire terminals as ground. The top electrode was switched to open loop when the voltage pulses were off (shown as 0 V).

4.2 Voltage Induced Resistive Switching

Figure 4.1 (a) illustrates the operation of a resistive switch consisting of a Co channel, a GdO_x gate oxide that acts as a solid-state ionic conductor[6], and a Au gate electrode. When $V_G < 0$ V is applied

to the gate electrode, oxygen ions are pumped towards the cobalt channel forming insulating cobalt oxide. When $V_G > 0$ V is applied, oxygen is driven away from the cobalt layer and the cobalt oxide is reduced. V_G can hence control the thickness of the cobalt metal layer and therefore the lateral resistance of the channel.

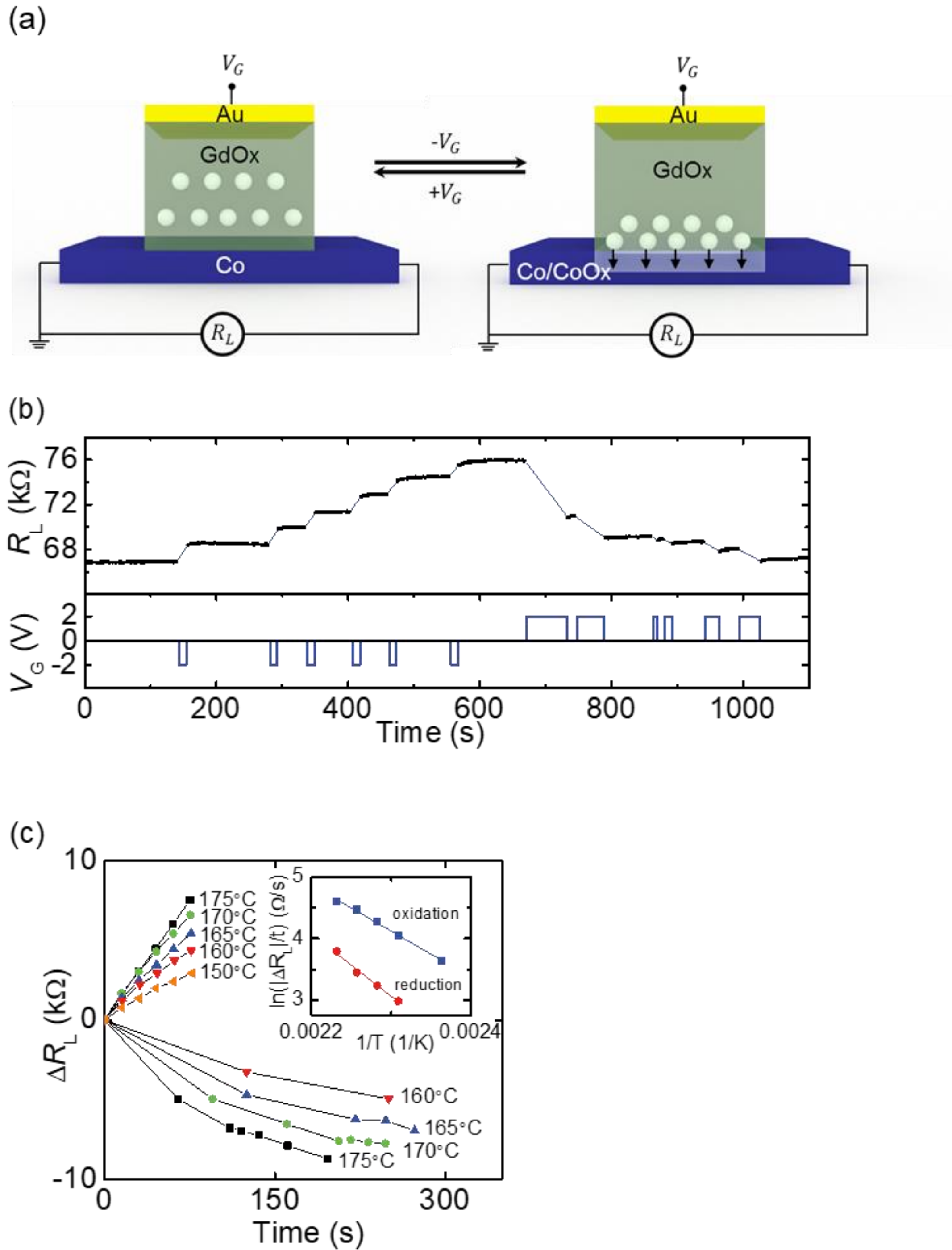

Figure 4.1. Voltage induced resistive switching. a, Schematic illustration of the operation principle of the three-terminal resistive switch. Oxygen ions in the GdO_x layer are shown as white spheres. **b,** R_L and V_G as a function of time at 175 °C. **c,** Resistance change as a function of the duration of -2 V gate voltage (above x-axis) and of +2 V gate voltage (below x-axis). Inset: Plot of logarithm of resistance change rate versus inverse temperature under -2 V gate voltage (blue) and under +2 V gate voltage (red) with linear fittings.

Two sets of devices were fabricated with different lateral dimensions and gate oxide thickness, labeled as (I) and (II) below. Structure (I) is composed of a 200 μm wide Co(5 nm) wire, Ta(2 nm)/Au(5 nm) pads for making electrical contact, a GdO_x(80 nm) layer covering the whole cobalt wire, and a 2.6 mm wide Ta(1.4 nm)/Au(5 nm) top electrode. Structure (II) is composed of a 200 μm wide Co(5 nm) wire, Ta(2 nm)/Au(5 nm) contact pads, a GdO_x(10 nm) layer covering the whole cobalt wire, and a 200 μm wide Au(3 nm) top electrode.

We first studied resistance switching of devices (I) at elevated temperatures to enhance the oxygen vacancy mobility[6]. The device was first heated up to 200 °C and after the channel resistance stabilized ,the device was cooled and maintained at 175 °C. +2 V and -2 V voltage pulses were applied to the top electrode and R_L was monitored between pulses. Figure 4.1(b) shows R_L and V_G versus time. R_L increased (decreased) as negative (positive) V_G was applied. The direction of resistance change was consistent with the cobalt redox mechanism. The device behaves as a non-volatile multilevel memory because the resistance change ΔR_L scales with the voltage pulse length, and at $V_G = 0$, the resistance is stable.

The temperature dependence of the resistance switching of (I) devices was investigated as follows. The channel resistance was set to a value $R_0 \approx 68000\ \Omega$. First at 175 °C, R_L was measured between five -2 V 15 s gate voltage pulses and then the resistance was reduced by applying +2 V pulses to a value slightly below R_0. Repeating these procedures, the resistance increase due to negative V_G pulses was measured at 175 °C, 170 °C, 165 °C, 160 °C and 150 °C and the resistance decrease due to positive V_G pulses was measured at 175 °C, 170 °C, 165 °C, and 160 °C. Figure. 4.1(c) shows ΔR_L as a function of the integrated voltage pulse time. Resistance change rates were then calculated as the average resistance change over time. The inset shows the logarithm of resistance

change rate versus inverse temperature when -2 V was applied (blue) and when +2 V was applied (red). The data show a thermally activated Arrhenius-like behavior with an effective activation energy of 0.59±0.02 eV for oxidation and 0.80±0.08 eV for reduction. The reduction is slower and has a higher activation energy than oxidation, which we attribute to the reduction potential of the Co layer, which should act as a built-in potential that biases oxygen ion migration towards the metallic Co layer.

4.3 Modeling Oxidation Progress

In reducing the GdO_x thickness from 80 nm to 10 nm, we find the resistance switching behavior of devices (II) can be observed on similar or faster time scales as devices (I) even at room temperature. We attribute this behavior to the larger electric field and ion migration rate in the thinner GdO_x, which was also reported in Ref. [6]. Figure 4.2(a) shows the resistance response of a +3 V gate voltage pulse right after a -2 V voltage pulse at room temperature. The resistance increased as V_G = -2 V gate voltage was applied, and decreased as V_G = +3 V gate voltage was applied, and stayed stable after the cycle. The kinetics of oxidation under a negative gate voltage was found to fit well to a logarithm oxidation rate law. The cobalt oxide layer was assumed to be uniform in thickness under the top electrode, and the conduction through the cobalt oxide layer to be negligible compared to the cobalt layer. The total cobalt layer thickness, if all cobalt exist in metallic form, is denoted as h_{total}, and the thickness of cobalt that is oxidized is denoted as h_{CoOx}. The resistance of the wire is the sum of two components, which are R_{active} and $R_{passive}$. R_{active} is the resistance of the active region under the top electrode and $R_{passive}$ is the resistance of the wire outside the gate plus the resistance from electrical contact. Therefore the lateral resistance of

the wire $R_L = R_{active} + R_{passive}$, and $R_{active} = \rho_{Co} \frac{l}{(h_{total} - h_{CoOx})w}$, where ρ_{Co} is the resistivity of cobalt thin film, l is the length of the wire under the gate, and w is the width of the wire. The logarithm oxidation rate law is described by:

$$h_{CoO_x} = K \ln(\alpha t + 1) + X_0 \tag{4.1}$$

where K, α and X_0 are constants, and t is the time from the oxidation begins. The rate equation gives

$$R_L = R_{passive} + \frac{\rho_{Co} l}{w(\mathrm{C} - K \ln(\alpha t + 1))} \tag{4.2}$$

where C is a constant. The green curve in Figure 4.2(a) shows the fitting Eq. (2) to the data. A similar logarithm oxidation rate law was observed for metal with a thin oxide layer exposed in air at low temperatures[94–96]. The diminishing rate at longer time indicates that the cobalt oxide formed during the oxidation is probably limiting the switching speed for these devices. This implies that a thinner cobalt layer may lead to faster resistance switching. The positive voltage pulse has a larger amplitude than the negative voltage pulse, but the reduction process takes longer than the oxidation, which is consistent with the observations of (I) devices.

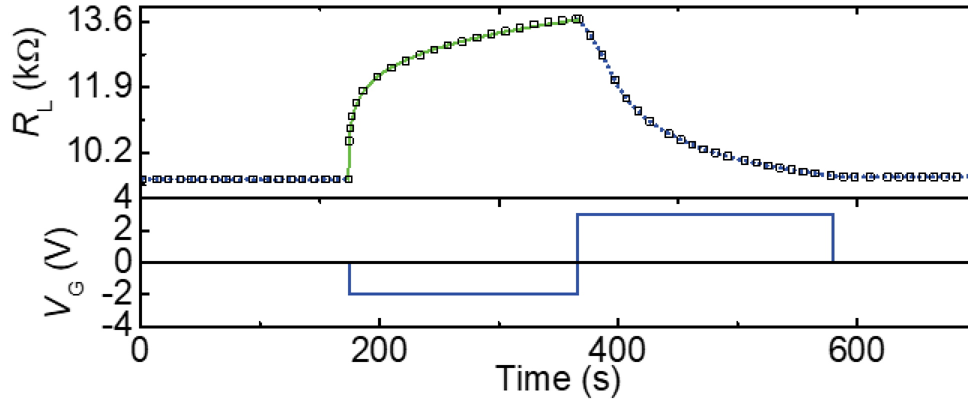

Figure 4.2. R_L and V_G as a function of time at room temperature. -2V and +3V pulses were applied in sequence. R_L measurements are shown as black squares. The blue dotted lines are for guiding the eyes. The green line is R_L fitted using logarithm rate law.

Because a reversible high resistance change ratio is desirable for many applications, attempts were made to increase the wire resistance to a very high value and then switch it back. We found that when the R_L increase is too high (MΩ range), positive V_G can no longer reduce R_L, which is probably due to loss of electrical connection to the portion of the channel under the gate, which serves as counterelectrode. In order to gain more insight into the phenomena, we measured the temperature-dependence of R_L as the device goes through oxidation and reduction. First by applying V_G = -3 V, R_L was increased to ~100 kΩ. Then by applying a V_G = +3 V, R_L was reduced to ~19 kΩ. Figure 4.3(a) shows resistance versus temperature for both states. At the high resistance state, R_L decreases as the temperature increases, which indicates semiconducting nature of conduction. At the low resistance state, R_L increases with increasing temperature, indicating metallic conduction.

4.4 Large Voltage Induced Resistance Switching

The change in the character of conduction in the Co channel in the high-resistance state, and our observation that after setting the device to even higher R_L a gate voltage can no longer decrease it, is explained schematically in Figure 4.3(b). Initially, the cobalt layer is continuous and metallic with small variation of thickness in the lateral plane, as illustrated in Figure 4.3(b) (i). When $V_G < 0$ V is applied, oxygen ions are driven towards the cobalt layer. The grain boundaries of cobalt are likely to be the fast diffusion paths for oxygen ions and therefore oxidation is likely faster along them. The non-uniformity may get enhanced as the oxidation goes on, as illustrated in Figure 4.3(b) (i-ii). When the oxidation time is long enough, islands of metallic cobalt remain while insulating oxide gaps form between the metallic islands as shown in Figure 4.3(b) (iii). The conduction of the wire changes from metallic to semiconducting as it is limited by the oxide gaps. As the oxidation goes on, the metallic islands eventually become separated and the electrical connection to the portion of the channel under the gate is lost. As a result, a positive voltage can no longer reduce the wire back to the original state.

Instead of using dc negative and positive voltage to control the wire resistance, we found that by applying negative voltage and an alternating waveform to the top electrode, a reversible resistance change by a factor of 10^3 could be achieved. Here, a set of devices similar to (II) but with slightly thinner Co (4 nm) was fabricated. By applying a gate voltage of -3 V, the channel resistance could be increased from ~100 kΩ to 10^8 Ω, but positive dc bias can no longer reduce the resistance. The current-voltage (I-V) characteristics of the Co channel at both a low and a high resistance state are shown in Figures 4.4 (a),(b) respectively. At the low resistance state, the I-V curve shows a linear ohmic behavior, while at the high resistance state, a rectifying and hysteretic I-V curve was

observed. The shapes of the I-V curves are consistent with the illustrations shown in Figure 4.3(b) and the temperature-dependent channel resistance in Figure 4.3(a): in the low resistance state, the continuous metallic cobalt layer gives an ohmic I-V behavior, whereas in the high resistance state, and the insulating gaps between metallic islands give raise to a rectifying I-V curve.

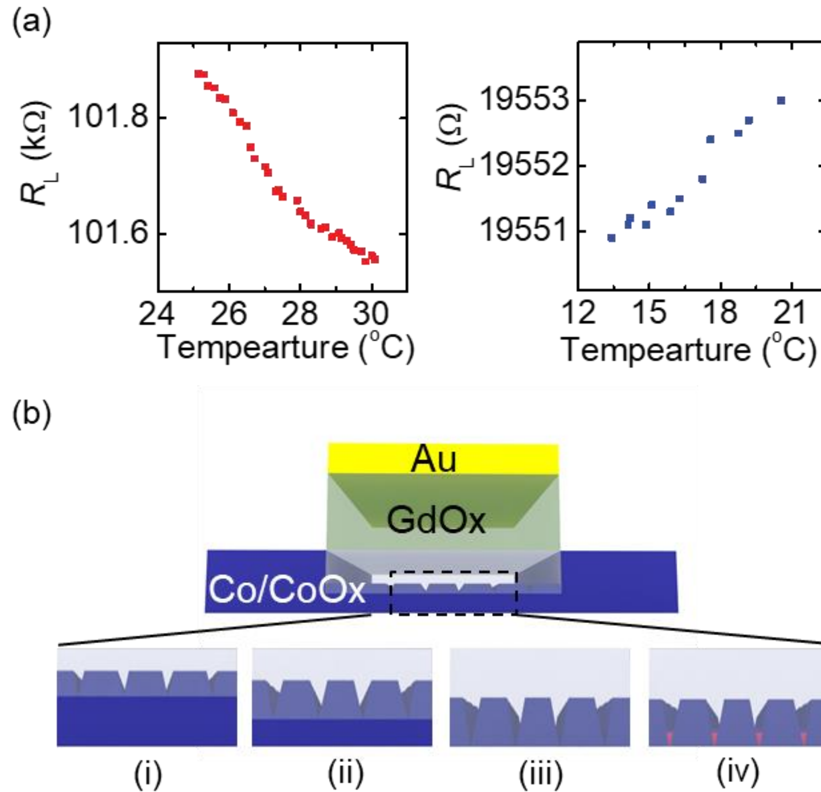

Figure 4.3. Possible morphology evolution during V_G application. a, *R*-*T* curves of the wire at high resistance state (~100 kΩ) and at low resistance state (~19 kΩ) **b, i-iii** Schematic illustrations of the possible morphology evolution as the metal is oxidized. **iv** Schematic illustration of the possible mechanism responsible for the fast resistance decrease after applying the +4 V/-1 V waveform.

As is known in two-terminal oxide memristive devices, voltage cycling can create conductive filaments or induce charge carrier redistribution across an insulating barrier[97,98]. We employed a similar strategy to recover electrical contact within the bottom electrode in the high resistance state

and to therefore allow recovery of the low-resistance state by gate voltage. Here, instead of applying a dc gate voltage, we applied an alternating +4 V/-1 V waveform to the Au gate electrode, which allowed for successful recovery of the low-resistance state reliably over many cycles (Figure 4.4(c)). The waveform has a periodicity of 100 ms, with 95 ms square pulses at +4 V and 5 ms square pulses at -1 V, as shown in Figure 4.4(c), inset. Using this protocol, we can reliably toggle the channel resistance by a factor of ~10^3 times by applying -2 V voltage and the same +4/-1 V waveform, with a switching time less than 30 s. We therefore explain the fast reversible switching as follows. When a negative voltage is applied to the top electrode to oxidize the wire, the electrical connection to the portion of wire under the gate is becoming limited by the insulating gaps between metallic islands as shown in Figure 4.3(b) (iii). A positive constant voltage is slow to close the gaps by reduction of the oxide because the process requires formation of electrical connections in the lateral direction. While a -1 V transient pulse may change the defect concentrations inside the gaps and create conductive paths deep in the gaps, which are illustrated as a red layer in Figure 4.3(b) (iv). If the negative voltage pulse is followed by a positive voltage pulse, the reduction of oxide can proceed quickly with the help of the conductive paths formed by the negative voltage, and therefore the fast reversible resistance switching with high resistance change ratio can be obtained.

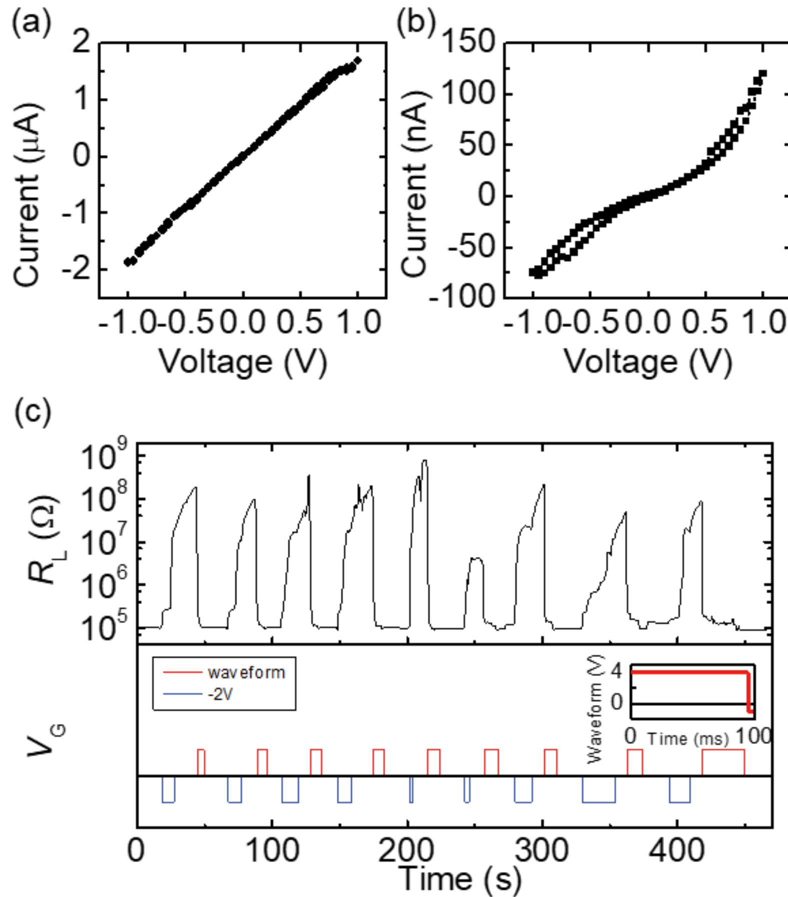

Figure 4.4. Large Voltage Induced Resistance Switching. **a,** I-V curve of the wire at around 500 kΩ. **b,** I-V curve of the wire at around 20 MΩ. **c,** Wire resistance change and gate voltage as a function of time demonstrating fast reversible resistance switching at room temperature. Inset: +4 V/-1 V waveform used for switching.

4.5 Material Selections and Device Designs for Better Switching Performance

Here we describe several strategies for the proposed devices to achieve better switching performance. We described a new type of three terminal resistive switching device focusing on demonstrating the working principle and preliminary results. The results show promises for applications such as neuromorphic computing and electric switch involving controlling a large

current. For these potential applications, a large switching ratio and fast switching speed are desired. The section will first discuss the selection criteria for the materials for the conductive channel and resistive switching mechanism that can be used to achieve improved performance. The section will then describe an alternative device design to mitigate the problem of losing electrical connections to the bottom electrode when the conductive channel becomes highly resistive. Successfully addressing the problem has the potential to increase the reversible switching ratio significantly.

Other resistance switching materials than Co may be applied to improve the performance of the device. Tan et al. showed that the same device structure allows reversible hydrogen loading into the bottom layer, we propose that a range of materials that change their resistivity with hydrogen loading can be used as the conductive channel material[7]. The alternative approach has the advantage of faster ion migration and better reversibility. For this approach, the selection criteria for getting better device performance is that the material of interest should have a large resistance difference between hydrogen loaded state and hydrogen unloaded state and should have high hydrogen diffusivity in both states. We expect that Mg-Ni alloys and VO_x are promising candidates: Mg is a metallic conductor, while the electronic structure of MgH_2 formed by hydrogenation of Mg is non-metallic with a large band gap of ~4-5 eV[99]. The switching speed of Mg could potentially be improved by alloying. For example, Mg-Ni alloys potentially offer faster loading and unloading speed than Mg as shown in Figure 4.5a. Another type of materials that has the potential to be used for the voltage switchable conductive channel is VO_2 as recently result has shown reversible transition between a metallic phase to an insulating phase with hydrogenation. The sheet resistance changed ~5 orders of magnitude as shown in Figure 4.5b.

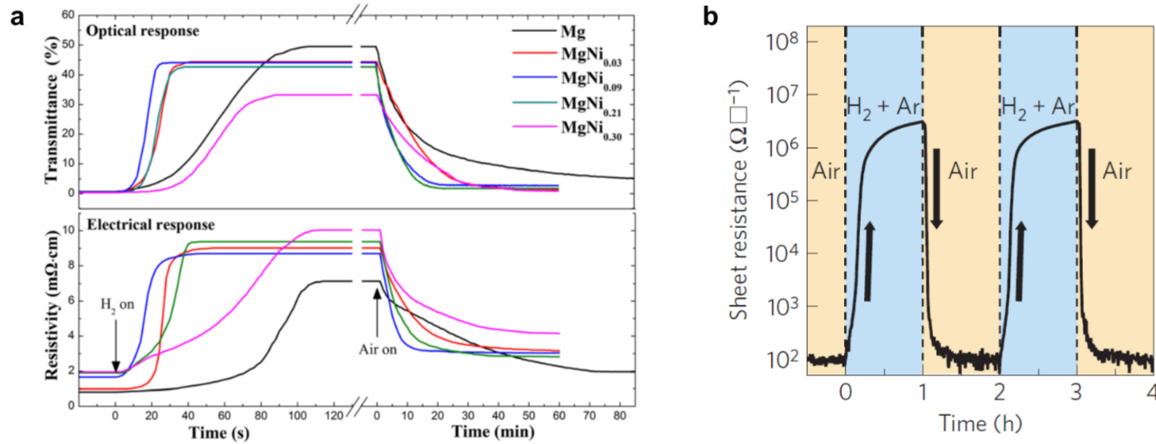

Figure 4.5. Dynamic resistivity modulation of $MgNi_x$ and VO_2. a, The optical and electrical responses of Mg and $MgNi_x$ (x = 0.03–0.30) films. **b**, *In situ* resistivity of $(100)_R$-VO_2 films on (0001) Al_2O_3 during hydrogenation and dehydrogenation as a function of time at 120 °C showing resistivity change ratio of ~10^5. Reprinted with permission from Refs. [100,101].

As discussed above, when R_L increases and becomes comparable to the resistance of the gate, then the gate voltage cannot be effectively applied across the device stack as the lateral resistance will contribute a large voltage drop. This voltage drop prevents the device from achieving a reliable and reversible switching with large switching ratio. The method of alternating gate voltage discussed in Section 4.4 increases the range of resistance switching, but the switching still lacks reliability. Here we propose that an inclusion of an additional layer under the conductive channel material to mitigate the problem. The additional layer provides stable electrical contact to the bottom electrode regardless of the chemical state of the conductive channel material. The additional layer should have lateral resistance that is lower than that of the gate resistance (on the order of MΩ to GΩ). However, the lateral resistance should not be too low so that the conductive channel is shunted. In addition, the layer should be chemically stable or have much lower reaction kinetics than the switchable material. We propose the use of amorphous graphite or doped silicon. When a 5 nm of amorphous graphite or silicon doped at a concentration of ~10^{17}/cm^3 is used, the lateral resistivity of the device will be on the order of 10^7 Ω. If Co is used as the channel material,

a switching ratio of 10^4 - 10^5 should be achieved reliably. The gate oxide resistance can be potentially higher if the deposition is optimized, so that even higher switching ratio can potentially be achieved.

4.6 Summary

In summary, we demonstrated a three-terminal resistive switch based on a metal-redox switch. The device operates by oxidizing a metallic material and reducing the corresponding oxide back to metal with all solid-state operation. The resistance switching was observed to be a thermally activated process. For devices with a thinner GdO_x layer, resistance change can be observed at room temperature. By reducing the thickness of the wire layer, a switching ratio of $\sim 10^3$ was obtained. In nanoionics devices, switching speed on the order of nanosecond has been demonstrated[102]. Further performance improvement can be expected by reducing the size of the device, by optimizing the thickness of the wire and oxide, by replacing GdO_x with better oxygen ion conductor materials, and by optimizing the metal channel material and microstructure. The reversible non-volatile redox reaction between metal and metal oxide provides a way of post-fabrication control of solid-state material composition and properties. This type of three-terminal switch may find applications in neuromorphic computing and multilevel data storage, as well as applications that require a large resistivity change and those involving controlling a relatively large current.

Chapter 5
Voltage-Gated Optics and Plasmonics Enabled by Solid-State Proton Pumping

Dynamic control of optical properties by hydrogen absorption/desorption has been actively pursued since the discovery that thin metal films can be reversibly transformed into an optically transparent state by hydrogenation[43]. Following the initial work on yttrium, hydrogen-switched optics, such as mirrors[43,44] or other reflection-based optical devices[45,46], were realized with a wide range of materials including Pd and Mg[47,48]. Metals such as Mg are of particular interest as they can support plasmon resonances in the visible spectrum in nanostructures with suitable geometry[48]. These resonances can enable subwavelength light manipulation, and color generation with print resolutions at the optical diffraction limit[30,31,49]. Hydrogen loading and unloading can serve as an effective means to change the optical response on demand to achieve active plasmonics and metasurfaces, with great potential in dynamic plasmonic color displays, dynamic holography, anti-counterfeiting technologies, and information encryption[46,50–53]. However, in most work so far, plasmonic switching is achieved through exposure to hydrogen gas in an enclosed chamber, which is impractical for many applications as it precludes addressability, i.e. local and selective switching[54]. Although hydrogen gating using ion storage layers has been achieved in solid-state tunable mirrors[103] and similar electrochromic devices[104], a simple, general means to locally gate hydrogenation in more complex optical and plasmonic device architectures is currently lacking.

It was recently demonstrated that a solid-state proton pump can be realized utilizing H_2O hydrolysis in ambient atmosphere catalyzed by a GdO_x/Au interface, where it was shown that the magnetic properties of thin buried metal layers could be gated nondestructively with a modest voltage[7]. Here we show that a similar mechanism enables local, reversible hydrogen gating of optical properties in a wide range of metallic and plasmonic devices by covering the structure with a transparent gate oxide capped with a top electrode and applying a small voltage. We demonstrate the simplicity and utility of the mechanism by realizing nonvolatile voltage-gated color pixels based on tunable interference cells and plasmonic arrays. We further discover a large reversible change in the optical path length of GdO_x upon hydrogen insertion, equivalent to a > 20% change in its index of refraction, which is matched only by liquid crystal cells and complex phase-change materials[32,41,42]. Our approach permits switching speeds on the order of tens of ms, and device thicknesses down to several tens of nm. It promises highly localized control of a wide range of optical properties for applications such as high-resolution reflective displays, hyperspectral imaging, and dynamic holography.

5.1 Experiment Methods

Device fabrication: Thin film stacks were grown using magnetron sputtering at room temperature with a background pressure of ~3 x 10^{-7} Torr. Ta was deposited under 2 mTorr Ar. Au, Pt and Pd were deposited under 3.5 mTorr Ar. Al, Mg, Ti and Y were deposited under 3 mTorr Ar. SiO_2 layers were deposited by radio frequency (RF) sputtering under 3 mTorr Ar. GdO_x were deposited by RF sputtering from a Gd_2O_3 target under 3 mTorr Ar at an oxygen partial pressure of 0.6 mTorr. The transmission switching devices and interference devices were patterned with shadow masks as shown in Figure 5.1. Aluminum nanodisks of the plasmonic devices were patterned with 200 nm PMMA and electron beam lithography. 25 nm of Al was deposited by electron beam evaporation, and excess material was removed by lift-off in N-Methyl-2-pyrrolidone.

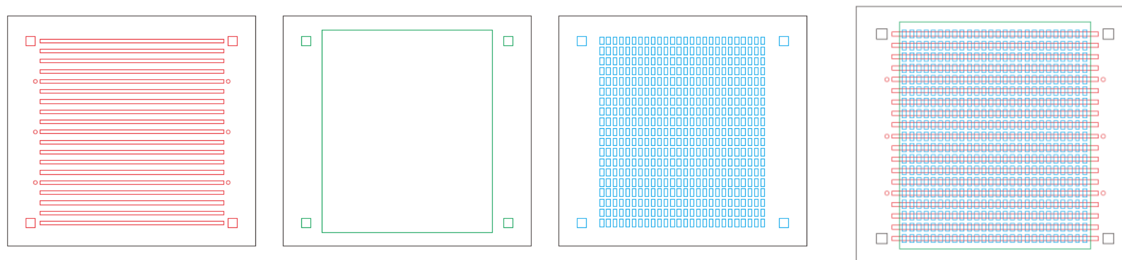

Figure 5.1. Shadow mask design for fabricating array of gating devices allowing measurement of multiple devices on thickness wedge samples. From left to right: bottom electrode layer, electrolyte layer, top electrode layer and an overlay of all layers. The width of each bottom electrode and each top electrode is 400 µm.

Gate voltage application: Gate voltages were applied using a Keithley 2400 Sourcemeter and mechanically compliant BeCu microprobes. All gating experiments were carried out under room temperature.

Gas ambient study: Four devices with the same device structure fabricated in the same batch were used in the study. The optical images of the devices in the virgin state were taken. Then the

devices were placed in a vacuum chamber. After the vacuum level reached 10^{-3} Torr, either dry nitrogen, dry oxygen, or wet nitrogen was introduced to the chamber for each device. After the pressure level reached 20 Torr, V_G = +3 V was applied to each device for 180 s, and then the devices were left open circuit. The same +3 V, 180 s was also applied to one device at vacuum without introducing gas into the chamber. Optical transmission images of these devices were taken again after the voltage applications.

X-Ray Absorption Spectroscopy (XAS): XAS data were acquired at the Coherent Soft X-ray Scattering (CSX) beamline at the National Synchrotron Light Source II, Brookhaven National Laboratory using fluorescent yield. The incident soft X-ray beam has a footprint of ~200 µm and the sample was tilted 15º relative to the incident beam. The sample used for the measurement had a crossbar geometry with about 1 mm x 1 mm gated regions and a layer structure of Ti(3 nm)/Mg(40 nm)/Pd(5 nm)/GdO_x (40 nm) with a 3 nm Au top gate. The main chamber base pressure was ~2 x 10^{-9} Torr, and the sample was kept at 150 K throughout the measurement. The gating was carried out ex-situ before loading into the measurement chamber. Three devices with the same structure, grown side by side, were used. To get the spectrum of the virgin state, no voltage application was carried out on the first device. To study the effect of positive V_G, V_G = +3 V was applied for 5 min on the second device. To study the reversibility of the chemical change, V_G = -2 V was applied for 1hr after V_G = +3 V was applied for 5 min on the third device. A large color change of the devices was observed when V_G = +3 V was applied on both the second and the third device, indicating hydrogen was loaded into the third sample before the negative voltage application (hydrogen unloading).

Optical characterization: Reflection spectra were measured using a CRAIC microspectrometer with a 20x objective and 0.5 N.A. for wavelengths between 400 nm and 800 nm. The measurements were calibrated with a standard Si reference.

Switching ratio characterization: V_G = +6 V was first applied for 30 s to each device to load hydrogen, and then the device was left open circuit for 30 s while the reflection spectrum was collected. After 30 s of open circuit, V_G = -2 V was applied for 10 s to unload hydrogen from the device. Then the device was left open circuit again and the reflection spectrum after unloading was collected. The switching ratio was calculated as the reflectance of each device after hydrogen loading over the reflectance after unloading.

Reflected color simulation: We used the transfer matrix method[19] to simulate the reflection spectra of the interference devices. The interference color change by yttrium hydrogenation was simulated assuming yttrium changed to $YH_{2.9}$, and Pd changed to PdH using the optical constants reported in ref[105] and ref[106] respectively, and assuming the refractive index of GdO_x changed from 1.7 to 2.1. The interference color by hydrogen loading into GdO_x was simulated using the GdO_x refractive index adapted from ref[107]. The reflected spectra of plasmonic devices were simulated by the FDTD method. The refractive index of MgH_2 was taken from ref[108]. Refractive indices of Ta, Ti, Au, Mg and SiO_2 from Palik[21] were used in the simulations. The colors of the devices were rendered from reflection spectra using D65 illuminant.

5.2 Optical Property Switching Using a Solid-state Proton Pump

We first show that a small gate voltage (V_G) applied to a metal/GdO_x/metal stack can be used to electrically switch optical transmission by injecting protons sourced from moisture in the air. Devices were formed by depositing a layered structure of Ti(3 nm)/Mg(60 nm)/Pd(5 nm)/GdO_x(35 nm)/Au(3 nm) onto an indium tin oxide coated glass substrate as discussed in Section 5.1, as shown schematically in Figure 5.2a. Here, Mg serves as a hydrogen-switchable mirror[38,43,109], Au serves as the top gate electrode, Pd protects the Mg from oxidation, and Ti serves as an adhesion layer. As we show below, the GdO_x layer catalyzes water splitting and facilitates proton conduction under a positive gate bias, allowing for voltage-gated switching of the transmissivity of the Mg mirror.

Figure 5.2a shows the device schematic and measurement scheme. The device was placed on a LED backlight panel and the optical images were acquired in transmission mode (Figure 5.2a, insets). Due to the low transmissivity of the 60 nm thick Mg, the sample initially appears almost opaque with a barely visible darker region corresponding to the gold contact. After $V_G = +3$ V was applied for 180 s, a large increase in optical transmittance of the gated region was observed. When the bias is removed and the device set to open circuit, the new optical state is retained in a nonvolatile fashion. After subsequently applying $V_G = -2$ V for 1 hr, the gated region of the transmitted image became dark again, showing that the optical switching behavior is reversible. This behavior is consistent with a reversible transition between metallic Mg and optically-transparent MgH_x[110], suggesting hydrogenation and dehydrogenation of Mg under gate bias. Figure 5.2b shows experiments performed under several different environmental conditions. Gating experiments were performed in vacuum, as well as at atmospheric pressure in ambient air, dry O_2, dry N_2, and wet N_2. The results indicate that the optical property changes only occur when there is moisture in the gas environment.

Figure 5.2c shows schematically the mechanism of electrochemical water splitting catalyzed at the top oxide/noble-metal interface that accounts for the reversible transition in transmittance. At positive bias, water molecules near the metal/oxide interface are split into H^+ and O_2. The gate bias then drives the extracted protons towards the bottom electrode, loading the Mg layer with hydrogen and switching it to an optically-transparent state. Under negative bias the reaction is reversed, leading to hydrogen removal and the return of Mg to a metallic state, consistent with the images in Figure 5.2a. Figure 5.2d confirms this process directly, using X-ray absorption spectroscopy (XAS) to follow the chemical state change under voltage cycling. Here, the K-edge spectra of Mg from a similar device were obtained in the virgin state, after positive V_G, and after subsequent negative V_G application, corresponding to the three optical states shown in Figure 5.2a. The XAS spectra correspond closely to previously reported K-edge XAS spectra of metallic and hydrogenated Mg, as shown in Figure 3.9[77], before and after positive bias application. The spectrum recovers to the virgin state after subsequent negative bias application, showing that the hydrogen loading process is reversible. The reverse reaction only occurs in the presence of oxygen gas as shown in previous work[7].

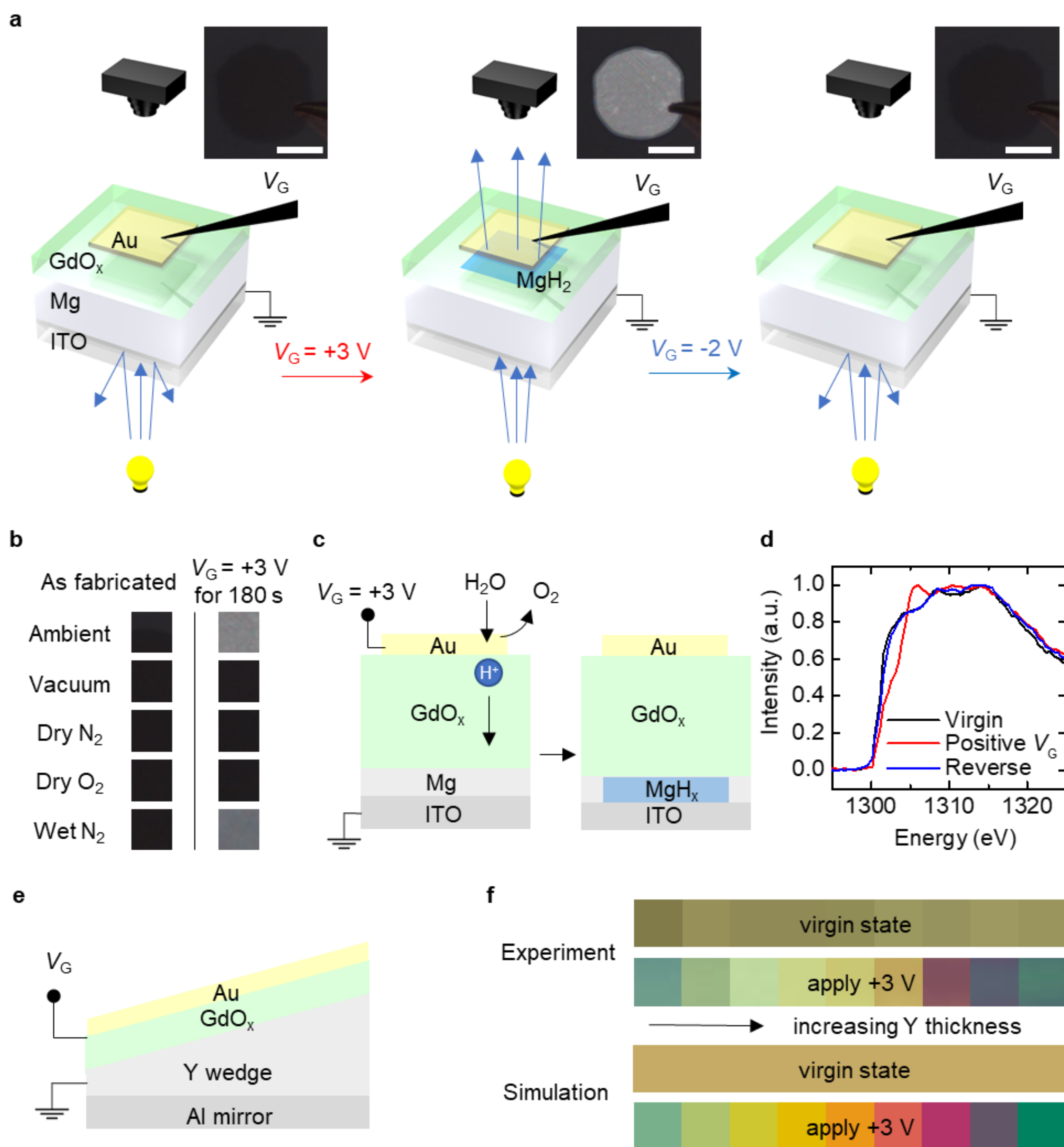

Figure 5.2. Hydrogen absorption by bottom electrode. a, Device schematic and measurement scheme for switchable transmittance devices. The Ti and Pd layers are omitted. Transmission images are shown to the right of the camera icons. The transmission image became brighter after applying V_G = +3 V and then became darker after applying -2 V. The scale bar is 400 μm. **b**, Optical images of the device as fabricated and after applying V_G = +3 V for 180 s in different gas environments (cropped to a square located at the center of the gated region). Transmission change was only observed in ambient and wet N_2. **c**, Schematic illustration of the electrochemical water splitting and Mg hydrogenation. **d**, X-ray absorption spectra of Ti/Mg/Pd/GdO_x/Au devices, in virgin state, after positive V_G application, and subsequent negative V_G application. **e**, Schematic illustration of reflection device with yttrium as bottom electrode. The Ta and Pt layers are omitted. **f**, Optical images and simulated colors of the devices with increasing yttrium thickness as fabricated and after applying V_G = +3 V for 180 s.

We next demonstrate the generality of the device design by substituting Mg with Y in a Fabry-Pérot configuration that permits the realization of nonvolatile reflective color pixels (Figure 5.2e). Here, we deposited a Ta(3 nm)/Al(100 nm)/Y(wedge 50 nm-140 nm)/Pt(3 nm)/GdO_x(35 nm)/ Au(3 nm) film on a Si substrate as described in Section 5.1. Discrete Au electrodes were fabricated across the film to allow the thickness-dependent optical properties to be probed in a single film. As fabricated, the Y layer is metallic, and devices with different yttrium thicknesses have similar reflected color as shown in Figure 5.2f. After positive bias application, devices with different Y thicknesses changed to different colors as shown in Figure 5.2f (bottom). Colors emerge as the metallic Y transforms into an optically-transparent dielectric that contributes to the total path length of the Fabry-Perot cavity. The total thickness of Y and GdO_x determines the color of the reflected light. Transfer matrix modeling of the system agrees well with experimental results, as shown in Figure 5.2f.

5.3 Switchable Plasmonic Color Devices

To demonstrate the range of functionalities that can be achieved using this simple gating mechanism, we study switchable plasmonic color devices as shown in Figure 5.3a. Starting with a uniform Al(100 nm)/Mg(40 nm)/Pd(5 nm)/GdO_x(5 nm) film, a palette consisting of pixels of Al nanodisk arrays (Figure 5.3b) was fabricated on the top as described in Section 5.1. The entire set of pixels was covered by a 35 nm GdO_x layer and a single 3 nm Au top electrode. As shown in Figure 5.3c (top), the disk diameter *d* and nearest neighbor separation *g* were varied from array to array to yield a range of reflected colors due to the geometry-dependent plasmonic resonances.

The plasmonic resonance depends on the optical properties of the surrounding layers and therefore can be controlled by hydrogen loading/unloading. As fabricated, Mg functions as a mirror layer below the Al disks. When a positive V_G is applied, hydrogen loading transforms the Mg into transparent MgH_x, so that it is no longer a mirror layer. Instead, the bottom Al layer functions as the new mirror layer. Hence, the distance between the Al disks and the mirror layer increases compared to the virgin state due to the inclusion of the MgH_x layer. The distance increase causes a blueshift of the resonances. Optical images after applying $V_G = +5$ V for 120 s are shown in Figure 5.3c (middle).

Finite-difference time-domain method (FDTD) simulations of switchable plasmonic color were carried out to simulate the reflected colors. Simulations were carried out with periodic conditions along x- and y-direction and perfect matching layers along z-direction. Planer light source and frequency domain power monitor were placed above the device. The virgin device structure used in the simulation is the same as described in the main text except that the outmost 1nm in radius and the bottom and top 3 nm of the aluminum nanodisks were replaced by aluminum oxide to account for oxidation that happened during fabrication. The Mg layer is assumed to expand in thickness by 30% when loaded with hydrogen[110]. The resulted colors as shown in Figure 5.3c (right) match well with the experimental results.

With a later negative V_G application, the colors recovered closely to the virgin state as shown in Figure 5.3c (bottom), demonstrating the reversibility of the plasmonic response control.

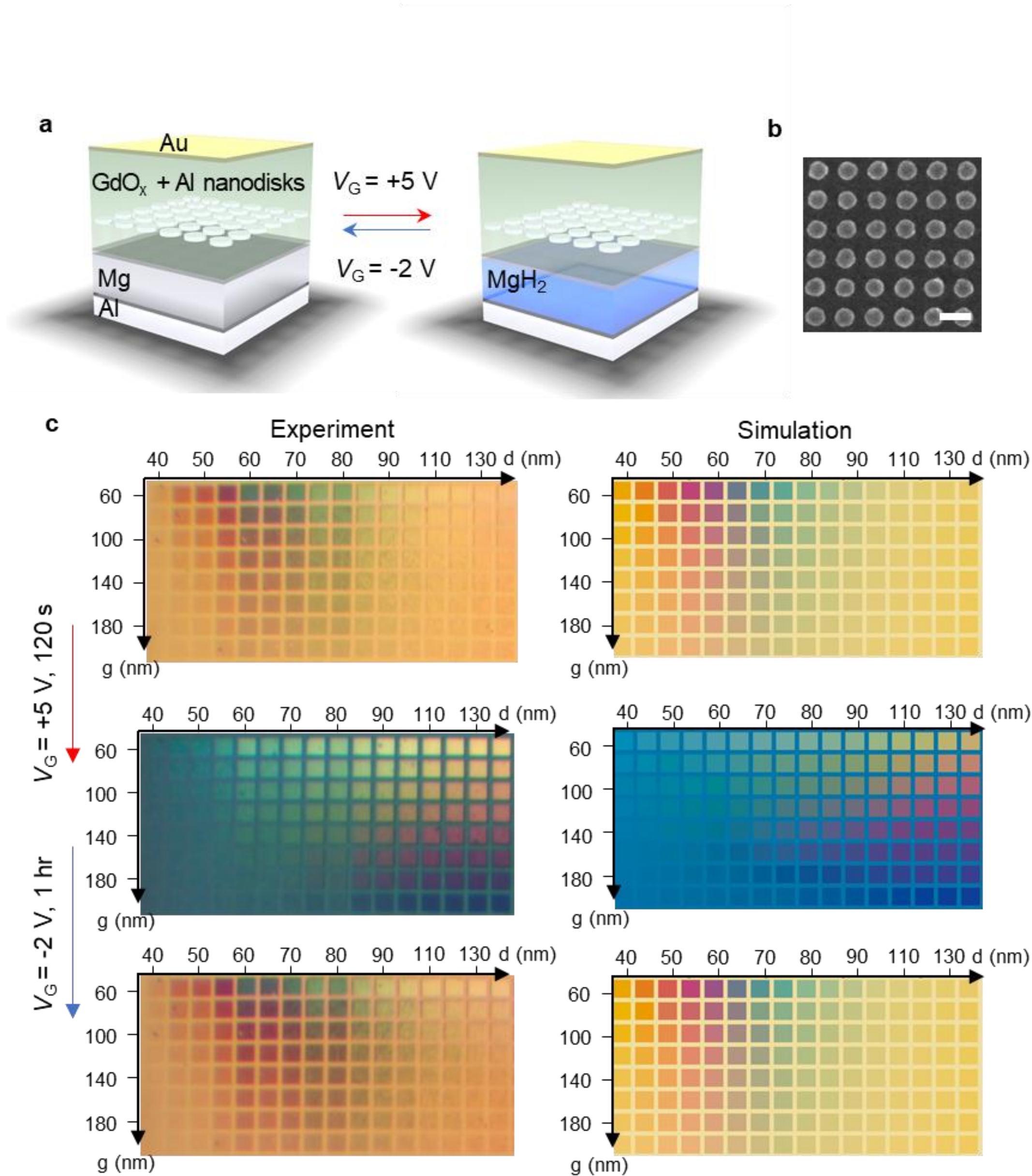

Figure 5.3. Electrochemical switchable solid state thin film plasmonic device. a, Schematic illustration of the switchable plasmonic device. **b**. A scanning electron microscope image of the nanodisk array before 35 nm GdO_x and top electrode deposition. The scale bar is 200 nm. **c**, Optical image (left) and simulated colors (right) of the device as fabricated, after applying +5 V for 2 mins and after applying -2 V for 1 h.

5.4 Giant Reversible Switching of Effective Refractive Index

We observed that the optical properties can be switched not only through hydrogen gating of metallic and plasmonic structures, but also through large and reversible changes in the optical properties of the GdO_x dielectric layer itself. We demonstrate this by examining interference color switching in Ta(3 nm)/Au(3 nm)/GdO_x(50 nm)/Au(3 nm) stacks grown on Si/SiO_2(t_{SiO2}) and gated using a cross-bar structure (Figures 5.4a,b). Here, the thickness of the SiO_2 layer (t_{SiO2}) was varied from 110 nm to 420 nm, so that the reflected color due to thin-film interference varies over a wide range. The variation of t_{SiO2} also provides multiple data points for studying the mechanism of color switching. Figure 5.4c shows a plan-view optical micrograph of a device with t_{SiO2} = 270 nm in the virgin state. Figure 5.4d shows that the device color changes from blue to green upon positive bias application in ambient atmosphere, and Figure 5.4e shows that this color change can be modeled by an increase by ~0.4 of the real part of the refractive index of GdO_x upon hydrogen injection. Figure 5.4f shows that the identical index change can closely reproduce the color change observed for an array of devices with different t_{SiO2}, which act as switchable color interference devices.

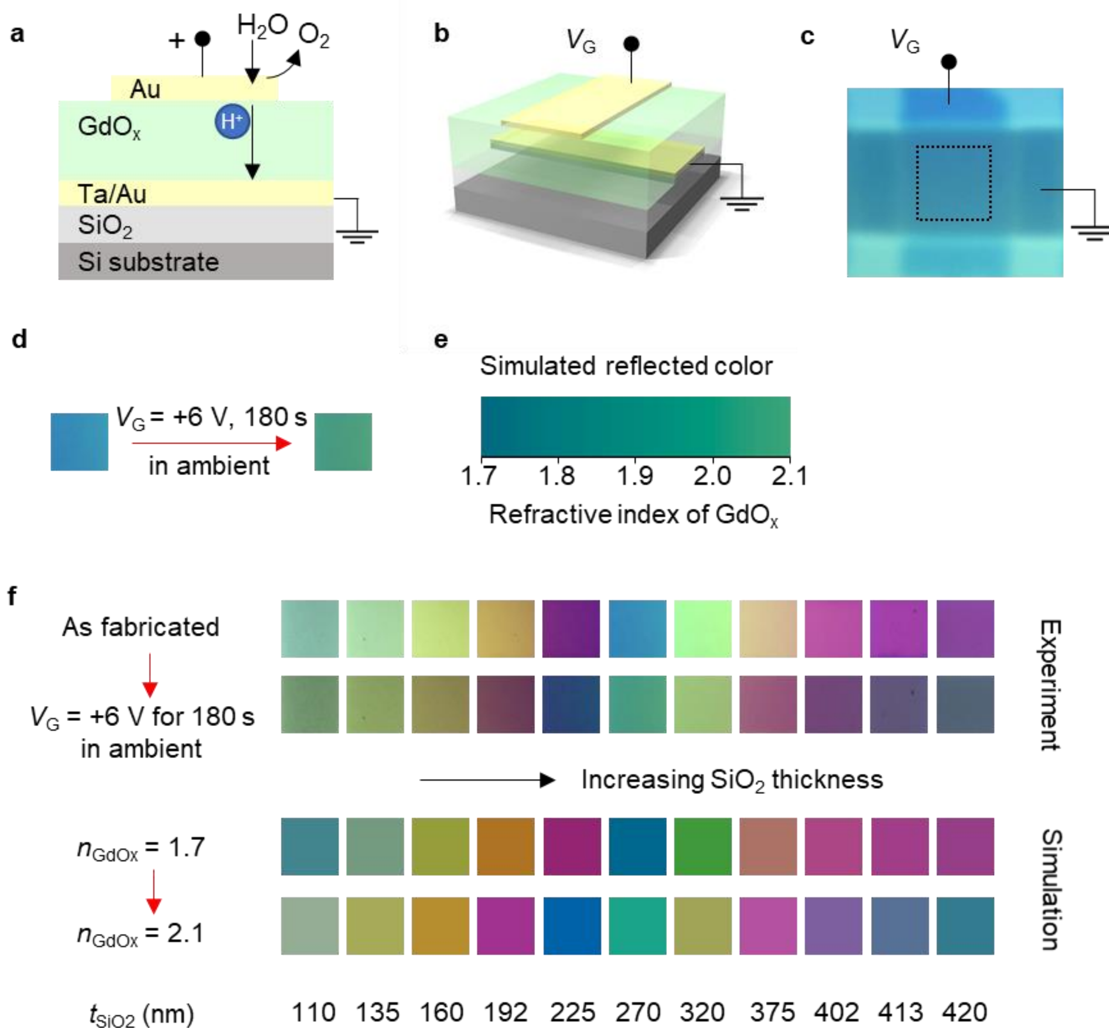

Figure 5.4. Electrochemical switchable color from solid state thin films. **a**, Schematic illustration of interference color switching device. When a $V_G > 0$ is applied, water from the ambient is dissociated and the protons move towards the bottom electrode and incorporate into GdO_x film. **b**, Schematic illustration of interference color switching device with a crossbar structure. **c**, Optical image of a typical device as fabricated. Probes are landed on the top and bottom electrode. **d**, Optical images of a device with 270 nm SiO_2 before and after voltage application in ambient. **e**, Simulated reflected color of the device as a function of the refractive index of GdO_x. **f**, Optical images of devices and simulated colors with increasing SiO_2 thickness from the left (110 nm) to the right (420 nm).

The reflectance spectra of the interference color switching devices were measured before and after $V_G = +6$V for 30 s as shown in Figure 5.5a (left). The spectra were simulated by the transfer matrix method and are shown in Figure 5.5a (right). The refractive index of GdO_x used in simulation is

shown in Figure 5.5b. The virgin state GdO_x refractive index is taken from ref[107]. The small imaginary part is ignored and assumed to stay zero when loaded with hydrogen. The simulation and experimental data show good agreement in virgin state spectrum, in that the peaks red shift with hydrogen loading. The experimental data shows lower reflectance at shorter wavelength than the simulation which is likely due to scattering caused by absorption and inhomogeneity of optical property change during voltage gating.

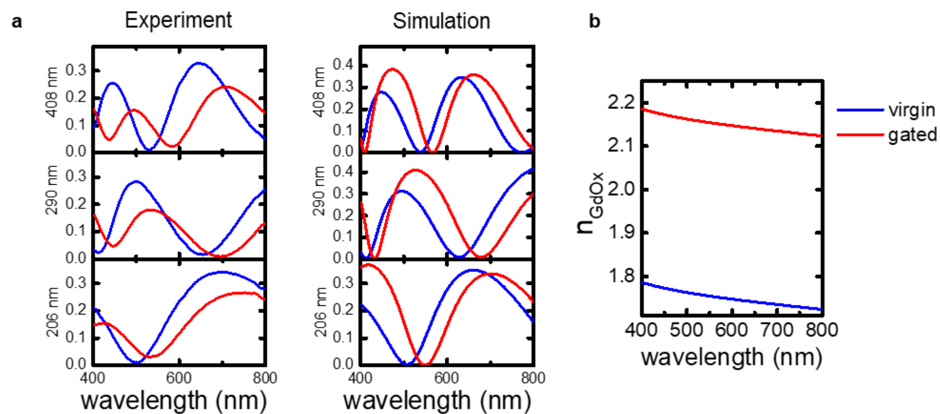

Figure 5.5. a, Measured and simulated reflectance of interference color devices with three different t_{SiO2}, before and after hydrogen loading. **b**, Refractive indices of GdO_x used in the simulation (adapted from ref[107]).

The observations and simulations hence suggest that a substantial change in the optical path length in the visible spectrum from voltage application is responsible for the observed color change. We attribute this effect to hydrogen accumulation in the GdO_x layer, which could occur through conversion to a mixed oxide-hydroxide phase changing the optical index and effective thickness, although the detailed mechanism remains to be understood. Nonetheless, the magnitude of change in effective refractive index is extremely large, comparable only to the index change achievable using liquid crystals or phase-change materials[32,41,42,111].

We note that the GdO_x refractive index change was taken into consideration in the simulations of the yttrium interference switching, and Mg plasmonic switching devices and found to play a minor role in the observed behaviors in those devices. In the plasmonic devices, the direction of the peak shift due to the change from Mg to MgH_x and from the increase of refractive index of GdO_x oppose each other, but the change from Mg to MgH_x dominates. The contributions from Y/Mg and GdO_x are compared, and The GdO_x refractive index change was found to play a minor role in the observed behaviors in the yttrium interference switching, and Mg plasmonic switching devices. For the yttrium interference switching devices, simulations were carried out with GdO_x refractive index of 1.7 and 2.1, and the reflected colors at hydrogen loaded state are shown in Figure 5.6. The minor difference in colors demonstrates that the color change with hydrogen loading is primarily due to the change of yttrium, and the refractive index change of GdO_x only contributes minor change to the colors.

Figure 5.6. Experiment micrographs and simulated colors of yttrium gating reflection devices with different GdO_x refractive index when loaded with hydrogen. The refractive index change of GdO_x only contributes minor change to the colors.

Similarly, for the Mg plasmonic switching devices, simulations were carried out with GdO_x refractive index of 1.7 and 2.1, and with Mg unloaded and loaded with hydrogen. The reflected colors are shown in Figure 5.7. Comparing to Figure. 5.3c, the agreement to the experimental result is better with n=1.7 for the hydrogen unloaded state and n=2.1 for the loaded state. The results indicate that the plasmonic color change with hydrogen loading is primarily due to the optical

change of Mg to MgH_2, and the refractive index change of GdO_x only contributes minor change to the colors. Here we note that although the color change due to refractive index change alone is small, it is still significant to the point that the patches of colors shifted by an equivalent of ~20 nm in diameter of the nanodisks in the case of the Mg unloaded state. This suggests that plasmonic color switching devices can be made without a metallic hydrogen storage bottom layer.

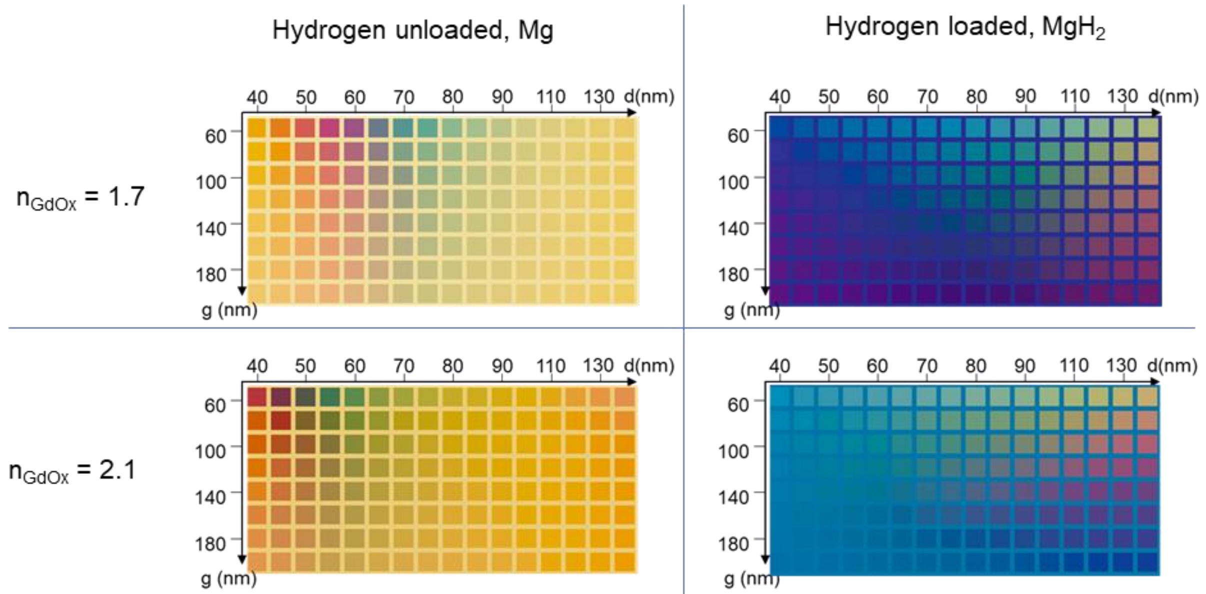

Figure 5.7. Simulated colors of plasmonic switching device with different GdO_x refractive indices and different Mg hydrogen loading states. The agreement to the experimental result is better with n=1.7 for the virgin state and n=2.1 for the hydrogen loaded state.

5.5 Switching Performance

Next, we characterized the switching ratio, speed and cyclability of the voltage gated optical devices, as these are important performance metrics for display applications. We first studied the amplitude of reflectance modulation as a function of wavelength in a series of GdO_x interference switching devices with different t_{SiO2} as described in Section 5.1. As shown in Figure 5.8a, the

reflectance modulation ratio exhibits a maximum in a wavelength range that can be tuned throughout the visible spectrum by the choice of t_{SiO2}.

We then studied the switching dynamics of the voltage gated devices. The devices are classified into two types according to where the hydrogen is loaded. Type 1 devices include the GdO_x interference switching devices without a hydrogen-switched metallic layer at the bottom. In these devices, the optical modulation is due to hydrogen loading into the GdO_x layer. Type 2 devices have a metallic hydrogen-switched layer in the bottom, whose optical properties are modulated through voltage-gated hydrogen loading/unloading. This class of devices includes the transmission switching devices with Mg, interference switching devices with Y, and plasmonic switching devices with Mg. The switching dynamics of the two types of devices are determined by three processes: the water hydrolysis reaction at the top electrode, the transport of protons through GdO_x, and the loading/unloading of hydrogen in the bottom metallic layer or the GdO_x layer. The two types of devices only differ in the third process, while they show different switching speeds. With the analysis below, we show that the gating process introduced here through the first two processes is fast, with switching time down to ~10 ms.

The switching dynamics of Type 1 devices were characterized by measuring the time-resolved reflectivity change using a 532 nm laser beam focused on the device and measuring the reflection intensity with a fast photodiode and the results are summarized in Figure 5.8b-f. Here, we used the GdO_x interference switching device with t_{SiO2} = 408 nm shown in Figure 5.8a, whose reflectivity modulation ratio is maximum at the probe laser wavelength. Figure 5.8b shows the reflectivity measured while V_G was cycled between +6 V and -2 V steps at 4 s intervals. We find that the device response is reversible and asymmetric, with hydrogen unloading occurring more rapidly than loading. To quantify the switching speed, switching transients with different V_G steps were

measured as the reflectance normalized by the value at the beginning of the rising/falling edge. Figure 5.8c shows reflectance transients for positive-going voltage steps, transitioning from V_G = -4 V to various positive values of V_G. Figure 5.8d shows similar measurements for negative-going voltage steps transitioning from a fixed V_G = +8 V to various negative voltages. Switching transient measurements were also carried out on another device with a thinner 10 nm GdO_x layer (Figures 5.8e and 5.8f).

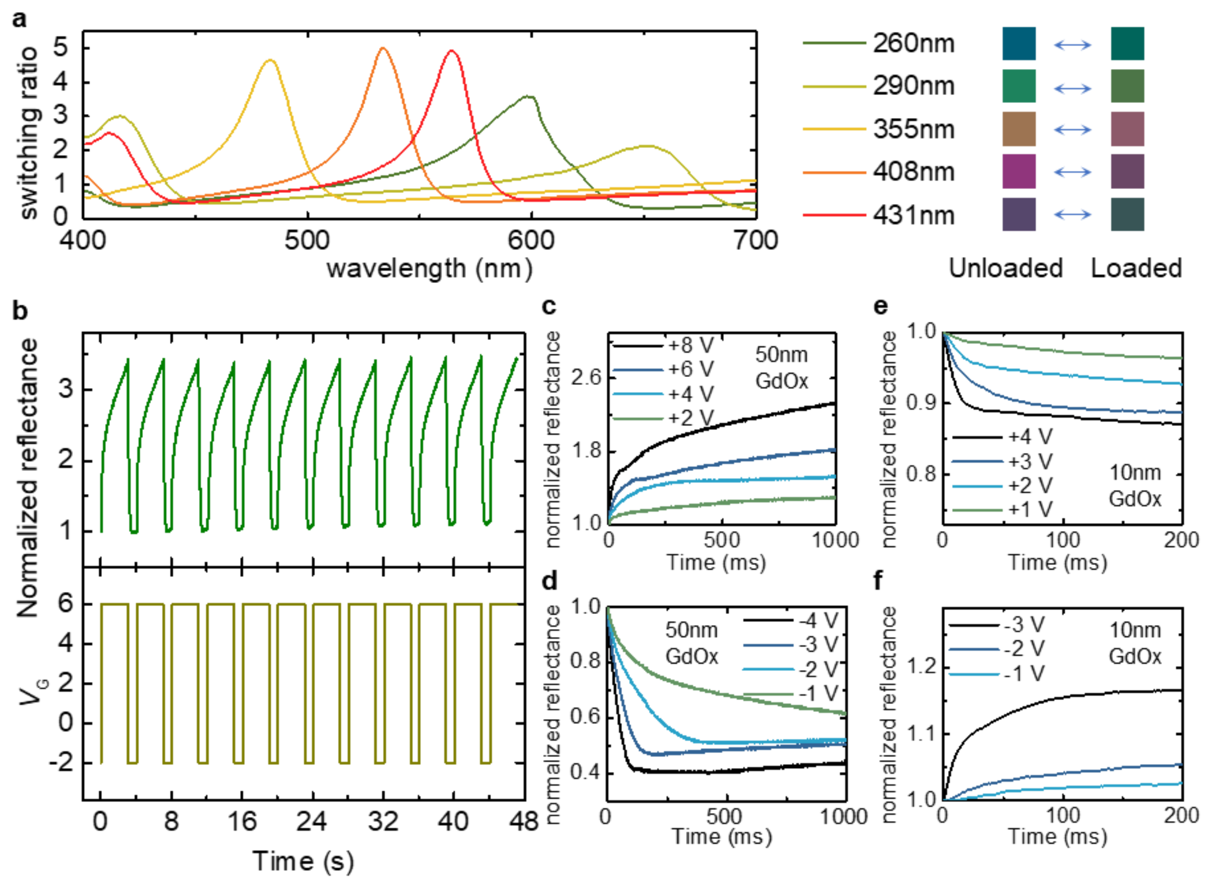

Figure 5.8. Switching ratio, reversibility and response time. a, Reflectance switching ratio versus wavelength for five devices with different SiO_2 thicknesses. The thickness of SiO_2 and the color of the device in both states are shown in the legends. **b,** The normalized reflectance of the 408 nm SiO_2 sample measured by a 532 nm and V_G as a function of time. The reflected color can be cycled multiple times reversibly with ratio of ~3. **c** and **d,** Reflectance of the optical device as a function of time measured by a 532 nm laser, showing the switching transient of a device with 50 nm GdO_x, switching from V_G = -4 V (c) and from V_G = +8 V (d) to the voltages labeled on plots. **e** and **f,** Reflectance of the optical device with 10 nm GdO_x and 400 nm SiO_2 measured by a

660 nm laser as a function of time, switching from V_G = -3 V (e) and V_G = +4 V (f) to the voltages labeled on the plots.

The switching time dynamics of the GdO_x interference switching devices (Type 1 devices) shown in Figure 5.8 was characterized by measuring time-resolved reflectivity transients at a fixed wavelength during hydrogen loading and unloading. We find that the switching transients can be well-fitted by double-exponential functions with two separate time constants, suggesting that the rate of insertion/removal of hydrogen depends on the instantaneous concentration of loaded hydrogen: hydrogen can be rapidly pumped into an initially hydrogen-free layer, but the rate of hydrogenation decreases with time; likewise, the rate of hydrogen removal is faster immediately when a gate voltage is initially applied, and it declines with time. Although a detailed analysis of the hydrogen loading and unloading kinetics, accounting for the multiple processes involved, is beyond the present scope, we here characterized the dynamics as a function of V_G and GdO_x thickness by considering the rate of the initial transient response during hydrogen loading/unloading. In this way, we compare the rate of hydrogen insertion/removal amongst devices and bias conditions under a common hydrogen-loaded state for each measurement (either the hydrogen-depleted state for hydrogen loading measurements, or the hydrogen-saturated state for hydrogen unloading measurements.)

From the switching transients in Figure 5.8, we extracted two timescales: the rate of reflectivity change at the initial application of V_G, and a time constant $T_{1/2}$ which corresponds to the time to reach 50% of the maximum observed reflectivity change. These timescales are shown are shown in Figures 5.9a,b as a function of V_G for devices with two GdO_x thicknesses. The rate of change at the initial application of V_G increases with increasing amplitude of V_G for both the 10 nm and the

50 nm thick GdO_x devices and for both the falling and rising edge of V_G, which we attribute to faster electrochemical reaction kinetics and faster proton migration through the oxide induced by larger V_G. With larger V_G, shorter time is needed to achieve 50% change as $T_{1/2}$. The only exception is that for the device with 50 nm GdO_x, $T_{1/2}$ is higher at positive V_G of +6V and +8V than V_G of +4V, which suggests that large positive V_G may activate the formation of a different phase that has different time dynamics. However, we caution that if the optical change does not saturate in the measurement window, then comparison of $T_{1/2}$ for different V_G may not be applicable, since the time to reach saturation at small V_G may be very much longer than the $T_{1/2}$ corresponding to the apparent saturation in the measuring time window.

The thickness of GdO_x is also an important factor in the time dynamics. A direct comparison of the rate of change at the onset of V_G is not applicable between the two types of devices because the rate of change is not only proportional to the speed of the optical property switching but also the sensitivity of the reflectivity to the optical property change determined by the optical stack and incident wavelength. The time constant on the other hand gives a better comparison for different device configurations. As shown in Figure 5.9c, the time constant $T_{1/2}$ is smaller for device with thin GdO_x oxide at positive V_G edge. At the edge of negative V_G, the $T_{1/2}$ of devices with thin and thick oxide layer is comparable at -1V and -2V, and the device with 10 nm GdO_x has much smaller $T_{1/2}$ than the device with 50 nm GdO_x at -3V. The fastest switching ($T_{1/2}$ ~ 10 ms) is achieved for the device with 10 nm thick GdO_x and at V_G of +4V and -3V. Because the optical change originates from the GdO_x layer itself, a change in the GdO_x thickness also changes the amount of hydrogen that can be loaded into the device, which complicates the time dynamics comparison between devices with different GdO_x thickness.

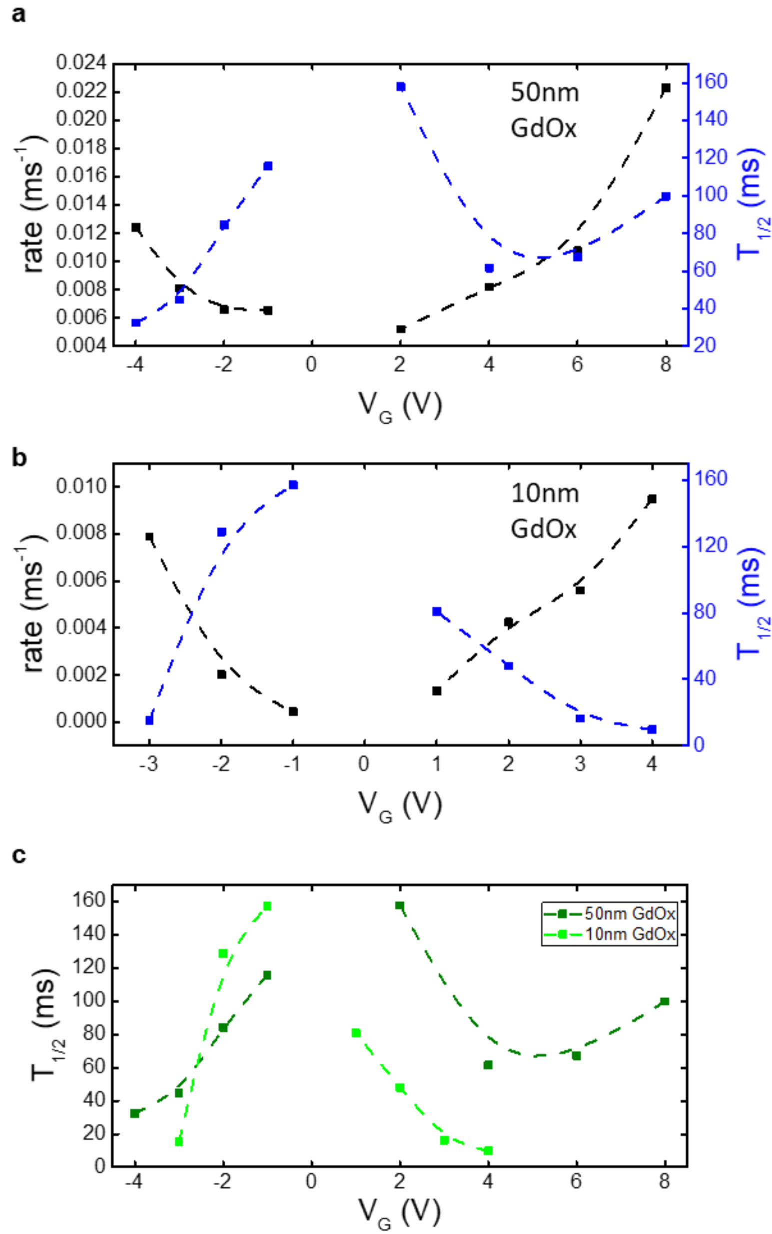

Figure 5.9. Switching time dynamics of GdO_x interference device. a and **b**, rate of reflectivity change at the initial application of V_G and $T_{1/2}$ versus V_G for devices with GdO_x thickness of 50nm (a) and 10nm (b). **c**, $T_{1/2}$ versus V_G for devices with GdO_x thickness of 50nm and 10nm.

The total device thickness responsible for the gating (excluding the Si/SiO_2 substrate) is around 20 nm for devices with 10 nm GdO_x. The result indicates that it is possible to achieve optical

property modulation with total device thickness of ~20 nm and switching speeds on the order of 10 ms in these devices. The results suggest that the speed can potentially be further improved by replacing GdO_x with materials with higher proton conductivity and improved tolerance to large V_G.

We then studied the switching dynamics for Type 2 devices. We studied the switching transient of the Mg plasmonic switching devices by extracting the mean red channel intensity value from images captured from a CCD camera, using only regions without Al nanostructures. The result for V_G of +5V and -2V is shown in Figure 5.10. The switching time constants $T_{1/2}$ for both the hydrogenation and dehydrogenation processes are on the order of seconds or more. In contrast, the switching time of GdO_x interference switching devices with even thicker GdO_x layer under the same V_G is around 100 ms as shown in Figure 5.9.

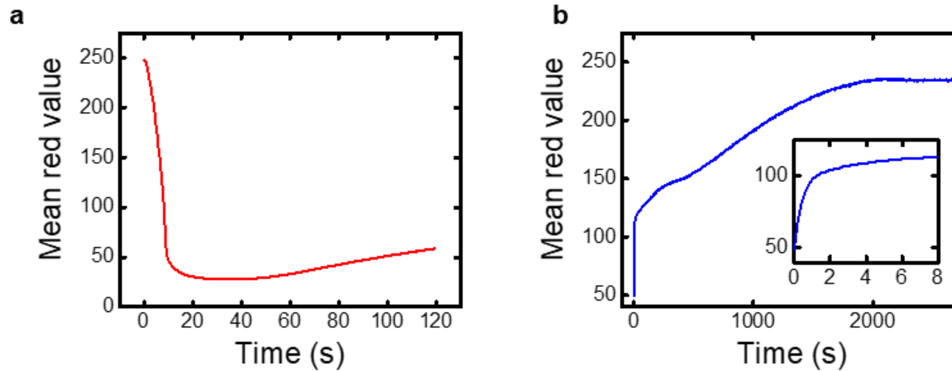

Figure 5.10. Switching transient for Mg optical switching device during hydrogenation with V_G = 5 V (a) and dehydrogenation with V_G = -2 V(b). The inset in b is the plot zoomed-in near the beginning of V_G application.

The result suggests that the interfacial reaction at the top electrode and the diffusion of hydrogen through the GdO_x layer is not limiting the speed of the switching. Instead, the hydrogenation/dehydrogenation of Mg and Y are likely to be the rate limiting step for Type 2 devices. As a result, we expect that the switching speed of Type 2 can be optimized by

modifications such as adding a buffer layer between the metallic layer and the Pd capping layer[48], using a nanostructured metallic layer to increase the surface area for hydrogenation[50], and using hydrogen switchable materials with faster absorption/desorption kinetics such as Mg-Ni alloy[34] to achieve faster switching.

Finally, we comment on device cyclability. As shown in Figure 5.8b, the devices of Type 1 can be cycled reversibly over many cycles without significant change in device performance. In performing the measurements shown, the devices were cycled for several hundred cycles without degradation. In some devices, failure occurs through a sudden increase in leakage current, consistent with dielectric breakdown of the GdO_x. We find that failures occur more frequently with larger-area devices, which is consistent with this failure mode. This observation suggests that the cyclability of the devices can potentially be optimized by improving oxide uniformity to reduce pinhole formation, or by using an electronic blocking layer in the device to minimize the electronic current. We note that voltage gated magnetic devices using a GdO_x gate layer have recently been shown to be reliable for several thousand switching cycles[7].

5.6 Additional Implementations of Color Switching Devices

In this section, several additional implementations of color switching devices will be discussed, and the preliminary results will be shown. We focused on voltage control of plasmonic response based on the reversible refractive index change of GdO_x, and voltage control of the color of devices with nanohole array as the top electrodes.

The plasmonic color switching devices shown in Section 5.3 are based on hydrogen-switching of a metallic layer in the heterostructures. It is also possible to achieve plasmonic color change simply by hydrogenating the GdO_x layer, which is significantly faster. Figure 5.7 (left) shows that the effective refractive index change of GdO_x makes a significant contribution to the color change of the plasmonic devices, corresponding to color shifts by an equivalent of ~20 nm in diameter of the nanodisks. This suggests that fast plasmonic color switching can be achieved by just changing the effective refractive index of GdO_x via voltage gating without the rate limitation from hydrogen loading/unloading of a metallic layer.

We fabricated Al nanodisk arrays with diameters ranging from 80-160 nm and periodicity ranging from 160-240nm on a glass substrate coated with ITO. The height of the Al nanodisks are 20 nm. The gating device was completed by growing 65 nm of GdOx and circular Au top electrodes with thickness of 3 nm. The optical image of the device is shown in Figure 5.11. Bright and vibrant colors were observed from the nanodisk arrays with different nanodisk diameters and periodicity. However, a gate voltage was not able to switch the colors, which we attribute to the extremely low hydrogen diffusivity and proton conductivity of Al_2O_3 formed when Al nanoparticles were exposed to air following GdO_x deposition. The result shows that it is possible to achieve different colors with the same layer stack by just varying the geometry. The result also indicates that a dense oxide layer should be avoided in order to allow electric contact between the electrolyte and the nanodisks.

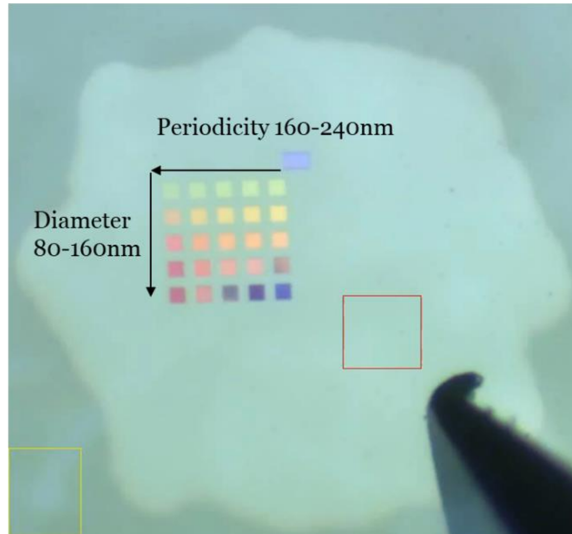

Figure 5.11. Reflected colors from Al nanodisk arrays with varying periodicities and diameters showing bright colors.

We then fabricated similar structures with Au nanodisks instead of Al. Figure 5.12 (top) shows the reflected image as fabricated (left) and after a gating sequence was applied. The colors of the nanodisk arrays were not as vibrant as the one made of Al, but with a gate voltage applied to the top electrodes, reversible color change was observed from the devices.

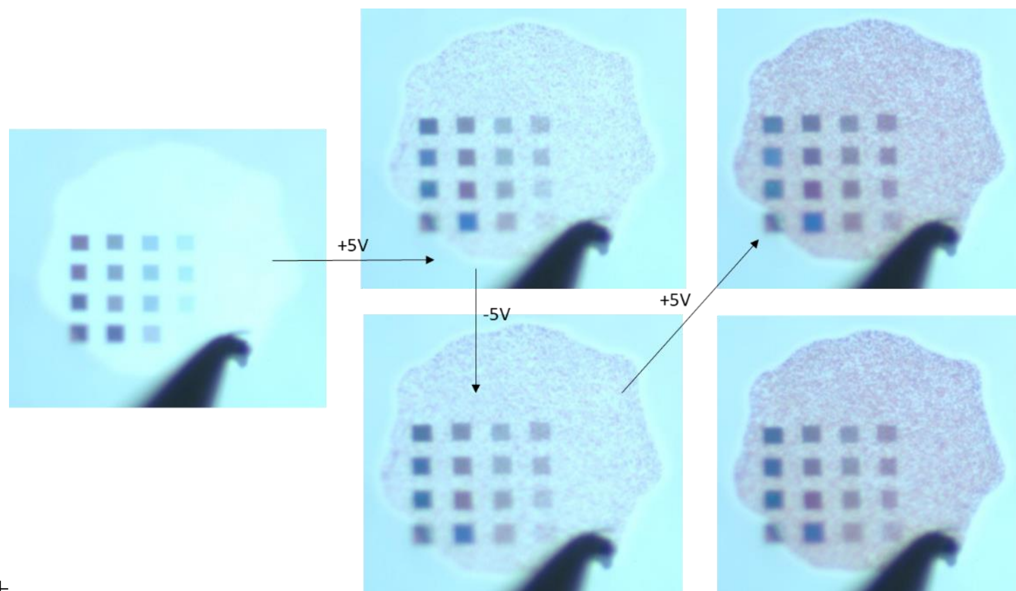

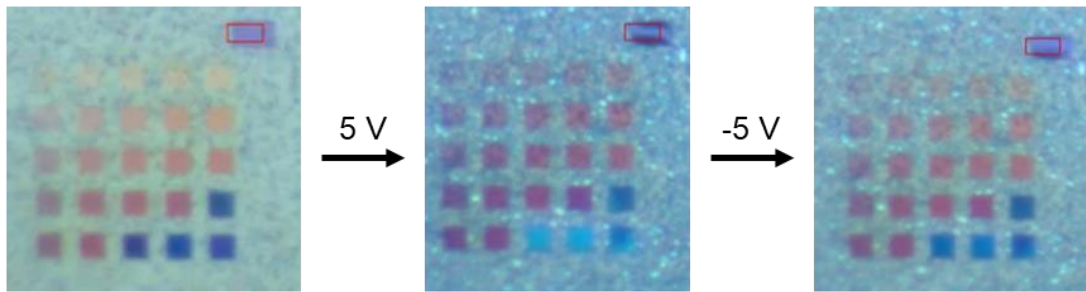

Figure 5.12. Reflected images of voltage controlled plasmonic color devices with Au nanodisk arrays (top) and Al(20 nm)/Au(4 nm) nanodisk arrays (bottom) as fabricated, after V_G = 5 V was applied and after -5 V was applied subsequently.

An alternative approach to prevent the formation of a dense oxide layer is to cap the Al with a thin layer of inert material. Similar switchable plasmonic color device was also fabricated with 20 nm of Al capped with 4 nm of Au. As shown in Figure 5.12 (bottom), by applying voltage to the top electrode, reversible color change was also observed.

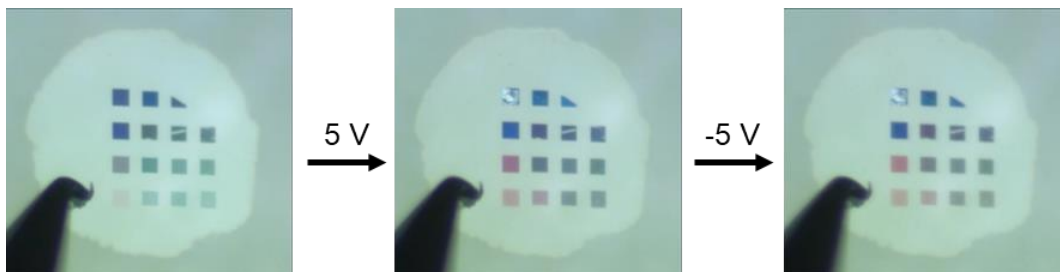

Figure 5.13. Reflected images of voltage controlled plasmonic color device with a 1nm thick Co layer as fabricated, after V_G = 5 V was applied and after -5 V was applied subsequently. The gated region was smooth after gate voltage application.

We also notice that non-homogenous features appear in the region without plasmonic nanodisks in the devices after gating in Figure 5.12. We attribute the inhomogeneous feature to hydrogen gas bubble formation with gate voltage application due to poor adhesion of GdO_x to ITO in these devices. The inhomogeneous features can be effectively removed by depositing a thin layer of material such as Co as shown in Figure 5.13.

In addition to controlling the optical properties of the dielectric medium surrounding plasmonic nano structures, we show that effective voltage-controlled color change can be achieved with devices with nanohole array top electrodes. Figure 5.14a shows the device structure, a 20 nm thick Au top electrode layer was put on top of Ta/Pt/GdO_x layers. Figure 5.14b shows the secondary electron SEM images of the device after fabrication. The color of the device after fabrication was yellow as shown in Figure 5.14c. By applying $V_G = +7$ V to the top electrode, the color of the device changed first to red and then to blue. Figure 5.14c also shows the optical image of the device after two complete cycles showing the reversibility of the color change.

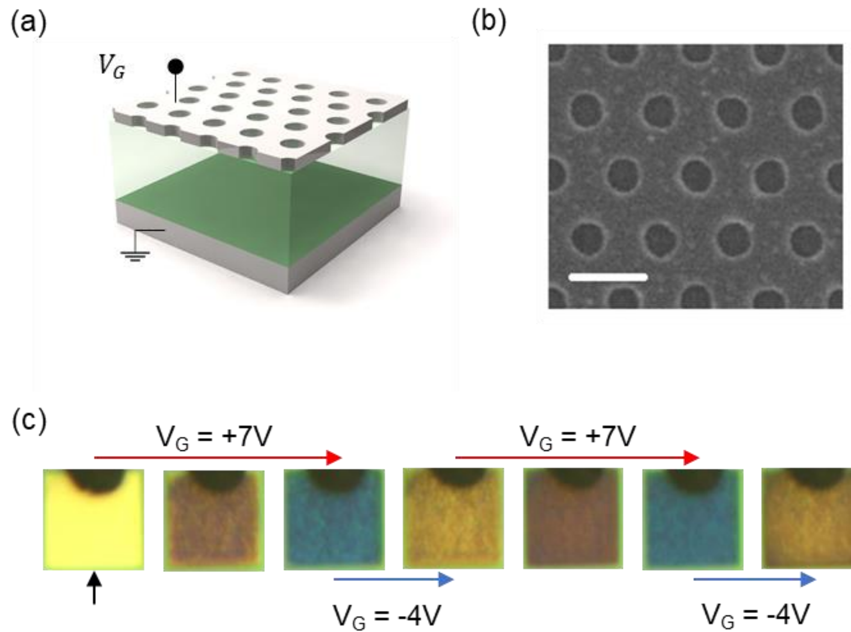

Figure 5.14. Color pixel that shows color changes through yellow, red and blue. a, Schematic illustration of the device structure. **b,** SEM image of the device. Scale bar, 200 nm. **c,** optical images of the pixel as fabricated and after a series of voltage applications.

We further demonstrate a dynamic color picture of a leaf using the same device structure with high resolution features by using electron beam lithography. Figure 5.15 (a) shows the design layout of the device. Electron beam lithography was used to define a leaf pattern with two regions. The two

regions were separated by gaps with the smallest width of <400 nm. Figure 5.15 (c) shows the optical images of the devices as fabricated and after positive V_G pulses of different lengths were applied to the two top electrodes. The background region changed to blue and the leaf region changed to red. The small feature size and the fact that there was no leakage between the two regions indicate the localization of voltage-controlled color with this approach.

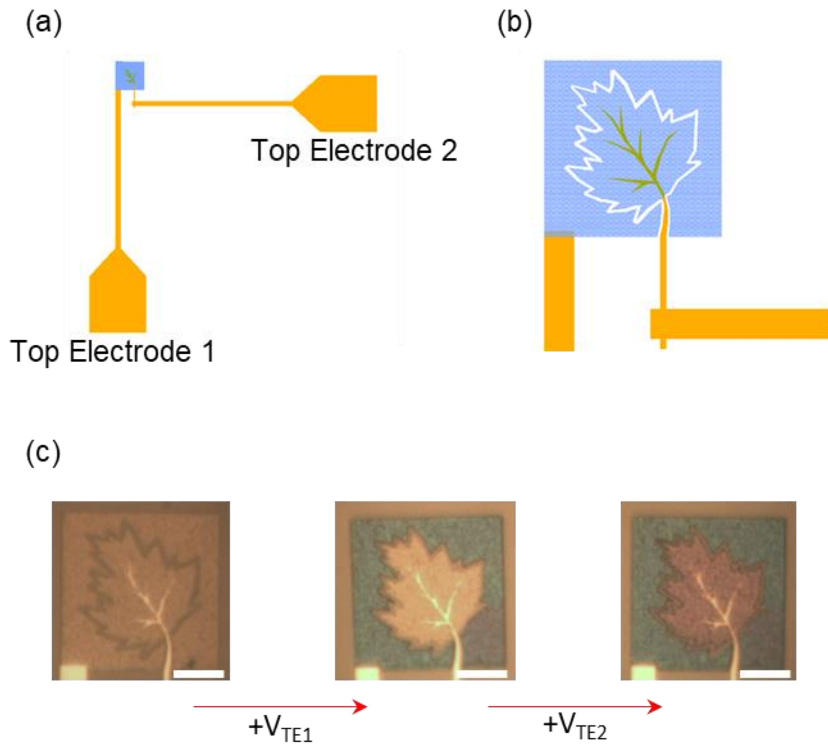

Figure 5.15. High resolution demonstration. a, Lithography layout of the dynamic color images of a leaf. **b,** Zoomed in to the main region. **c,** Optical images of the image as fabricated (left), after voltage application to Top Electrode 1 (middle), and then after voltage application to Top Electrode 2 (right), showing that different parts of the image can be addressed individually, with gaps smaller than 400 nm and undetectable leakage current between the two electrodes. The scale bars are 10 μm.

5.7 Discussion

We demonstrated all-solid-state thin film devices with electrochemically switchable optical properties through hydrogen loading/unloading using a simple gate oxide. Reflectance, transmittance and plasmonic response gating over a wide range can be achieved by reversibly pumping hydrogen into and out of the system, based on electrocatalysis at the electrode/air interface. The active oxide can be made as thin as 10 nm so that the optical modulation can be highly localized, and high switching speeds can be achieved. The versatile system has great potential to be applied in plasmonic devices and active metamaterials to achieve control of optical properties at the nanoscale.

Two types of switching mechanisms are studied: Type 1 devices modulate optical responses with hydrogen loading into the electrolyte layer, while Type 2 devices include a hydrogen-switched layer as the bottom electrode. As discussed above, the speed of Type 1 devices are as fast as around tens of milliseconds, so these devices are potentially applicable for devices that require fast optical property change such as displays. The speed can potentially be further improved by replacing GdO_x with materials with higher proton conductivity and improved tolerance to large V_G. Simulations also suggest that the inclusion of plasmonic structures in adjacent to the electrolyte materials may provide improved switching contrast. For Type 2 devices, we show that the speed is limited only by the hydrogenation/dehydrogenation process of the hydrogen switchable materials, not by the hydrogen pumping mechanism. We expect that the speed can potentially be optimized by modifications such as adding a buffer layer between the metallic layer and the Pd capping layer, using a nanostructured metallic layer to increase the surface area for hydrogenation, and using hydrogen switchable materials with faster absorption/desorption kinetics such as Mg-Ni alloy to achieve faster switching. The comparison of speed of hydrogenation for Mg and Mg-Ni

alloy is shown in Figure 4.5a. In addition to metallic hydrogen storage materials, we expect electrochromic oxide such as WO_3 to be promising candidates for achieving faster optical switching and/or additional degree of freedom in terms of optical design. For both types of devices, we have used GdO_x as a proton conducting layer, other proton conducting oxides such as $Y{:}BaZrO_3$[112,113] may provide even faster performance, leading to ultrafast switching for displays and optical modulation applications.

In addition, the ultra-thin solid-state stack structure of the devices allows the use of flexible substrates and realization of ultrathin pixels whose lateral dimensions can hence be scaled to deep sub-wavelength for high-resolution optical and holographic display applications.

Chapter 6
Voltage Control of Ferrimagnetic Order and Voltage-Assisted Writing of Ferrimagnetic Spin Textures by Solid-State Hydrogen Gating

Controlling the magnetic state of a material by electrical means is a key to spin-based data storage and more efficient data manipulation[114,115]. One key technological challenge is to achieve 180° magnetic switching efficiently by electrical means. The present methods are mainly based on local magnetic fields or spin torques[116,117]. It is desirable to switch magnetization with a voltage, which has the potential to minimize energy consumption[118,119], however it is inherently difficult because electrical fields do not induce time-reversal symmetry breaking, as is required for 180° magnetic switching. Many methods for voltage-controlled magnetization switching are being explored including manipulating magnetization with piezoelectric material and using multiferroic materials[118,120–124]. These methods require either high voltages to induce enough strain or difficult growth and device fabrication procedures.

Ferrimagnets are ideal candidates for achieving 180° switching owing to a multi-sublattice configuration with magnetic moments of different magnitudes opposing each other. If the relative magnitude of magnetic moment of the sublattices can be controlled, the sign of the net magnetization can be inverted. Moreover, ferrimagnets have technological advantage over

ferromagnets as they allow for fast spin dynamics[60,63,125], small spin textures[60], and ultrafast optical switching[58]. However, the usual means of controlling compensation behavior in ferrimagnets, such as varying the composition at fabrication[126], changing the temperature[127], annealing[128,129], and hydrogen gas exposure[130,131] do not allow for localized electrical actuation.

Here we show that the dominant sublattice of a rare-earth transition-metal alloy (RE-TM) ferrimagnet (GdCo) can be controlled reversibly by a gate voltage using a solid-state hydrogen pump[7]. The control originates from hydrogen injection into GdCo sourced from ambient moisture through hydrolysis. Using a small gate voltage, the compensation temperature (T_M) can be shifted by >100 K. *Ab initio* calculations suggest that this effect is due to a larger decrease of the Gd sublattice moment than the Co sublattice moment with hydrogen loading, resulting from a drastic decrease of the inter-sublattice exchange coupling between Co and Gd sublattices. Applying this approach, the sign of the polar-magneto-optical contrast and the polarity of the anomalous Hall effect in out-of-plane magnetized thin film ferrimagnets can be switched by gate voltage application, reflecting a change in the dominant sublattice. Dominant sublattice switching can be toggled at room temperature using pulses as short as 50 μs, and devices show no degradation after cycling in excess of 10^4 cycles. With a constant field, the Néel vector of the film can be switched 180 degrees just by applying a gate voltage. In addition, the exchange bias field in GdCo/NiO exchange-coupled stacks can be reversibly inverted. Moreover, the approach allows for localized electrical control as we further demonstrate through reverse domain generation and skyrmion bubble generation in racetrack-like devices[114,115]. The approach provides a new type of magnetic bit writing, a new platform for voltage control of magnetism and may also find applications in magneto-optical modulators[132].

6.1 Experiment Methods

Sample preparation: Samples with three types of layer structures were fabricate. Samples for MOKE measurement have a layer structure of Ta(3 nm)/Pd(6 nm)/$Gd_{45}Co_{55}$(6nm)/Pd(10 nm)/GdO_x(30 nm)/Au(3 nm). Samples for electrical measurements, demonstrating reverse domain generation and structural characterizations have a layer structure of Ta(3 nm)/Pt(3 nm)/$Gd_{45}Co_{55}$(6 nm)/Pd(6 nm)/Al_2O_3(20 nm)/GdO_x(30 nm)/Au(3 nm). Samples for demonstrating switchable exchange bias have a layer structure of Ta(3 nm)/Pd(10 nm)/NiO(30 nm)/Pd(0.6 nm)/$Gd_{45}Co_{55}$(10 nm)/Pd(10 nm)/GdO_x(30 nm)/Au(3 nm). All samples were grown using magnetron sputtering at nominal room temperature. The Ta, Pt, Pd, GdCo and Au layers were grown using d.c. sputtering. Au was grown under 3.5 mTorr Ar and the rest was grown under 3 mTorr Ar sputtering gas. The NiO layer was grown reactively under 3 mTorr Ar with P_{O2} of 0.05 mTorr. The Al_2O_3 layer was grown reactively under 3 mTorr Ar with P_{O2} of 0.1 mTorr. The GdO_x layer was deposited using radio-frequency sputtering with 3 mTorr Ar and P_{O2} of 0.7 mTorr. The exchange biased samples were grown with an out-of-plane bias field of 2.8 kOe. The thickness of the Pd layer between NiO and GdCo was optimized to minimize the reduction of NiO and the oxidation of GdCo while maintaining the exchange bias[133].

Shadow masking was used to pattern top Au electrodes for the MOKE measurements. The Au(3 nm) top electrodes are of size around 200 x 200 μm. The domain wall tracks and Hall crosses were patterned using photolithography and ion milling. The Al_2O_3 hydrogen blocking layer, GdO_x electrolyte layer and Au top electrode layer for gated Hall cross and gated racetracks were patterned using photolithography and lift-off. The device layouts are shown in Figure 6.1.

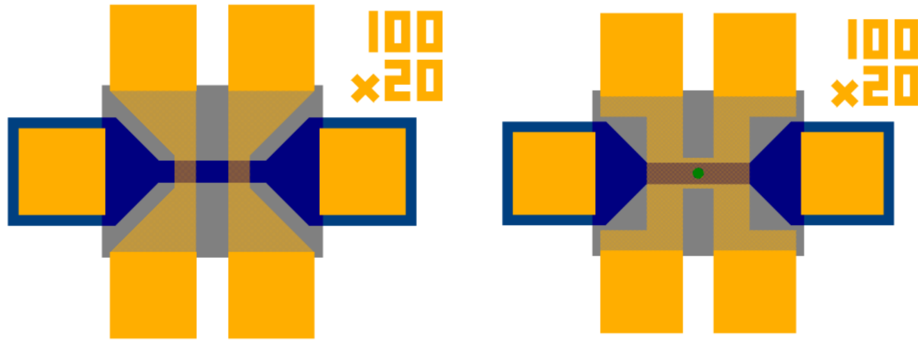

Figure 6.1. Device layout of reversed domain (left) and skyrmion bubble generators (right).

The fabricated Hall crosses had channel dimension of 6 x 6 μm. The domain wall tracks are 200 μm long and 20 μm wide. The skyrmion tracks are 200 μm long and 100 μm wide with an 80 μm wide region of length 50 μm in the center. The Al_2O_3 hydrogen blocking layer was incorporated into the skyrmion racetrack only. The blocking layer was patterned with a 20 μm diameter circular hole, located at the center of the gate electrode.

Polar laser and wide field MOKE measurements: MOKE measurement was performed using a 1 mW laser with wavelength of 660 nm focused to a spot size of about 10 μm. Measurements were performed in polar geometry which is sensitive to the out-of-plane magnetization. A CuBe probe was used to make electrical contact to the top electrodes and the bottom metal layers were contacted to at the sample edge and were grounded. The laser spot was positioned near the center of the electrodes for hysteresis loop measurements. The focused laser MOKE was integrated into a custom wide-field MOKE microscope. The MOKE differential images for shadow mask devices were obtained by subtracting the MOKE images after saturating the film along z+ direction by the images after saturating the film along z-. The MOKE differential images of the reversed domain generators were obtained by subtracting the MOKE images after current injection by the MOKE images before current injection.

Hall effect measurements: Anomalous Hall effect (AHE) measurements were performed using a lock-in amplifier with an alternating-current injected current of amplitude 0.3 mA and at frequency 10 kHz. The field was swept perpendicular to the plane with cycling time 0.1 s.

Cycling of dominant sublattice at room temperature: V_G = +2.3 V (-0.5 V) was applied to switch the device to Co (Gd) dominant state at room temperature. The AHE hysteresis loop was constantly acquired every 0.1 s. After each crossing of compensation, the polarity of V_G was switched once a loop with $H_C < 800$ Oe was acquired and met the criteria of ($|M_r/M_s| > 0.8$) for at least three consecutive loops, where M_r is the remnant and M_s is the saturation magnetization.

Current pulse injection for racetrack experiments: To displace the reversed ferrimagnetic domain along the racetrack of the reversed domain generator, current pulses with width of 10 µs were injected using contact pads patterned at either end of the track. The current density in Pt layer was 1.1×10^{11} A m^{-2}. To displace the bubble skyrmion, current pulses with width 200 µs were injected along the track, and the current density in the Pt layer was 0.8×10^{11} A m^{-2}. A small constant out-of-plane field (-10 Oe) was applied after the nucleation of the reversed bubble skyrmion to stabilize its size so that it could remain visible in wide MOKE microscopy.

Computational methods: First-principles spin polarized calculations were performed by means of the density functional theory and projector augmented wave method as implemented in the Vienna ab initio simulation package (VASP)[134]. The exchange-correlation potential was treated using the generalized gradient approximation with the Perdew, Burke, and Ernzerhof functional corrected for solids[135], including the valence states $5s^2 5p^6 5d^1 6s^2 4f^7$ for Gd and $3d^7 4s^2$ for Co. The GGA+U method[136] was applied to *f*-orbitals of Gd and *d*-orbitals of Co atoms with U_{eff} = 7 eV and 3 eV, correspondingly. A 7.31 x 7.31 x 7.31 $Å^3$ supercell of $GdCo_2$ (C15 Laves phases) containing 8 Gd and 16 Co atoms was used. k-point mesh of 8x8x8 and energy cut-off of 400 eV are applied.

Our calculations showed that hydrogen solubility is higher at 1Gd3Co tetrahedral pores and these interstitials were used to simulate hydride formation.

Magnetic coupling constants were calculated using the Heisenberg model of the exchange for nearest neighbors, described by the following Hamiltonian:

$$H = -\frac{1}{2}\sum_{\mathrm{i,j}} J_{\mathrm{ij}} \cdot \boldsymbol{S}_{\mathbf{i}} \cdot \boldsymbol{S}_{\mathbf{j}} \tag{6.1}$$

To compute the temperature-dependent equilibrium magnetizations for the $GdCo_2H_x$ we employ Landau-Lifshitz-Gilbert equation as implemented in VAMPIRE atomistic code[137]. A supercell of 5.78 x 5.78 x 5.78 nm^3 containing 12288 Co and Gd atoms was used. The effect of hydrogen absorption is introduced by modifying the set of exchange correlation constants in accordance with the results of ab initio calculations. System trajectories with 10^7 time steps (after 10^4 equilibration steps) and an integration time step of 10^{-15} s are simulated for various hydrogen concentration under constant $T = 300$ K. From these trajectories the zero-field equilibrium magnetizations of the sublattices of the ferrimagnet as well net magnetization were extracted.

6.2 Dominant Sublattice Switching and Compensation Temperature Gating

Experiments focus on perpendicularly-magnetized Gd_xCo_{100-x} (GdCo), an amorphous ferrimagnet with antiparallel Gd and Co sublattices. The dominant sublattice depends on the alloy composition and temperature (T), since the Gd sublattice magnetization (M_{Gd}) varies more strongly with T than does the Co sublattice magnetization (M_{Co}). We examined voltage-controlled hydrogen gating in Ta/Pd or Pt/$Gd_{45}Co_{55}$(6 nm)/Pd/GdO_x/Au films grown on thermally oxidized Si as described in Section 6.1.

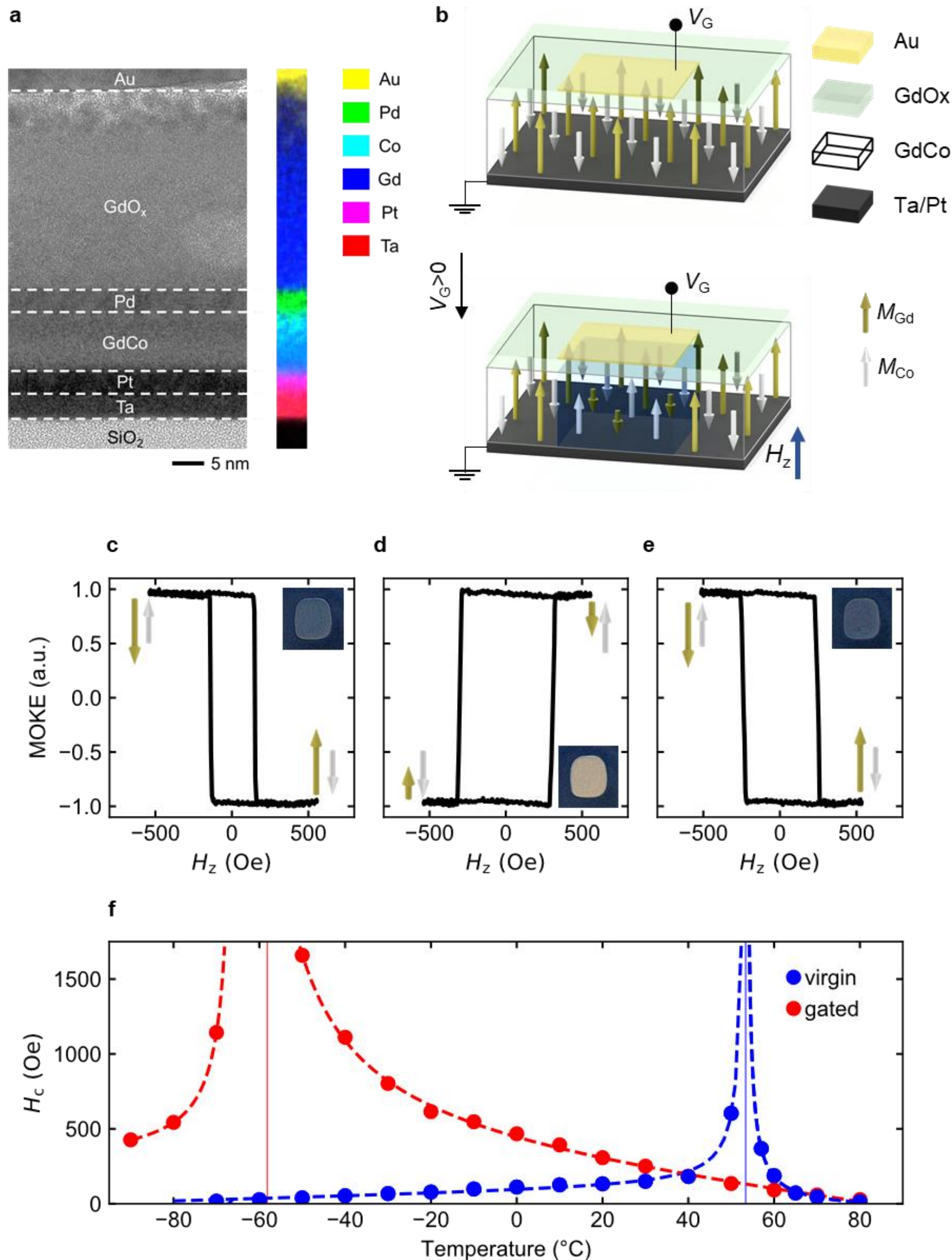

Figure 6.2. Gating of dominant sublattice and compensation temperature (T_M) of GdCo. a, Cross-sectional high resolution transmission electron micrograph (left) and energy dispersive X-ray (EDS) chemical profile of a CoGd heterostructure. **b,** Schematic illustration of the device structure in the virgin state (top) and after a positive gate voltage is applied (bottom). The Pd protection layer on top of GdCo is omitted. **c-e,** Laser MOKE hysteresis loop of the device in virgin state (**c**), after applying $V_G = +2.5$ V for 180 s (**d**), and after subsequently applying $V_G = -0.5$ V for 30 s. Insets: wide-field differential MOKE contrast images of the gate electrode area. **f,** Coercivity H_c versus temperature in the virgin state (blue) and after applying positive gate

The cross-sectional transmission electron micrograph in Figure 6.2a confirms the amorphous nature of the GdCo layer. We prepared Ta(4 nm)/Pd(6 nm)/Gd_xCo_{100-x}(6 nm)/Pd(10 nm) films with x = 39.3, 41.6, 43.8, 45.7, and 46.7. The H_c and polarity of MOKE hysteresis loops are shown in Figure 6.3. The coercivity diverges and the loop polarity inverts at $x \approx 44$, which corresponds to the compensation composition at room temperature. We estimate the composition of the samples in the main text to be $Gd_{45}Co_{55}$ based on measured H_c and the MOKE loop polarity and is Gd-dominated at room temperature

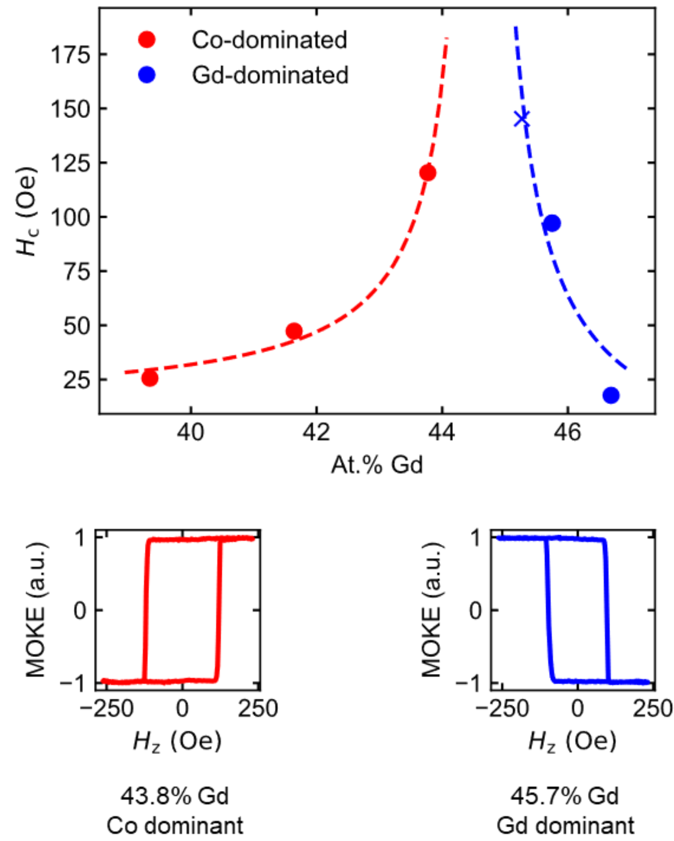

Figure 6.3. a, H_c and MOKE loop polarity versus Gd atomic percent of GdCo. b, MOKE hysteresis loops at x = 43.8 and x = 45.7.

The GdO_x/Au top gate serves to catalyze water dissociation and proton injection, sourced from ambient humidity under positive gate bias as reported previously[7]. The upper Pd layer was used to protect the GdCo from oxidation while allowing hydrogen to diffuse through[138].

To examine the effect of gate voltage on the magnetic properties, the top Au layer was patterned as an array of ~200 μm x 200 μm isolated electrodes on an otherwise continuous film, with the bottom metal layers serving as a back electrode, allowing for localized gating (Figure 6.2b). Out-of-plane hysteresis loops were measured via the polar magneto-optical Kerr effect (MOKE) using a focused probe laser spot positioned at the interior of the gate electrode. It has recently been shown[7,8,139] that in metal(anode)/GdO_x/Au stacks, a positive gate voltage $V_G \gtrsim 1.2$ V dissociates water molecules at the Au/GdO_x interface and injects protons toward the bottom electrode, where they recombine with electrons to form neutral H. Negative V_G drives the process in reverse, allowing for solid-state hydrogen loading/unloading by V_G. Figures 6.2c-e show hysteresis loops from the GdCo layer in the virgin state (Figure 6.2c), after applying $V_G = +2.5$ V for 180 s (Figure 6.2d) and after subsequently applying $V_G = -0.5$ V for 30 s (Figure 6.2e). The data reveal a reversible voltage-gated inversion of the MOKE polarity which, as seen in wide field differential MOKE contrast images (insets in Figures 6.2c-e), is localized to the gate region. Because the MOKE contrast arises primarily from the Co sublattice[62], this inversion suggests that M_{Co} switches from being antiparallel to parallel with respect to M_s under positive V_G, that is, the dominant sublattice switches from Gd to Co (Figure 6.2b) upon hydrogen loading.

voltage (red), showing > 100 °C decrease of the magnetic compensation temperature T_M by hydrogen gating.

As discussed in ref[7], in metal(anode)/GdO_x/Au stacks, by applying a positive gate voltage $V_G \gtrsim$ 1.2 V to the top Au and grounding the bottom metal layer, water from the ambient is split at the

top electrode forming oxygen and protons. The protons are driven by electric field towards the bottom electrodes where they recombine with electrons and get loaded into the bottom electrode. The mechanism was supported by X-ray absorption spectroscopy measurements[7]. Figure 6.4 shows the processes involved when a positive V_G is applied for the device structures in this chapter.

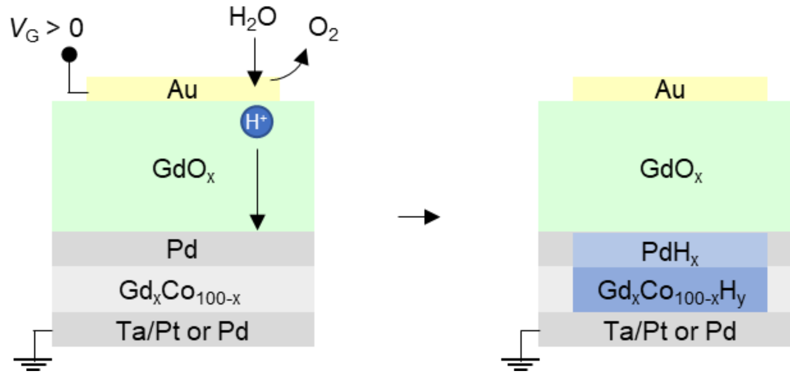

Figure 6.4. Schematic illustration of water splitting and hydrogen pumping by applying positive V_G.

The electrode reactions involved during hydrogen loading are:

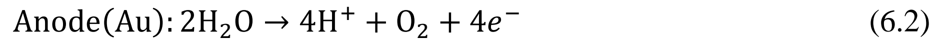

$$\mathrm{Anode(Au)}: 2\mathrm{H_2O} \rightarrow 4\mathrm{H}^+ + \mathrm{O_2} + 4e^- \tag{6.2}$$

$$\mathrm{Cathode(Pd)}: \mathrm{Pd} + \mathrm{xH}^+ + \mathrm{x}e^- \rightarrow \mathrm{PdH_x} \tag{6.3}$$

$$\mathrm{Cathode(GdCo)}: \mathrm{Gd_xCo_{100-x}} + \mathrm{yH}^+ + \mathrm{y}e^- \rightarrow \mathrm{Gd_xCo_{100-x}H_y} \tag{6.4}$$

To support the processes described above, we experimentally show the critical role of water vapor in voltage induced hydrogen loading. Experiments were carried out to study the effect of different gas environments. Five devices with the same device structure fabricated in the same batch were used in the study. The polar MOKE loops of the devices in the virgin state were measured. Then $V_G = +3$ V was applied to one device for 180 s in ambient, and the same V_G was applied to another device for 180s in vacuum ($<10^{-3}$ Torr). The other three devices were first placed in a vacuum

chamber. After the vacuum level reached 10^{-3} Torr, dry nitrogen, dry oxygen, and wet nitrogen were introduced to the chamber for each device respectively. After the pressure level reached 20 Torr, $V_G = +3$ V was applied to each device for 180 s, and then the devices were left open circuit. MOKE hysteresis loops of these devices were taken again after the voltage applications. The results are shown in Figure 6.5. Inversion of hysteresis loop polarity was only observed in gas environment with water vapor and the hysteresis loops of the rest of the devices did not show observable changes. The critical role of water vapor in the gating process supports the water splitting and hydrogen injection mechanism[7]. This remarkable change in T_M, by >100 K, indicates that hydrogen gating can enable facile solid-state control of ferrimagnetic order and 180° switching of the net magnetization by tuning the relative magnitude of M_{Co} and M_{Gd} using a small gate voltage.

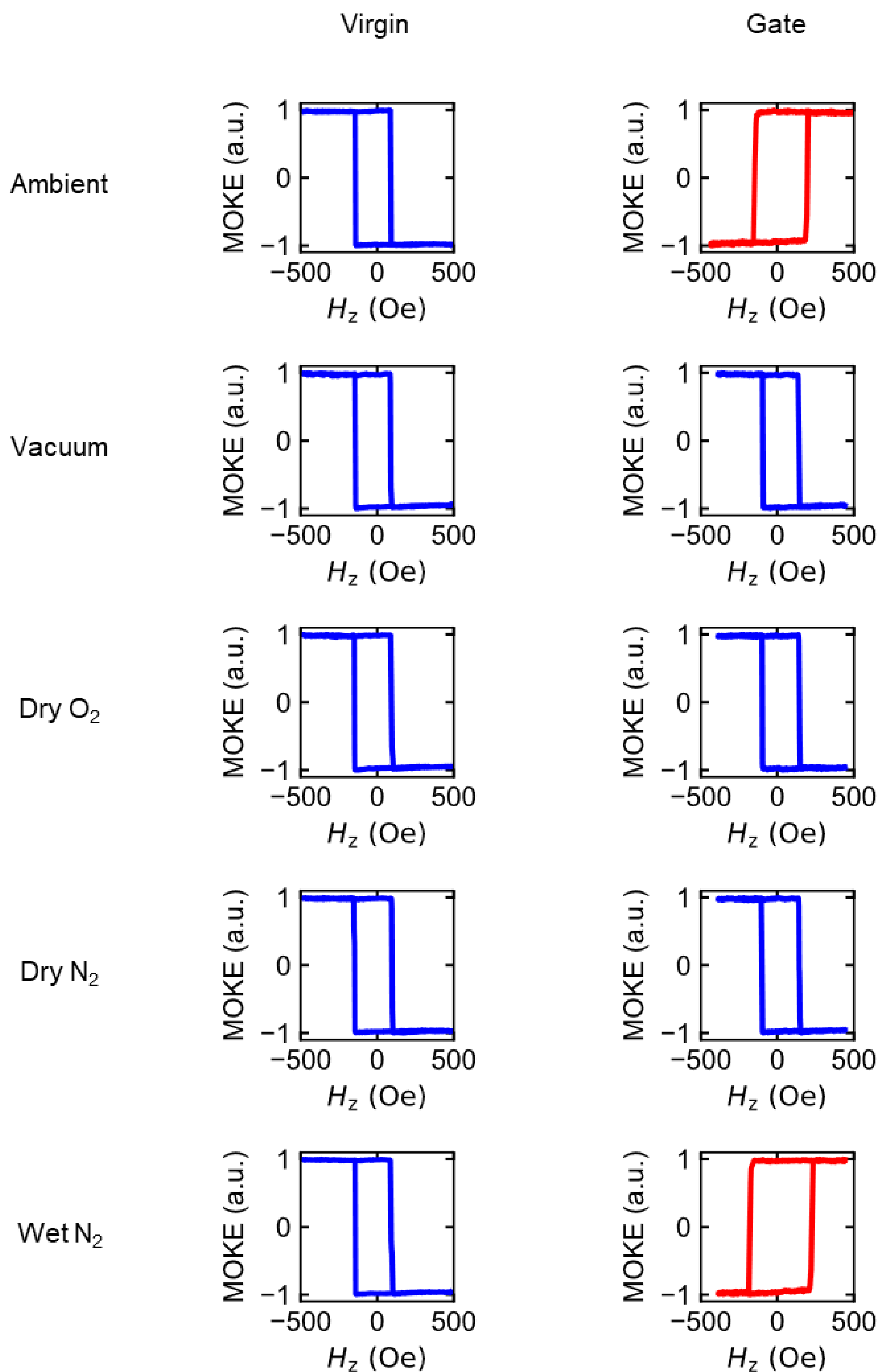

Figure 6.5. MOKE hysteresis loops before and after applying $V_G = +3$ V for 180 s under different gas environments

Figure 6.2f shows the coercivity, H_c, versus T before and after gating with $V_G = +2.5$ V. The divergence of H_c corresponds to the magnetization compensation temperature T_M, at which $|M_{Co}|=|M_{Gd}|$ and hence $M_s=0$. In the virgin state, $T_M \approx 330$ K, consistent with a Gd-dominated net magnetization at room temperature. After gating, T_M decreases to $\approx$220 K, such that the room-temperature magnetization is Co-dominated, which explains the MOKE polarity inversion in Figure 6.2d.

We note that the sign flip of MOKE hysteresis loop alone may not fully support that the dominant sublattice of GdCo was switched at room temperature, because the sign flip of the loop may come from the sign flip of Co sublattice moments, or from the change of the optical properties of the thin film stack such that the MOKE contrast flips. To study the origin of the sign flip, we carried out differential wide field MOKE measurements to show that we indeed switched the Co sublattice moment direction with respect to the total magnetization. The measurement sequence is shown in Figure 6.6. We cycle the gate voltage between +2.5V and -2.5V with 60s dwell time on each polarity. A few seconds before the gate voltage sign flipping, a +Hz pulse was applied to align the total magnetization to positive z direction, and wide field MOKE contrast before and after the field pulse was recorded and shown as insets of Figure 6.6.

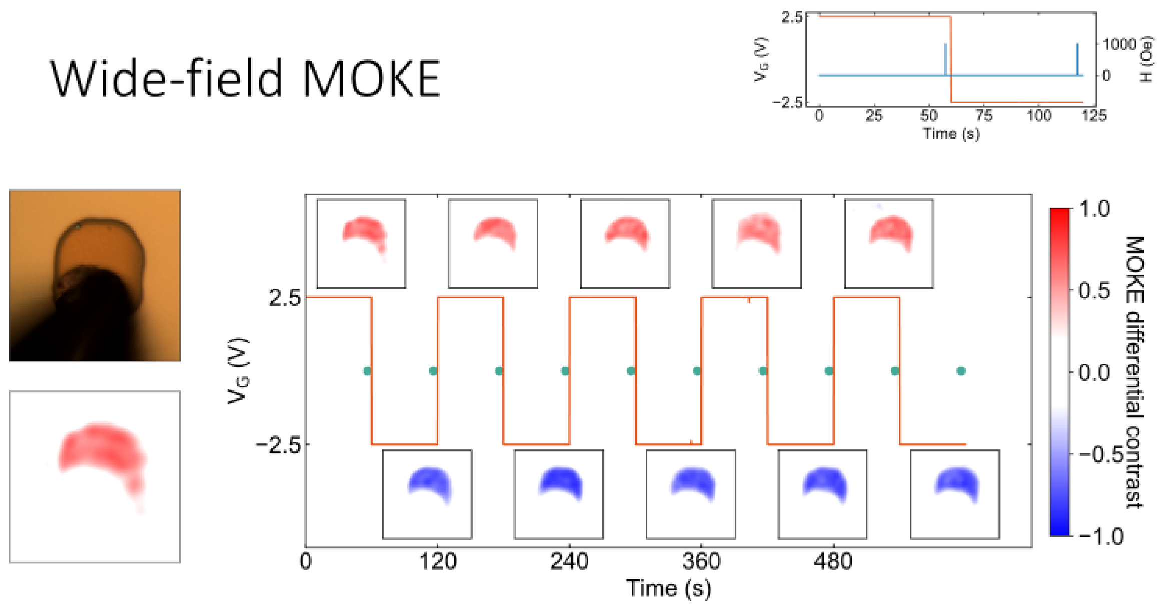

Figure 6.6. Differential wide-field MOKE images and experimental procedures to verify the origin of MOKE polarity flipping.

Because we observe MOKE contrast every time after the field pulse, the Co sublattice moment was flipped during the field pulse. The opposite sign of the MOKE contrast at positive and negative V_G corresponds to the two flipping events during a full positive and negative V_G cycle. We also rule out the effect of reflection intensity change by measuring the MOKE contrast when no field was applied, which was negligible because the optical change was plateaued after 60s at each direction. The results support that the origin of the sign flip of MOKE hysteresis loop is due to the toggling of the dominant sublattice. Such measurement protocol was extended below in the section on reversed domain generation.

6.3 *Ab initio* Modeling of Hydrogen-Enabled Switching of Ferrimagnetic Order

To provide mechanistic insight into the observed T_m gating by hydrogenation, we employed density functional theory (DFT) calculations using a crystalline $GdCo_2$ supercell as a model system (Figure 6.7a). Ab initio calculations reveal that the zero-temperature Gd magnetic moment is insensitive to hydrogenation due to the highly localized nature of the *f*-electrons, and the Co magnetic moment varies only slightly upon hydrogen loading, remaining in the range of 1.3-1.5 μ_B under all studied loading conditions. Since these changes are insufficient to explain switching of the dominant sublattice, we examined the effect of incorporated H on inter- and intra-lattice exchange interactions, which may affect the T-dependence of M_{Co} and M_{Gd}. Using a Heisenberg model, we find that the intersublattice exchange coupling constant $J_{Gd\text{-}Co}$ decreases drastically upon hydride formation, whereas the Co-Co exchange constant $J_{Co\text{-}Co}$ shows a more modest decrease (Figure 6.7b). Since Gd-Gd exchange coupling is weak, $J_{Gd\text{-}Co}$ is dominantly responsible for stabilizing M_{Gd} at finite temperature, and hence we attribute the experimentally-observed hydrogen-gated reduction of M_{Gd} relative to M_{Co} to a weakening of antiferromagnetic exchange coupling.

To confirm the effects of weakened antiferromagnetic exchange, we performed Monte-Carlo spin dynamics simulations as discussed in Section 6.1 to estimate M_{Gd} and M_{Co} at finite temperature as a function of the degree of hydrogen loading (Figure 6.7c). In accordance with prior work[140,141], $GdCo_2$ is Gd-dominated at room temperature, with a net magnetic moment of 2.8 μ_B/f.u. Hydrogen incorporation leads to a significant reduction of M_{Gd} at room temperature, while M_{Co} decreases less strongly. Although $GdCo_2H$ remains Gd-dominated, for $GdCo_2H_2$, the relative change in M_{Gd} and M_{Co} is found to be sufficient to switch the dominant sublattice at room temperature, as seen

in Figure 6.7c. These results point to hydrogen-gated modulation of $J_{Gd\text{-}Co}$ as the origin of the experimentally-observed shift in T_M.

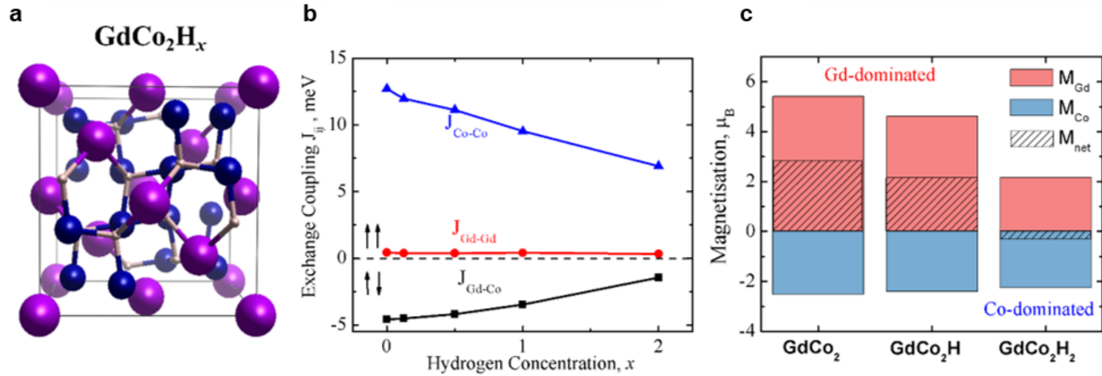

Figure 6.7. Ab initio calculations of the impact of hydrogen intercalation. a, Crystal structure of $GdCo_2H_x$ (C15 Laves phase) used as a model system. **b,** Evolution of exchange coupling constants upon $GdCo_2H_x$ hydrogenation obtained using DFT calculations. **c**, Sublattice and net magnetizations of $GdCo_2H_x$ at T= 300 K from spin dynamics modeling

6.4 Reversibility of Sublattice Gating and 180° Néel Vector Switching

We next examine the reversibility of sublattice switching and demonstrate 180° switching of the Néel vector, detected electrically in a standard Hall cross geometry (Figure 6.8a). Out-of-plane hysteresis loops were probed via the anomalous Hall effect (AHE) resistance (R_{AHE}) while V_G was applied to the gate electrode. Similarly to MOKE contrast, R_{AHE} arises primarily from Co[71,142], and hence V_G toggling of the dominant sublattice should manifest as an inversion of the AHE hysteresis loop. Figure 6.8b shows a time sequence of hysteresis loops acquired as V_G = +3 V was applied for 5 s starting in the Gd-dominated state, followed by V_G = -1.5 V for another 5 s. Positive bias causes H_c to first increase abruptly, as the GdCo is driven through compensation, and then to

decrease after the AHE loop inverts. Negative bias brings the system back through compensation to the Gd-dominated state. Since the transition is continuous, the degree of compensation can be precisely tuned by controlling the gate voltage and dwell time, providing analog accessibility to intermediate states with a wide range of H_c in both polarities.

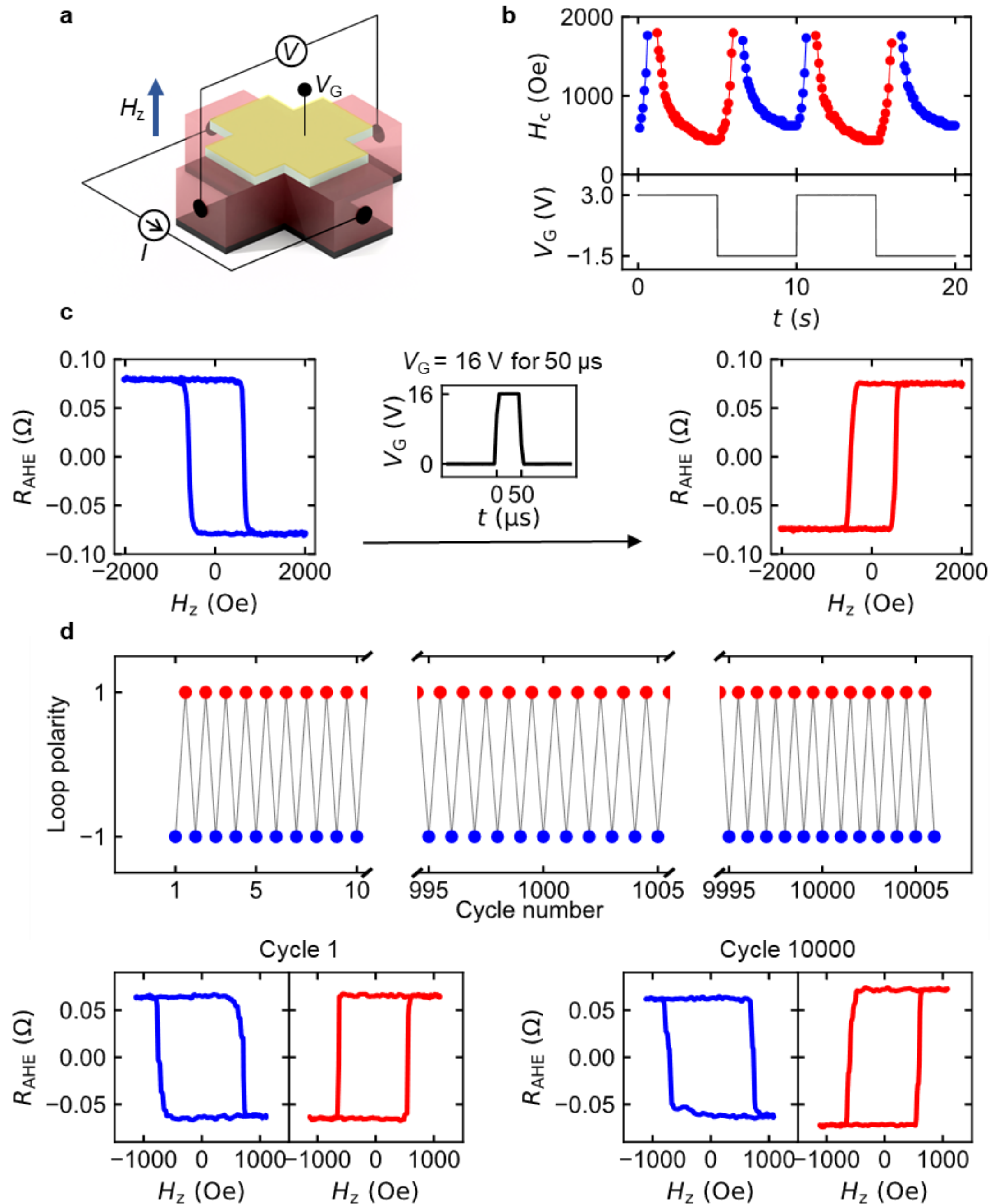

Figure 6.8. Electrical measurement of reversible toggling of the dominant sublattice with gate voltage. a, Schematic illustration of the device structure. The Pd protection layer on top of GdCo is omitted. **b,** Time sequence of the coercivity H_c of hysteresis loops acquired as V_G = +3.0 V was applied for 5 s starting in the Gd-dominated state, followed by V_G = -1.5 V for another 5 s. **c,** AHE hysteresis loops measured before (left) and after (right) a V_G pulse (+16 V, 50 μs) was applied. The V_G pulse waveform is shown in the middle. **d,** AHE hysteresis loop polarity versus cycle number, showing >10,000 reversible cycles. AHE hysteresis loops of device in Gd

dominated state (blue) and Co dominated state (red) at the 1st and 10,000th cycle are shown (bottom). No irreversible changes of the hysteresis loop are observed.

Figure 6.8d shows the AHE loop polarity as a function of cycle number as the device was cycled >10,000 times between Gd and Co-dominated states. Here, the voltage dwell time during each cycle was adjusted to set the device into states with equal H_c on either side of compensation. The AHE hysteresis loops measured at Cycles 1 and Cycle 10,000 are shown in Figure 6.8d. We find that although the time required for hydrogen loading/unloading increases with increased cycling as shown in Figure 6.9, the magnetic property switching is remarkably reversible, with no evidence of device wear out or irreversible magnetic property changes after an unprecedented degree of cycling.

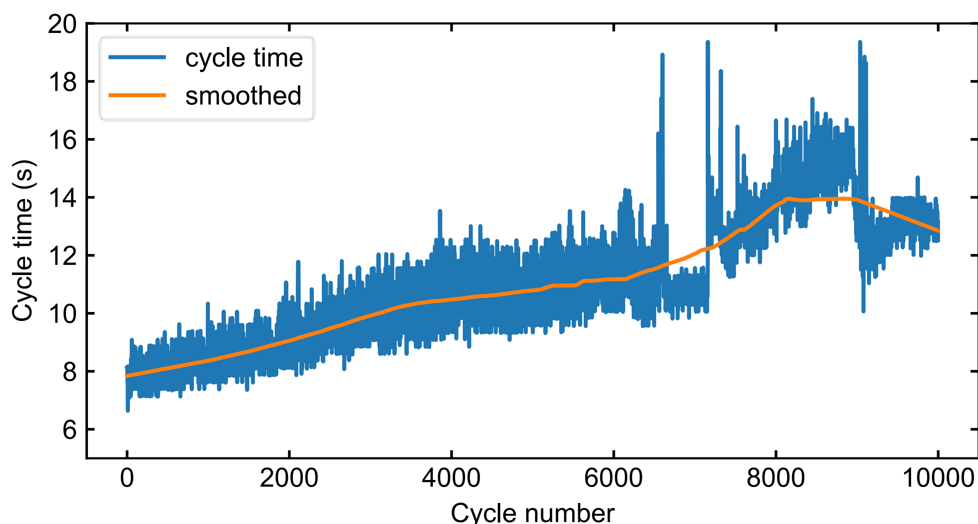

Figure 6.9. Cycle time as a function of cycle number when the device was cycled using V_G = +2.3 V and -0.5 V.

Figures 6.10a,b shows that in the presence of a static bias field, 180° Néel vector switching can be achieved through gate voltage control. For this Hall cross device, R_{AHE} is ~-0.1 Ω in the Gd-dominated state and ~0.1 Ω in the Co dominant state (Figure. 6.10a). For the switching experiment, a fixed +1000 Oe out-of-plane field was applied, while V_G was alternated between +2.8 V and -1.5 V. Figure 6.10b shows R_{AHE} and V_G versus time, where R_{AHE} alternates between -0.1 Ω and +0.1 Ω, showing 180° switching of the Néel vector of the ferrimagnetic order. Although an external field was used for convenience, a pinned stray field layer[143] could be readily integrated to permit field-free 180° switching by V_G alone.

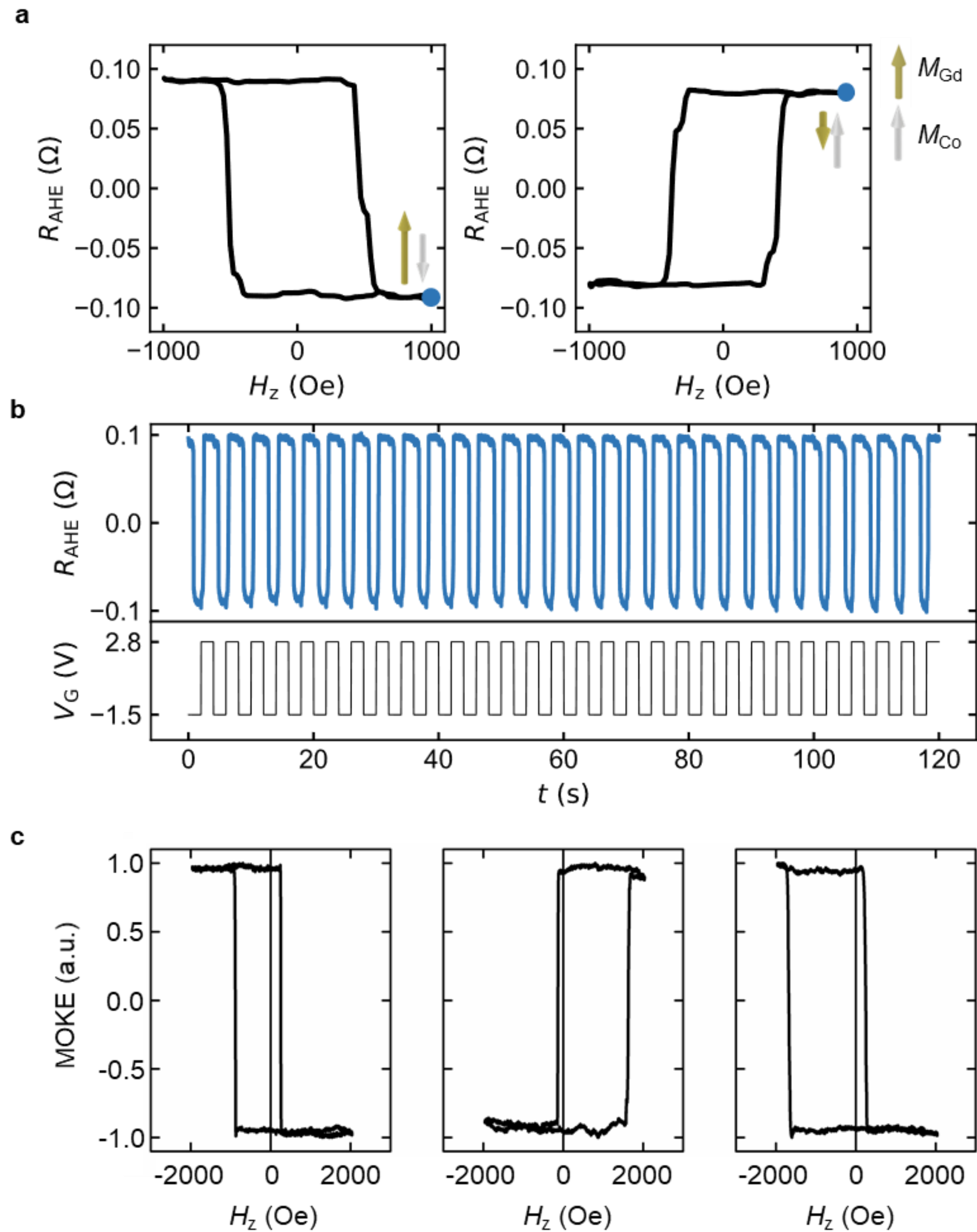

Figure 6.10. **180º switching of the Néel vector and the exchange bias field by gate voltage. a,** AHE hysteresis loops taken at Gd dominant state (left) and Co dominant state (right), controlled by applying V_G = -1.5 V and +2.8 V, respectively. **b,** R_{AHE} and V_G as a function of time showing reversible switching of the sublattice magnetizations. **c,** MOKE hysteresis loops of exchange biased GdCo as fabricated (left), after applying V_G = +2 V (middle), and subsequently application of $V_G < 0$ (right).

We have also grown a stack in which the GdCo layer is exchange-biased by an antiferromagnetic NiO layer as described in Section 6.1, in which we demonstrate voltage-gated toggling of the exchange bias field. In Figure 6.10c, the sample was grown with an out-of-plane bias field to achieve a negative out-of-plane exchange bias field of 330 Oe, in the Gd-dominated state. Applying a positive gate voltage of +2V for 3 mins switches the dominant sublattice, as evidenced by the vertical inversion of the loop, which is accompanied by an inversion of hysteresis loop shift direction along the field axis. This toggling of the exchange bias field can be attributed to a change in the direction of the net magnetization with respect to the pinned spins at the interface, and it is reversible under application of $V_G < 0$.

6.5 Fast Hydrogenation with Voltage Pulses

Fast toggling of dominant sublattice at room temperature can be achieved with larger V_G voltage application. The speed of the hydrogen loading is determined by water splitting reaction at the top electrode, proton migration through the GdO_x layer, and hydrogen incorporation into the bottom layer. All these procedures are expected to be faster at larger positive V_G. Figure 6.11. shows the H_c as a function of time as we apply +7 V 5 ms V_G pulses. When the pulse was off, a -0.5 V V_G was applied to reverse the hydrogen loading. Figure 6.11 shows that the dominant sublattice can be toggled by just one pulse.

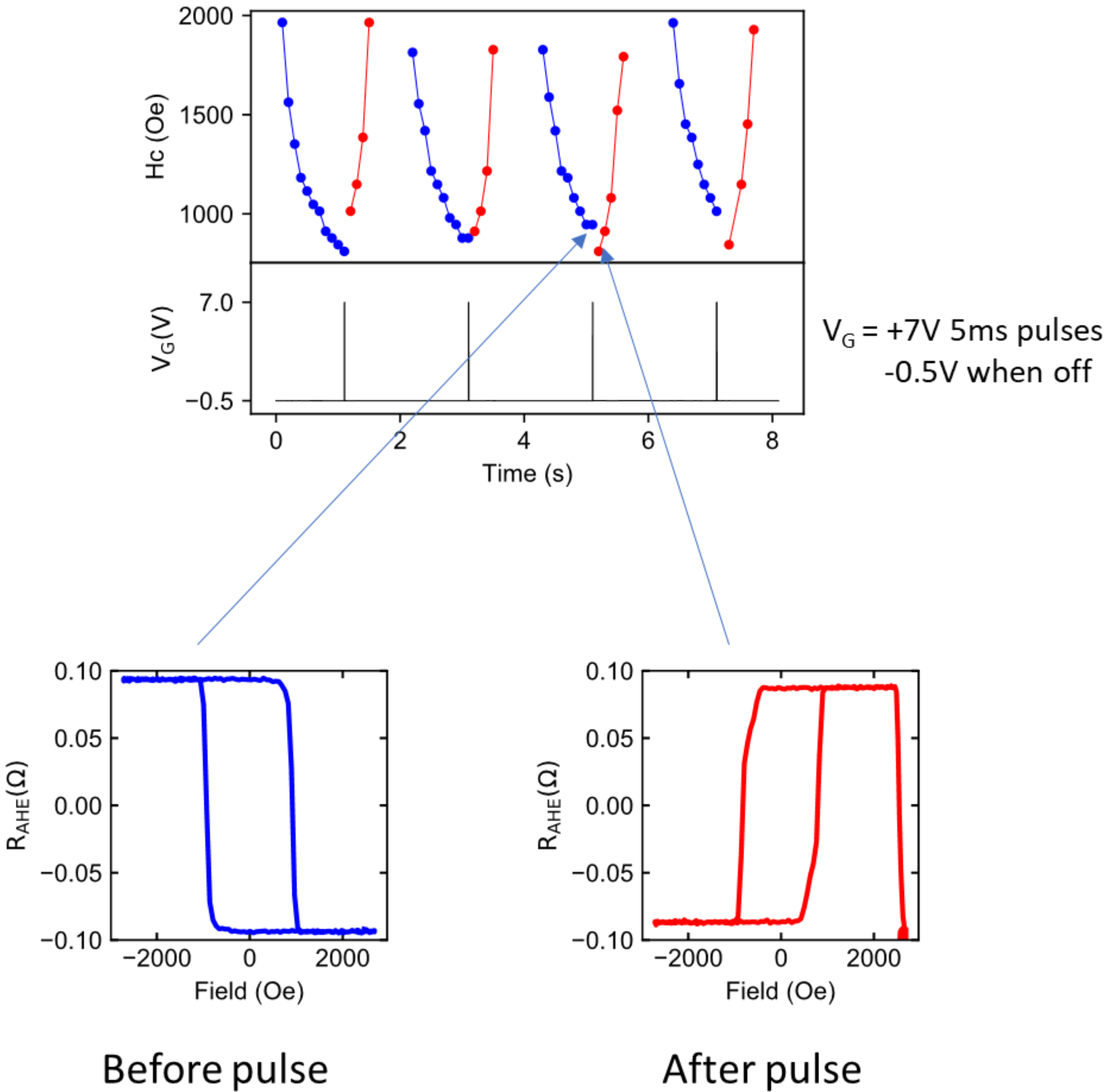

Figure 6.11. ***H_c* and *V_G* as a function of time showing that a single 5 ms +7 V *V_G* pulse can switch the dominant sublattice at room temperature.**

Figure 6.12 plots H_z, V_G, and the AHE signal as a function of time in vicinity of the V_G pulse. It shows that the AHE signal switching was delayed <10 ms after the pulse. The delay could be attributed to the hydrogen diffusion rate from Pd layer into GdCo layer, or be attributed to the domain wall propagation time. Further study on the effect of H_z and V_G on the delay time should reveal the cause of the delay.

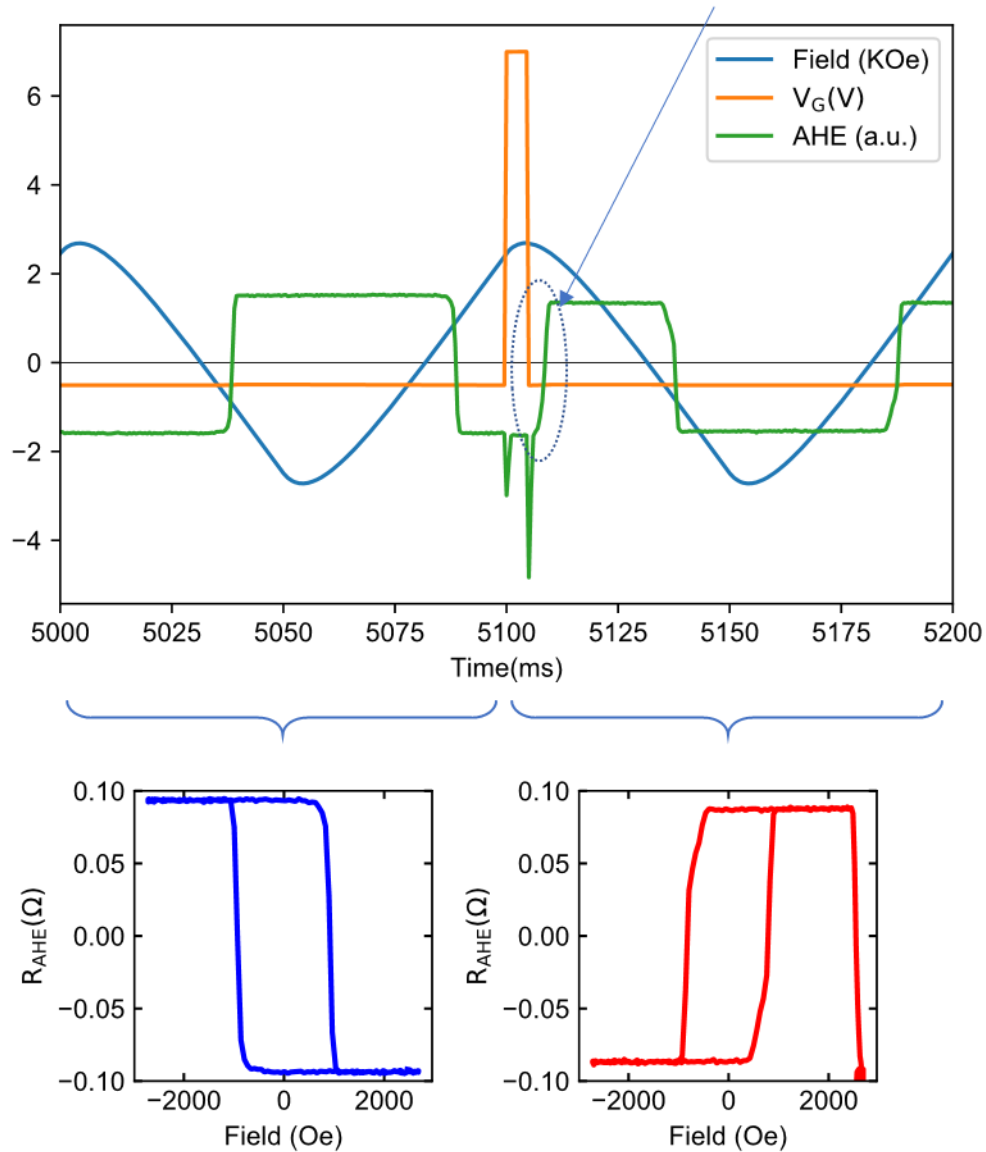

Figure 6.12. H_z, V_G and AHE signal as a function of time in the vicinity of the V_G pulse showing a delay of Co moment switching after the V_G pulse.

Nonetheless, by further increasing the amplitude of the V_G pulse, we show that the time required to toggle the dominant sublattice at room temperature can be substantially shorted. We examined a device started in the Gd-dominated state, and a 50 μs long pulse with $V_G = +16$ V V_G was applied, after which the hysteresis loop inverted. This is the fastest magneto-ionic switching reported to

date, and it is expected that even faster switching should be accessible with higher V_G and a thinner GdO_x layer so that the electric field becomes higher.

6.6 Reversed Domain and Skyrmion Generation in Racetrack Devices

The localized nature of the hydrogen gating effect also enables applications such as reversed domain and skyrmion generators in racetrack-like devices, as we demonstrate in Fig. 6.13. The reversed domain generator is based on a Ta(3 nm)/Pt(3 nm)/GdCo(6 nm)/Pd(6 nm)/GdO_x(30 nm) film patterned into a domain wall track with a rectangular Au(3nm) gate electrode, as shown in Figure 6.13a. The asymmetric heavy metal layers beneath and above GdCo give rise to a Dzyaloshinskii–Moriya interaction (DMI) and current-induced spin-orbit torque (SOT)[60,144], stabilizing Néel domain walls that are readily displaced by current. To generate a reversed domain in the gate region (Figure 6.13a), the film was first initialized with a positive out-of-plane field pulse, and then $V_G = +2.5$ V was applied for 30 s to switch the gated region from Gd-dominated to Co-dominated. A positive out-of-plane field pulse was then used to locally switch the Néel vector under the gate, after which $V_G = -1$ V was applied for 10 s to return the gated region to a Gd dominated state.

Figure 6.13b shows a sequence of differential MOKE contrast images as the resulting reversed ferrimagnetic domain was displaced along the track by longitudinal current pulses. Both up–down and down–up domain walls move along the current flow direction, consistent with SOT-driven left-handed Néel domain walls[145]. The result demonstrates that voltage gating in conjunction with a global out of plane field can be used to write a reversed domain in a defined region, which can

be subsequently shifted by current along a racetrack. The out-of-plane field can potentially be replaced with a localized pinned stray field layer to remove the need for an external field.

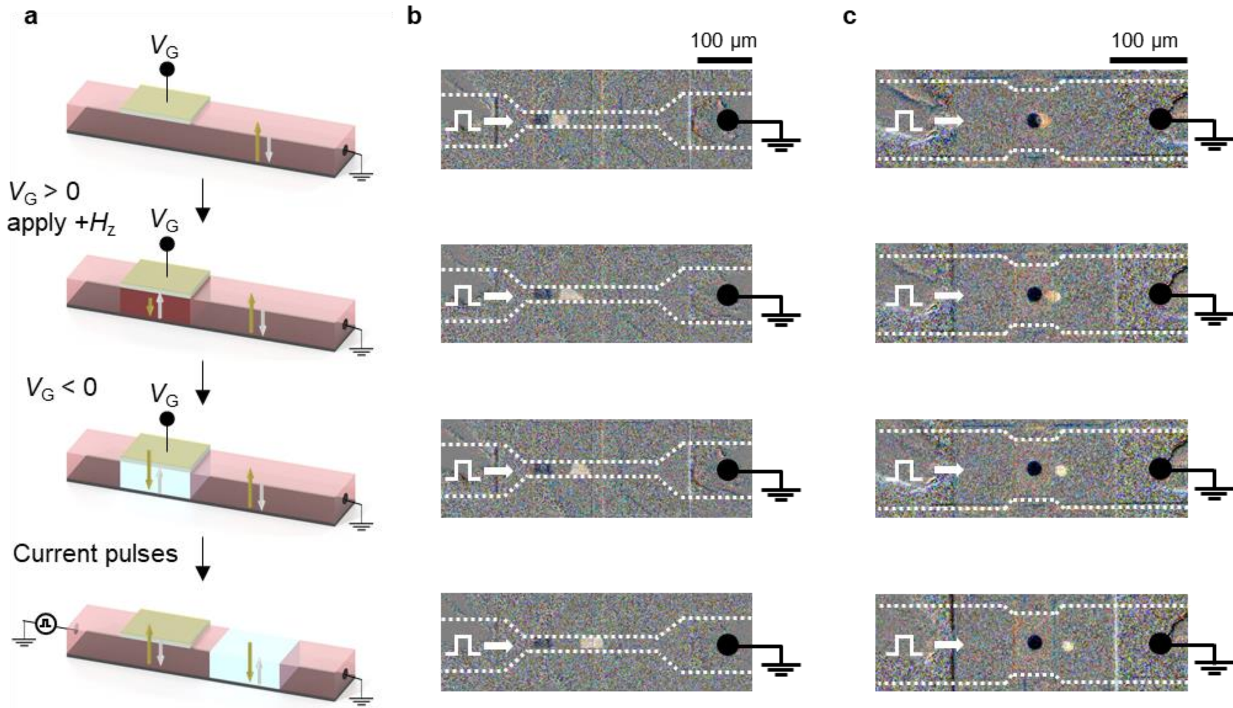

Figure 6.13. Reversed domain generator based on GdCo voltage gating. a, Schematic illustration of device structure and operation of the reversed domain generator. The Pd protection layer on top of GdCo is omitted. **b,** Sequence of wide field MOKE contrast images showing the movement of the generated reversed domain. **c,** Sequence of wide field MOKE contrast images showing the movement of the generated bubble skyrmion.

To further demonstrate the versatility of this approach, we also fabricated skyrmion generators with a similar structure to the reversed domain generator, with the addition of a Al_2O_3 hydrogen blocking layer[146] between the GdO_x and Pd layers as described in Section 6.1. The Al_2O_3 layer was patterned with a circular hole beneath the rectangular gate, so as to limit the region in which hydrogen loading occurs. Following the same procedure as for the reversed domain generators, a

circular reversed domain in the middle of a racetrack was nucleated and shifted by current, as shown in Figure 6.13c. The direction of motion indicates that the domain is a left-handed Néel bubble skyrmion, which can be shifted bidirectionally by reversing the current polarity. Figure 6.14 shows the MOKE contrast images of the skyrmion generator after the initiation sequence described in the main text, after each of a series of current pulses injected laterally while holding a small out-of-plane stabilizing field. The current pulses were injected from right to left, which is reversed comparing to the current injected in Fig 6.13 in the main text, and the skyrmion bubble also moved towards the reversed direction as expected.

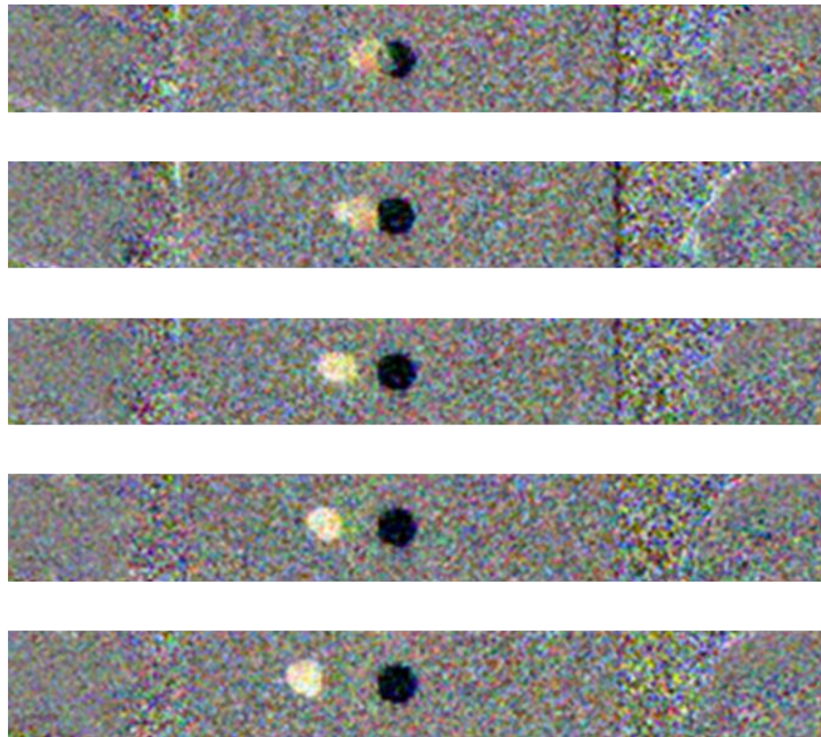

Figure 6.14. Sequence of wide field MOKE contrast images showing the movement of the generated skyrmion bubbles with lateral current pulses injected from right to left.

6.7 Voltage Control of Magnetic Anisotropy of Bulk PMA Films

In addition to the control of the relative size of the magnetic sublattice moment, gate voltage induced hydrogen loading/unloading also enables the control of magnetic anisotropy of the GdCo film. We measured the AHE hysteresis loop with either an out-of-plane field or an in-plane field of the devices before and after V_G application and the results are shown in Figure 6.15.

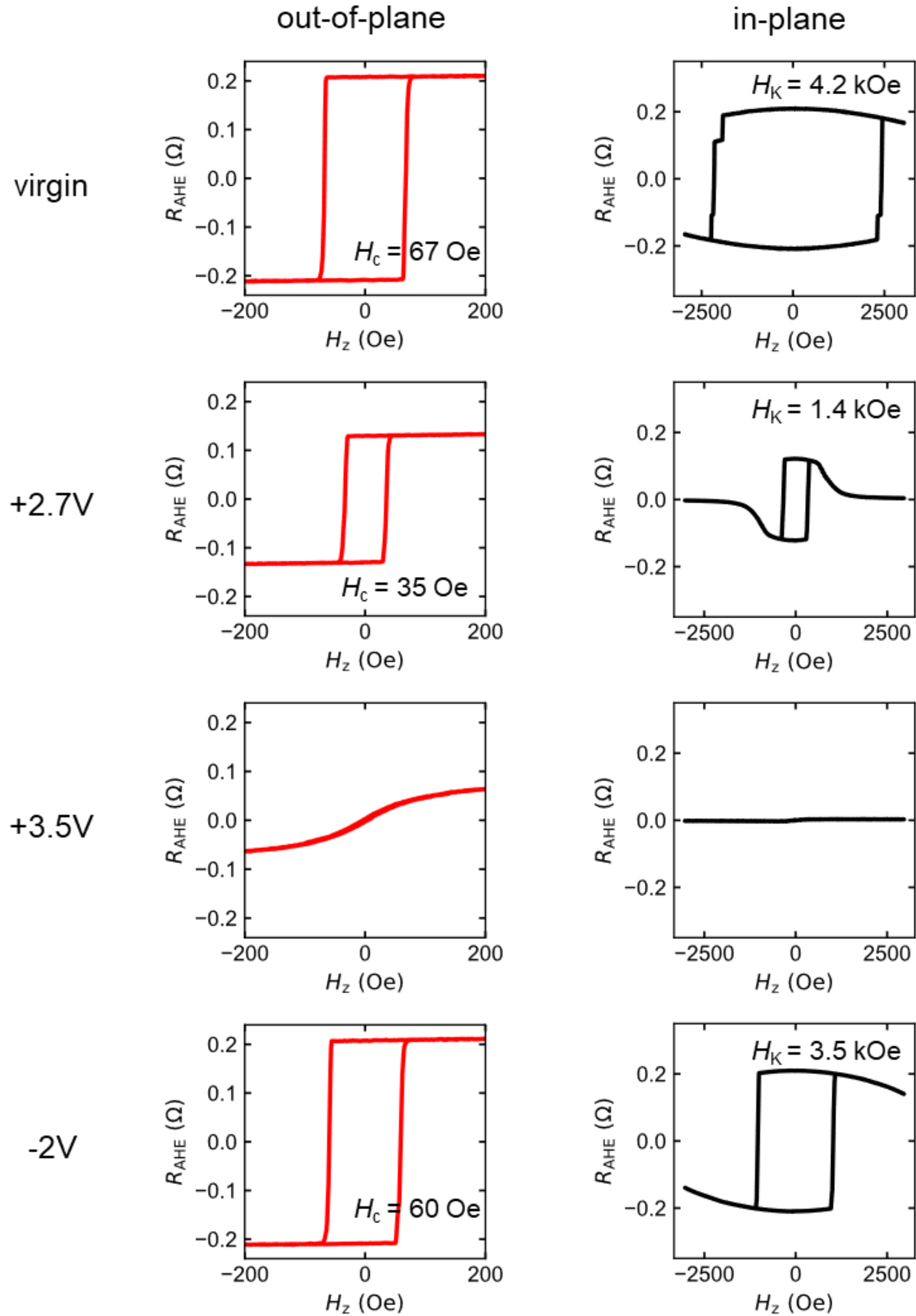

Figure 6.15. AHE hysteresis loops measured with out-of-plane field and in-plane field as fabricated, when the gate voltage was held at different levels, and when a negative gate voltage was applied to reverse the hydrogen loading. The H_c and H_K values are labeled inside the hysteresis loops.

As fabricated, the GdCo layer shows PMA characterized by a square hysteresis loop with $H_c \approx 67$ Oe. The polarity of the AHE hysteresis loop indicate that the device was Co dominant at room temperature. We extract the coercive field (H_k) of the GdCo by fitting the top and bottom of the hysteresis loop to Stoner W model. As fabricate, H_k was around 4.2 kOe. Then, $V_G = 2.7$ V was applied. After 3 min, the hysteresis loops were measured while the V_G was holding at 2.7 V. As shown in the figure, Hc becomes 35 Oe, and $H_k \approx 1.4$ kOe showing a great reduction of the H_k. Then a +3.5V V_G was applied for 3mins, and the hysteresis loop measurements was carried out again. The AHE hysteresis loop shows that the PMA was turned off. Finally, $V_G = -2$ V was applied, and the film regained PMA, and H_c and H_k recovered partially. The results indicate that the anisotropy of ferrimagnets can be reversibly controlled by a gate voltage in such structure. Previous works on voltage controlled magnetic anisotropy usually focus on controlling interfacial PMA. It is desirable for data storage applications to use magnetic layers with bulk PMA so that the bit size can be shrink down without losing the date retention as the anisotropy energy of bulk PMA film scales with the thickness. The work paves ways to magnetic data storage with improved power efficiency and high scalability.

6.8 Conclusions

We have shown that the dominant sublattice of a ferrimagnet can be switched reversibly by a gate voltage in an all solid-state structure. The switching originates from hydrogen injection into GdCo sourced from H_2O hydrolysis in ambient, reducing M_{Gd} more than M_{Co} and therefore reducing T_M. We show that T_M of GdCo can be shifted by > 100 °C, and at room temperature the MOKE contrast and AHE loop polarity can be switched reversibly. The switching showed remarkable cyclability of > 10,000 cycles, and allows for analog accessibility to intermediate states, making it of utility for realizing a spintronic synapse[147]. The approach also allows for 180° switching of the Néel vector with a fixed bias field, which could be readily replaced by a local stray field source for device integration. Because the switching is restricted to only the gate

region, it also allows for reversed domain and skyrmion generation on racetrack-like devices, revealing potential applications of the approach in solid-state magnetic data storage and logic. We expect that the approach is not restricted to GdCo, but should be applicable to the larger family of RE-TM magnets. A wide range of properties and phenomenon can be gated such as spin dynamics and spin texture characteristics. Finally, the switching of MOKE contrast in a localized region may also enable a new type of magneto-optical switching, with potential application of an energy efficient and high pixel density magneto-optical spatial light modulator.

Chapter 7 Summary and Outlook

7.1 Summary

In summary, we have significantly extended the scope of voltage gated material properties using solid-state ionic motion and electrochemical reactions. We demonstrate that a simple structure of a solid-state electrolyte on top of a metallic layer followed by a thin layer of top electrode enables control of a wide range of material properties including electrical and optical properties and enables the control of ferrimagnetic order. The findings also extend the scope of controlling interfacial properties to also include control of bulk material properties.

For the voltage control of electrical properties, we focused on controlling the resistivity of a thin film conductive channel by demonstrating a three-terminal resistive switch based on a metal-redox switch. The device operates by oxidizing a metallic material and reducing the corresponding oxide back to metal with all solid-state operation. Resistance change can be observed at room temperature. By reducing the thickness of the wire layer, a switching ratio of ~10^3 was obtained. The reversible non-volatile redox reaction between metal and metal oxide provides a means of post-fabrication control of solid-state material composition and properties. Potential material choices and device designs are discussed for achieving better switching performance. This type of three-terminal switch may find applications in neuromorphic computing and multilevel data storage, as well as applications that require a large resistivity change and those involving controlling a relatively large current.

For voltage control of optical properties, we demonstrated all-solid-state thin film devices with electrochemically switchable optical properties through hydrogen loading/unloading using a simple gate oxide. Reflectance, transmittance and plasmonic response gating over a wide range can be achieved by reversibly pumping hydrogen into and out of the system, based on electrocatalysis at the electrode/air interface. The active oxide can be made as thin as 10 nm so that the optical modulation can be highly localized, and high switching speeds can be achieved. The versatile approach has potential applications in optical modulators and displays. In addition, the ultra-thin solid-state stack allows the use of flexible substrates and realization of ultrathin pixels whose lateral dimensions can hence be scaled to deep sub-wavelength for high-resolution optical and holographic display applications.

For voltage control of ferrimagnetic order, we demonstrate that the dominant sublattice of a ferrimagnet can be switched reversibly by a gate voltage in an all solid-state structure. The switching originates from hydrogen injection into GdCo sourced from H_2O hydrolysis in ambient, reducing M_{Gd} more than M_{Co} and therefore reducing T_M. We show that T_M of GdCo can be shifted by > 100 °C. The switching showed remarkable cyclability of > 10,000 cycles with fast switching with 50 μs pulses, and allows for analog accessibility to intermediate states. The approach also allows for 180° switching of the Néel vector with a fixed bias field, allows for reversed domain and skyrmion generation on racetrack-like devices, revealing potential applications of the approach in solid-state magnetic data storage and logic. We expect that the approach is not restricted to GdCo, but should be applicable to the larger family of RE-TM magnets. A wide range of properties and phenomenon can be gated such as spin dynamics and spin texture characteristics. Finally, the switching of MOKE contrast in a localized region may also enable a new type of

magneto-optical switching, with potential application of an energy efficient and high pixel density magneto-optical spatial light modulator.

7.2 Outlook

In this section, we briefly mention possible future research topics as the outlook of the thesis. Additional study is necessary to better understand the underlying mechanisms as well as to better engineer devices for better performance. In addition, there are other properties that can potentially be controlled using the same approach.

7.2.1 High Resolution Optical Modulator with Applications of Ultra-High Pixel Density Displays or Holographic Displays

The unique advantage of the method to control material properties studied in this thesis is the localization of the property change. Because the devices consist of thin films with thickness down to ~10 nm that are compatible with semiconductor manufacturing processes, the approach is expected to allow for localized control with high spatial resolution. We expect that the capability to control the optical properties reversibly at subwavelength scale can enable unique applications such as high pixel density displays, counterfeit printing, reconfigurable metasurfaces, and dynamic holographic displays with wide viewing angle.

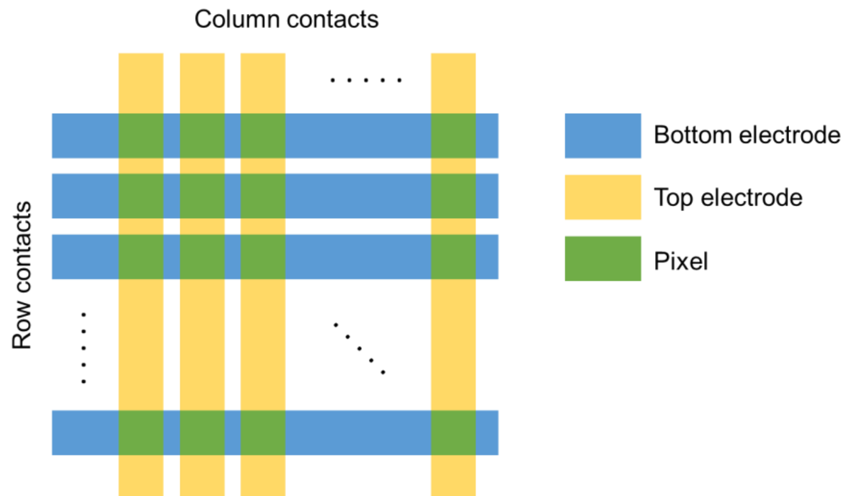

Figure 7.1. Passive addressing of an array of voltage-controlled devices.

Because the devices have a threshold behavior defined by the water splitting potential and the switching speed depends non-linearly on the gate voltage, it also has the potential to use passive addressing to control an array of devices to form a matrix. Figure 7.1 illustrates the layout of a passively addressed array of voltage-controlled devices.

7.2.2 Using SiO_2 and Spin-Coated Hydrogen Silsesquioxane (HSQ) as the Solid Electrolyte for Proton Conduction

SiO_2 is one of the most common material used and is highly abundant. Preliminary results show that it is possible to use SiO_2 as the solid-state electrolyte layer to conduct protons. Optimizing and exploiting the use of SiO_2 may enable devices that are easily fabricated with low cost. It is also worth exploring the use of spin coated HSQ as a way to make large area device at low cost.

7.2.3 Controlled Properties as Quantitative Probes for Nanoionics

The device structures used in the thesis for controlling electric, optical properties and ferrimagnetic order offer analog readout of the amount of hydrogen loading of the device. For the lateral resistive switching devices, the resistance is an analog reading of the oxidation of the conductive channel, for voltage control of ferrimagnetic order, the coercive field is a quantity that can be used as a quantitative measurement of the total magnetic moment, which relates to the hydrogen loading, and the reflectivity for voltage controlled optical devices also changes in an analog way that relates to the hydrogen loading and profile of the device. We expect that the controlled properties can be quantitively characterized relatively easily, therefore offering a way to quantitatively study solid-state ionic motion and electrochemical reactions. Further study is needed to correlate the property change and the amount of composition change as well as the ion concentration profile.

7.2.4 Voltage Control of Spin–Orbit Torque (SOT) Switching Threshold for Alternative Implementation of Reversed Domain Generators

Chapter 6 reveals that the bulk PMA can be controlled by applying a gate voltage. The control of the magnetic anisotropy energy may lead to different current threshold for SOT switching. Further study is needed to characterize the magnetic anisotropy energy and the effective spin Hall angle as a function of hydrogen load. Measurement of the critical switching current at a fixed applied field at different gating state can be carried out. If a reversible change of the critical switching current can be achieved, devices with localized reversed domain generator can be realized and a new scheme of magnetic bit writing can be achieved.

7.2.5 Voltage Control of More Material Properties

Using solid-state ionic motion and electrochemical reactions, one can control the composition of thin film material layers. Since a wide variety of properties are sensitive to such hydrogen loading or oxidation, the voltage control of materials properties should enable much greater functionalities than can be covered in this thesis. In addition to the electrical, optical and magnetic properties discussed in the thesis, there are also a wide range of other materials properties that depend on materials composition, such as thermal conductivity, modulus, strain, and chemical/catalytic activity. For example, the change from Mg to MgH_2 when loaded with hydrogen is accompanied by a 40% volume expansion. Such a large lattice parameter change may enable a voltage-controlled strain device that functions at room temperature as shown in Figure 7.2.

Figure 7.2. Gate voltage controlled hydrogen loading/unloading device fabricated on a chip with a 200 nm thick 0.5 mm x 0.5 mm square Si_3N_4 window showing reversible deformation with gate voltage application.

Due to the broadness of material properties that can be modulated with a change in composition, we expect exciting developments of voltage-controlled material properties with solid-state ionics in the near future.

References

1. Yang, P. & Tarascon, J. M. Towards systems materials engineering. *Nat. Mater.* **11**, 560–563 (2012).

2. Yang, J. J., Strukov, D. B. & Stewart, D. R. Memristive devices for computing. *Nat. Nanotechnol.* **8**, 13–24 (2013).

3. Christodoulou, C.G.; Tawk, Y.; Lane, S.A.; Erwin, S. R. Reconfigurable antennas for wireless and space applications. *Proc. IEEE* **100**, 2250–2261 (2012).

4. Dickson, W., Wurtz, G. a., Evans, P. R., Pollard, R. J. & Zayats, A. V. Electronically controlled surface plasmon dispersion and optical transmission through metallic hole arrays using liquid crystal. *Nano Lett.* **8**, 281–286 (2008).

5. Bauer, U. Voltage programmable materials. (Massachusetts Institute of Technology, 2014).

6. Bauer, U. *et al.* Magneto-ionic control of interfacial magnetism. *Nat. Mater.* **14**, 174–181 (2014).

7. Tan, A. J. *et al.* Magneto-ionic control of magnetism using a solid-state proton pump. *Nat. Mater.* **18**, 35–41 (2019).

8. Tan, A. J. *et al.* Hydration of gadolinium oxide (gdox) and its effect on voltage-induced co oxidation in a pt/co/gdox/au heterostructure. *Phys. Rev. Mater.* **3**, 064408 (2019).

9. Tan, A. J. Dynamic modulation of material properties by solid state proton gating. (Massachusetts Institute of Technology, 2019).

10. Emori, S., Bauer, U., Woo, S. & Beach, G. S. D. Large voltage-induced modification of

spin-orbit torques in pt/co/gdox. *Appl. Phys. Lett.* **105**, 222401 (2014).

11. Bauer, U., Emori, S. & Beach, G. S. D. Voltage-controlled domain wall traps in ferromagnetic nanowires. *Nat. Nanotechnol.* **8**, 411–6 (2013).

12. Bi, C. *et al.* Reversible control of co magnetism by voltage-induced oxidation. *Phys. Rev. Lett.* **113**, 1–5 (2014).

13. Maruyama, T. *et al.* Large voltage-induced magnetic anisotropy change in a few atomic layers of iron. *Nat. Nanotechnol.* **4**, 158–161 (2009).

14. MacLeod, H. A. *Thin-Film Optical Filters*. *Thin-Film Optical Filters* (2001). doi:10.1201/9781420033236

15. Stavenga, D. G., Leertouwer, H. L. & Wilts, B. D. Coloration principles of nymphaline butterflies - thin films, melanin, ommochromes and wing scale stacking. *J. Exp. Biol.* **217**, 2171–2180 (2014).

16. Burg, S. L. & Parnell, A. J. Self-assembling structural colour in nature. *J. Phys. Condens. Matter* **30**, (2018).

17. Stavenga, D. G. *et al.* Classical lepidopteran wing scale colouration in the giant butterfly-moth paysandisia archon. *PeerJ* **2018**, 1–22 (2018).

18. Van Der Kooi, C. J., Elzenga, J. T. M., Dijksterhuis, J. & Stavenga, D. G. Functional optics of glossy buttercup flowers. *J. R. Soc. Interface* **14**, (2017).

19. Heavens, O. S. *Optical Properties of Thin Solid Films*. (Dover Publications, Inc., 1991).

20. Byrnes, S. J. Multilayer optical calculations. 1–20 (2016).

21. Palik, E. D. *Handbook of Optical Constants of Solids*. (Academic Press, 1985).

22. Rodríguez-de Marcos, L. V., Larruquert, J. I., Méndez, J. A. & Aznárez, J. A. Self-consistent optical constants of sio_2 and ta_2o_5 films. *Opt. Mater. Express* **6**, 3622 (2016).

23. Pezzi, L., Palermo, G. & Umeton, C. *Plasmonics : A Theoretical Background*. **2**, (1968).

24. Naik, G. V., Shalaev, V. M. & Boltasseva, A. Alternative plasmonic materials: beyond gold and silver. *Adv. Mater.* **25**, 3264–3294 (2013).

25. Barnes, W. L., Dereux, A. & Ebbesen, T. W. Surface plasmon subwavelength optics. *Nature* **424**, 824–830 (2003).

26. Willets, K. A. & Van Duyne, R. P. Localized surface plasmon resonance spectroscopy and sensing. *Annu. Rev. Phys. Chem.* **58**, 267–297 (2007).

27. Haes, A. J., Haynes, C. L., Mcfarland, A. D. & Schatz, G. C. Plasmonic materials for surface-enhanced sensing and spectroscopy. **30**, (2005).

28. Ozbay, E. Plasmonics: merging photonics and electronics at nanoscale dimensions. *Science* **311**, 189–193 (2006).

29. Ellenbogen, T., Seo, K. & Crozier, K. B. Chromatic plasmonic polarizers for active visible color filtering and polarimetry. *Nano Lett.* **12**, 1026–1031 (2012).

30. Kumar, K. *et al.* Printing colour at the optical diffraction limit. *Nat. Nanotechnol.* **7**, 557–561 (2012).

31. Kristensen, A. *et al.* Plasmonic colour generation. *Nat. Rev. Mater.* **2**, 16088 (2016).

32. Kawamoto, H. The history of liquid-crystal displays. *Proc. IEEE* **90**, 460–500 (2002).

33. Mortimer, R. J., Rosseinsky, D. R. & Monk, P. M. S. *Electrochromic Materials and Devices: Present and Future*. *Electrochromic Materials and Devices* **77**, (Wiley-VCH Verlag GmbH & Co. KGaA, 2013).

34. Richardson, T. J. *et al.* Switchable mirrors based on nickel-magnesium films. *Appl. Phys. Lett.* **78**, 3047–3049 (2001).

35. Wang, H., Li, H., Wang, Y., Xu, S. & Xu, W. A voltage-controlled silver nanograting device for dynamic modulation of transmitted light based on the surface plasmon polariton effect. *Nanoscale* **8**, 4650–4656 (2016).

36. Tarumi, K., Bremer, M. & Geelhaar, T. Recent liquid crystal material development for active matrix displays. (1997).

37. Xu, T. *et al.* High-contrast and fast electrochromic switching enabled by plasmonics. *Nat. Commun.* **7**, 10479 (2016).

38. Molten, P. H. L., Kremers, M. & Griessen, R. Optical switching of y-hydride thin film electrodes: a remarkable electrochromic phenomenon. *J. Electrochem. Soc.* **143**, 3348–3353 (1996).

39. Gillaspie, D. T., Tenent, R. C. & Dillon, A. C. Metal-oxide films for electrochromic applications: present technology and future directions. *J. Mater. Chem.* **20**, 9585 (2010).

40. Ríos, C., Hosseini, P., Taylor, R. A. & Bhaskaran, H. Color depth modulation and resolution in phase-change material nanodisplays. *Adv. Mater.* **28**, 4720–4726 (2016).

41. Hosseini, P., Wright, C. D. & Bhaskaran, H. An optoelectronic framework enabled by low-dimensional phase-change films. *Nature* **511**, 206–211 (2014).

42. Wuttig, M., Bhaskaran, H. & Taubner, T. Phase-change materials for non-volatile photonic applications. *Nat. Photonics* **11**, 465–476 (2017).

43. Huiberts, J. N. *et al.* Yttrium and lanthanum hydride films with switchable optical properties. *Nature* **380**, 231–234 (1996).

44. den Broeder, F. J. a *et al.* Visualization of hydrogen migration in solids using switchable mirrors. *Nature* **394**, 656–658 (1998).

45. Ngene, P. *et al.* Seeing hydrogen in colors: low-cost and highly sensitive eye readable hydrogen detectors. *Adv. Funct. Mater.* **24**, 2374–2382 (2014).

46. Chen, Y. *et al.* Dynamic color displays using stepwise cavity resonators. *Nano Lett.* **17**, 5555–5560 (2017).

47. Tittl, A. *et al.* Palladium-based plasmonic perfect absorber in the visible wavelength range and its application to hydrogen sensing. *Nano Lett.* **11**, 4366–4369 (2011).

48. Sterl, F. *et al.* Magnesium as novel material for active plasmonics in the visible wavelength range. *Nano Lett.* **15**, 7949–7955 (2015).

49. Zhu, X., Vannahme, C., Højlund-Nielsen, E., Mortensen, N. A. & Kristensen, A. Plasmonic colour laser printing. *Nat. Nanotechnol.* **11**, 1–6 (2015).

50. Duan, X., Kamin, S. & Liu, N. Dynamic plasmonic colour display. *Nat. Commun.* **8**, 14606 (2017).

51. Li, J. *et al.* Addressable metasurfaces for dynamic holography and optical information encryption. *Sci. Adv.* **4**, eaar6768 (2018).

52. Shao, L., Zhuo, X. & Wang, J. Advanced plasmonic materials for dynamic color display.

Adv. Mater. **30**, 1–18 (2018).

53. Duan, X., Kamin, S., Sterl, F., Giessen, H. & Liu, N. Hydrogen-regulated chiral nanoplasmonics. *Nano Lett.* **16**, 1462–1466 (2016).

54. Zheludev, N. I. Obtaining optical properties on demand. *Science* **348**, 973–974 (2015).

55. O'Handley, R. C. *Modern Magnetic Materials: Principles and Applications*. (Wiley-Interscience, 1999).

56. Tannous, C. & Gieraltowski, J. The stoner-wohlfarth model of ferromagnetism. *Eur. J. Phys.* **29**, 475–487 (2008).

57. Blundell, S. *Magnetism in Condensed Matter*. (Oxford University Press, 2001).

58. Radu, I. *et al.* Transient ferromagnetic-like state mediating ultrafast reversal of antiferromagnetically coupled spins. *Nature* **472**, 205–209 (2011).

59. Imagawa, T., Narishige, S. & Hanazono, M. Magnetic properties of co-based amorphous films. *IEEE Transl. J. Magn. Japan* **2**, 471–472 (1987).

60. Caretta, L. *et al.* Fast current-driven domain walls and small skyrmions in a compensated ferrimagnet. *Nat. Nanotechnol.* **13**, 1154–1160 (2018).

61. Mushnikov, N. V., Goto, T., Gaviko, V. S. & Zajkov, N. K. Magnetic properties of crystalline and amorphous gdco2hx hydrides. *J. Alloys Compd.* **292**, 51–56 (1999).

62. Hansen, P. & Heitmann, H. Media for erasable magnetooptic recording. *IEEE Trans. Magn.* **25**, 4390–4404 (1989).

63. Kim, K. J. *et al.* Fast domain wall motion in the vicinity of the angular momentum

compensation temperature of ferrimagnets. *Nat. Mater.* **16**, 1187–1192 (2017).

64. Sigmund, P. Theory of sputtering. i. sputtering yield of amorphous and polycrystalline targets. *Phys. Rev.* **184**, 383–416 (1969).

65. Price, E. P. Characterization of transport processes in magnetic tunnel junctions. (2001). doi:10.16953/deusbed.74839

66. Thornton, J. A. Structure-zone models of thin films. *Model. Opt. Thin Film.* **0821**, 95 (1988).

67. Qiu, Z. Q. & Bader, S. D. Surface magneto-optic kerr effect. *Rev. Sci. Instrum.* **71**, 1243–1255 (2000).

68. Hamrle, J. Magneto-optical kerr effect (moke) photon-photon spectroscopies (absorption). (2014).

69. Magneto-optical, L. *et al.* Related content measurement of magneto-optical kerr effect using piezo-birefringent modulator. (1981).

70. Emori, S. Magnetic domain walls driven by interfacial phenomena. *PhD Thesis* (2013).

71. Nagaosa, N., Sinova, J., Onoda, S., MacDonald, A. H. & Ong, N. P. Anomalous hall effect. *Rev. Mod. Phys.* **82**, 1539–1592 (2010).

72. Groot, F. De & Kotani, A. *Core Level Spectroscopy of Solids*. (Taylor & Francis Group, 2008).

73. Funk, T., Deb, A., George, S. J., Wang, H. & Cramer, S. P. X-ray magnetic circular dichroism - a high energy probe of magnetic properties. *Coord. Chem. Rev.* **249**, 3–30 (2005).

74. van der Laan, G. & Figueroa, A. I. X-ray magnetic circular dichroism - a versatile tool to study magnetism. *Coord. Chem. Rev.* **277**, 95–129 (2014).

75. X-ray absorption spectroscopy of semiconductors. in *Springer Series in Optical Sciences Volume 190* (eds. Schnohr, C. S. & Ridgway, M. C.) (Springer-Verlag Berlin Heidelberg, 2015).

76. Abbate, M. *et al.* Probing depth of soft x-ray absorption spectroscopy measured in total-electron-yield mode. *Surf. Interface Anal.* **18**, 65–69 (1992).

77. Richardson, T. J. *et al.* X-ray absorption spectroscopy of transition metal-magnesium hydride thin films. *J. Alloys Compd.* **356–357**, 204–207 (2003).

78. O'Brien, W. L. & Tonner, B. P. Orbital and spin sum rules in x-ray magnetic circular dichroism. *Phys. Rev. B* **50**, 12672–12681 (1994).

79. Jo, S. H. *et al.* Nanoscale memristor device as synapse in neuromorphic systems. *Nano Lett.* **10**, 1297–1301 (2010).

80. Lai, Q. *et al.* Ionic/electronic hybrid materials integrated in a synaptic transistor with signal processing and learning functions. *Adv. Mater.* **22**, 2448–2453 (2010).

81. Nishitani, Y., Kaneko, Y., Ueda, M., Morie, T. & Fujii, E. Three-terminal ferroelectric synapse device with concurrent learning function for artificial neural networks. *J. Appl. Phys.* **111**, (2012).

82. Song, S., Miller, K. D. & Abbott, L. F. Competitive hebbian learning through spike-timing-dependent synaptic plasticity. *Nat. Neurosci.* **3**, 919–926 (2000).

83. Kuzum, D., Jeyasingh, R. G. D., Lee, B. & Wong, H.-S. P. Nanoelectronic programmable

synapses based on phase change materials for brain-inspired computing. *Nano Lett.* **12**, 2179–2186 (2012).

84. Prezioso, M. *et al.* Training and operation of an integrated neuromorphic network based on metal-oxide memristors. *Nature* **521**, 61–64 (2015).

85. Serrano-Gotarredona, T., Masquelier, T., Prodromakis, T., Indiveri, G. & Linares-Barranco, B. STDP and stdp variations with memristors for spiking neuromorphic learning systems. *Front. Neurosci.* **7**, 1–15 (2013).

86. Dan, Y. & Poo, M. M. Spike timing-dependent plasticity of neural circuits. *Neuron* **44**, 23–30 (2004).

87. Shi, J., Ha, S. D., Zhou, Y., Schoofs, F. & Ramanathan, S. A correlated nickelate synaptic transistor. *Nat. Commun.* **4**, 2676 (2013).

88. Kim, H. K. H., Sah, M. P., Yang, C. Y. C. & Chua, L. O. Memristor-based multilevel memory. *Cell. Nanoscale Networks Their Appl. (CNNA), 2010 12th Int. Work.* **1**, 1–6 (2010).

89. Widrow, B. An adaptive 'Adaline' neuron using chemical 'memistors'. *Stanford Electronics Laboratories Technical Report* 1553–2 (1960).

90. Thakoor, S., Moopenn, A., Daud, T. & Thakoor, a. P. Solid-state thin-film memistor for electronic neural networks. *J. Appl. Phys.* **67**, 3132–3135 (1990).

91. Yang, R. *et al.* On-demand nanodevice with electrical and neuromorphic multifunction realized by local ion migration. *ACS Nano* **6**, 9515–9521 (2012).

92. Ma, T. P. & Han, J. P. Why is nonvolatile ferroelectric memory field-effect transistor still

elusive? *IEEE Electron Device Lett.* **23**, 386–388 (2002).

93. Bi, C., Xu, M., Almasi, H., Rosales, M. & Wang, W. Metal based nonvolatile field-effect transistors. *Adv. Funct. Mater.* **26**, 3490–3495 (2016).

94. Chattopadhyay, B. Thin film oxidation and the logarithmic rate law. *Thin Solid Films* **16**, 117–124 (1973).

95. Chattopadhyay, B. & Measor, J. C. Initial oxidation of cobalt. *J. Mater. Sci.* **4**, 457–460 (1969).

96. Fehlner, F. P. & Mott, N. F. Low-temperature oxidation. *Oxid. Met.* **2**, 59–99 (1970).

97. Kubicek, M., Schmitt, R., Messerschmitt, F. & Rupp, J. L. M. Uncovering two competing switching mechanisms for epitaxial and ultrathin strontium titanate-based resistive switching bits. *ACS Nano* **9**, 10737–10748 (2015).

98. Muenstermann, R., Menke, T., Dittmann, R. & Waser, R. Coexistence of filamentary and homogeneous resistive switching in fe-doped srtio3 thin-film memristive devices. *Adv. Mater.* **22**, 4819–4822 (2010).

99. Isidorsson, J., Giebels, M. E., Griessen, R. & Arwin, H. Optical properties of mgh2 measured in situ by ellipsometry and spectrophotometry. *Phys. Rev. B - Condens. Matter Mater. Phys.* **68**, 1–15 (2003).

100. Zhao, Q. *et al.* Fast hydrogen-induced optical and electrical transitions of mg and mg-ni films with amorphous structure. *Appl. Phys. Lett.* **102**, (2013).

101. Yoon, H. *et al.* Reversible phase modulation and hydrogen storage in multivalent vo2 epitaxial thin films. *Nat. Mater.* **15**, 1113–1119 (2016).

102. Waser, R. & Aono, M. Nanoionics-based resistive switching memories. *Nat. Mater.* **6**, 833–40 (2007).

103. Armitage, R., Rubin, M., Richardson, T., O'Brien, N. & Chen, Y. Solid-state gadolinium-magnesium hydride optical switch. *Appl. Phys. Lett.* **75**, 1863–1865 (1999).

104. Niklasson, G. A. & Granqvist, C. G. Electrochromics for smart windows: thin films of tungsten oxide and nickel oxide, and devices based on these. *J. Mater. Chem.* **17**, 127–156 (2007).

105. van Gogh, A. T. M. *et al.* Structural, electrical, and optical properties of la1-zyzhx switchable mirrors. *Phys. Rev. B* **63**, 195105 (2001).

106. Von Rottkay, K., Rubin, M. & Duine, P. A. Refractive index changes of pd-coated magnesium lanthanide switchable mirrors upon hydrogen insertion. *J. Appl. Phys.* **85**, 408–413 (1999).

107. Dakhel, A. A. Optical constants of evaporated gadolinium oxide. *J. Opt. A Pure Appl. Opt.* **3**, 452–454 (2001).

108. Isidorsson, J., Giebels, I. A. M. E., Arwin, H. & Griessen, R. Optical properties of mgh2 measured in situ by ellipsometry and spectrophotometry. *Phys. Rev. B* **68**, 115112 (2003).

109. Manivasagam, T., Kiraz, K. & Notten, P. Electrochemical and optical properties of magnesium-alloy hydrides reviewed. *Crystals* **2**, 1410–1433 (2012).

110. Baldi, A., Gonzalez-Silveira, M., Palmisano, V., Dam, B. & Griessen, R. Destabilization of the mg-h system through elastic constraints. *Phys. Rev. Lett.* **102**, 1–4 (2009).

111. Franklin, D. *et al.* Polarization-independent actively tunable colour generation on imprinted

plasmonic surfaces. *Nat. Commun.* **6**, 1–8 (2015).

112. Kreuer, K. D. Aspects of the formation and mobility of protonic charge carriers and the stability of perovskite-type oxides. *Solid State Ionics* **125**, 285–302 (1999).

113. Norby, T. Solid-state protonic conductors: principles, properties, progress and prospects. *Solid State Ionics* **125**, 1–11 (1999).

114. Fert, A., Cros, V. & Sampaio, J. Skyrmions on the track. *Nat. Nanotechnol.* **8**, 152–156 (2013).

115. Parkin, S. S. P., Hayashi, M. & Thomas, L. Magnetic domain-wall racetrack memory. *Science* **320**, 190–194 (2008).

116. Tsymbal, E. Y. Electric toggling of magnets. *Nat. Mater.* **11**, 12–13 (2011).

117. Liu, L. *et al.* Spin-torque switching with the giant spin hall effect of tantalum. *Science* **336**, 555–558 (2012).

118. Heron, J. T. *et al.* Deterministic switching of ferromagnetism at room temperature using an electric field. *Nature* **516**, 370–373 (2014).

119. Matsukura, F., Tokura, Y. & Ohno, H. Control of magnetism by electric fields. *Nat. Nanotechnol.* **10**, 209–220 (2015).

120. Valencia, S. *et al.* Interface-induced room-temperature multiferroicity in batio3. *Nat. Mater.* **10**, 753–758 (2011).

121. Spaldin, N. A. & Ramesh, R. Advances in magnetoelectric multiferroics. *Nat. Mater.* **18**, 203–212 (2019).

122. Baek, S. H. *et al.* Ferroelastic switching for nanoscale non-volatile magnetoelectric devices. *Nat. Mater.* **9**, 309–314 (2010).

123. Fiebig, M., Lottermoser, T., Meier, D. & Trassin, M. The evolution of multiferroics. *Nat. Rev. Mater.* **1**, (2016).

124. Cherifi, R. O. *et al.* Electric-field control of magnetic order above room temperature. *Nat. Mater.* **13**, 345–351 (2014).

125. Cai, K. *et al.* Ultrafast and energy-efficient spin–orbit torque switching in compensated ferrimagnets. *Nat. Electron.* **3**, 37–42 (2020).

126. Ueda, K., Mann, M., De Brouwer, P. W. P., Bono, D. & Beach, G. S. D. Temperature dependence of spin-orbit torques across the magnetic compensation point in a ferrimagnetic tbco alloy film. *Phys. Rev. B* **96**, 1–6 (2017).

127. Chaudhari, P., Cuomo, J. J. & Gambino, R. J. Amorphous metallic films for magneto-optic applications. *Appl. Phys. Lett.* **22**, 337–339 (1973).

128. Katayama, T., Hasegawa, K., Kawanishi, K. & Tsushima, T. Annealing effects on magnetic properties of amorphous gdco, gdfe, and gdcomo films. *J. Appl. Phys.* **49**, 1759–1761 (1978).

129. Ueda, K., Tan, A. J. & Beach, G. S. D. Effect of annealing on magnetic properties in ferrimagnetic gdco alloy films with bulk perpendicular magnetic anisotropy. *AIP Adv.* **8**, 125204 (2018).

130. Schelleng, J. H., Forester, D. W., Lubitz, P. & Vittoria, C. Hydrogenation and magnetic properties of amorphous rare-earth-iron (r-fe) alloys. *J. Appl. Phys.* **55**, 1805–1807 (1984).

131. Pourarian, F. Review on the influence of hydrogen on the magnetism of alloys based on rare earth-transition metal systems. *Phys. B Condens. Matter* **321**, 18–28 (2002).

132. Cho, J. *et al.* Design, fabrication, switching, and optical characteristics of new magneto-optic spatial light modulator. *J. Appl. Phys.* **76**, 1910–1919 (1994).

133. Gilbert, D. A. *et al.* Controllable positive exchange bias via redox-driven oxygen migration. *Nat. Commun.* **7**, 1–8 (2016).

134. Kresse, G. & Furthmüller, J. Efficient iterative schemes for ab initio total-energy calculations using a plane-wave basis set. *Phys. Rev. B - Condens. Matter Mater. Phys.* **54**, 11169–11186 (1996).

135. Perdew, J. P. *et al.* Restoring the density-gradient expansion for exchange in solids and surfaces. *Phys. Rev. Lett.* **100**, 1–4 (2008).

136. Dudarev, S. & Botton, G. Electron-energy-loss spectra and the structural stability of nickel oxide: an lsda+u study. *Phys. Rev. B - Condens. Matter Mater. Phys.* **57**, 1505–1509 (1998).

137. Evans, R. F. L. *et al.* Atomistic spin model simulations of magnetic nanomaterials. *J. Phys. Condens. Matter* **26**, (2014).

138. Knapton, A. G. Palladium alloys for hydrogen diffusion membranes. *Platin. Met. Rev.* **21**, 44–50 (1977).

139. Huang, M. *et al.* Voltage-gated optics and plasmonics enabled by solid-state proton pumping. *Nat. Commun.* **10**, 5030 (2019).

140. Tsuchida, T., Sugaki, S. & Nakamura, Y. Magnetic properties of gdco 2 and gd 1- x y x co 2. *J. Phys. Soc. Japan* **39**, 340–343 (1975).

141. Lemaire, R. & Schweizer, J. Variation du moment magnetique du cobalt dans les composes gduy1−uco2. *Phys. Lett.* **21**, 366–368 (1966).

142. McGuire, T. R. & Gambino, R. J. Hall effect in amorphous gd alloy films. *J. Magn. Magn. Mater.* **15–18**, 1401–1403 (1980).

143. Han, G. *et al.* Control of offset field and pinning stability in perpendicular magnetic tunnelling junctions with synthetic antiferromagnetic coupling multilayer. *J. Appl. Phys.* **117**, 0–4 (2015).

144. Streubel, R. *et al.* Experimental evidence of chiral ferrimagnetism in amorphous gdco films. *Adv. Mater.* **30**, 1–8 (2018).

145. Emori, S., Bauer, U., Ahn, S.-M., Martinez, E. & Beach, G. S. D. Current-driven dynamics of chiral ferromagnetic domain walls. *Nat. Mater.* **12**, 611–616 (2013).

146. Serra, E., Bini, A. C., Cosoli, G. & Pilloni, L. Hydrogen permeation measurements on alumina. *J. Am. Ceram. Soc.* **88**, 15–18 (2005).

147. Fukami, S. & Ohno, H. Perspective: spintronic synapse for artificial neural network. *J. Appl. Phys.* **124**, (2018).